Epitaxial Thin Films of Lanthanum Nickel Oxides:

Deposition by PI-MOCVD, Structural Characterization and High Temperature Transport Properties.

Thesis submitted by MÓNICA BURRIEL LÓPEZ
to apply for the Degree of Doctor at the
Universitat Autònoma de Barcelona
in the Materials Science Program.

March 2007

Supervisors: Dr. José Santiso López
Dra. Gemma Garcia Alonso

ICMAB CSIC

Universitat Autònoma de Barcelona

Institut de Ciència de Materials de Barcelona
Consejo Superior de Investigaciones Científicas
Campus de la UAB
08193 Bellaterra, Barcelona

Universitat Autònoma de Barcelona
Departament de Química
08193, Bellaterra, Barcelona

Dr. JOSÉ SANTISO LÓPEZ, Científico Titular del Institut de Ciència de Materials de Barcelona (ICMAB-CSIC) y Dra. GEMMA GARCIA ALONSO, contratada Ramón y Cajal de La Universitat Autònoma de Barcelona (UAB)

CERTIFICAN:

Que Mónica Burriel López, Ingeniera Química por la Universidad de Zaragoza, ha realizado bajo su dirección el trabajo que lleva por título "Epitaxial Thin Films of Lanthanum Nickel Oxides: Deposition by PI-MOCVD, Structural Characterization and High Temperature Transport Properties.", el cual se recoge en esta memoria para optar al grado de Doctor por la Universitat Autònoma de Barcelona.

Y para que conste, firman el presente certificado.

Bellaterra, marzo de 2007

Dr. José Santiso López

Dra. Gemma Garcia Alonso

A mis padres

"If we knew what it was we were doing,
it would not be called research, would it?"
– Albert Einstein

Acknowledgements

Sin vuestra ayuda, sin vuestra amistad, sin vuestro apoyo, sin vuestro conocimiento... sin todos vosotros esta tesis no habría sido posible. Gracias a todos los que me habeis ayudado directa o indirectamente a conseguirlo.

En primer lugar me gustaría agradecer a mis directores de tesis, al Dr. José Santiso y a la Dra. Gemma Garcia, por todo su tiempo, esfuerzo y dedicación. Por toda la ayuda en el laboratorio, las discusiones científicas, las correcciones... Gracias a ellos he podido desarrollar este trabajo de investigación y he aprendido, y sigo aprendiendo, cada día. Gracias además, por su amistad.

Y ahora que este despacho está vaciándose de la gente del nuestro grupo, que se están mudando al nuevo edificio, es el momento de recordar a todos con los que aquí he compartido sonrisas, palabras, llantos, risas, música... mil y una historias y algún que otro cabreo, y que han conseguido que este rinconcito del mundo se haya convertido en mi segunda (o tercera) casa durante los cuatro últimos años. Gracias a todos: a los que estabais aquí durante los primeros años: José Ángel, Isaac, Silvia Molas, Eva, Judit..., a los que llegasteis más tarde: Pepe, Silvia Chellini, Neil, Ernest... y, muy especialmente, al grupito que hemos compartido despacho durante el último año: Carmen, ¡Carmensita!; Guillaume, que tiene la niña más mona del mundo; Cecilia, mi gemelita y Juanjo, el rey de los pajaritos. ¡Esos becarios de la semana de moda! La verdad es que con este buen ambiente da gusto venir a trabajar. ¡Mucha suerte y muchos ánimos con vuestras tesis! Gracias especialmente a Cecilia, con quien he compartido mucho más que despacho: ilusiones, sueños, viajes, decepciones, comidas, muchas risas y muchas horas de gimnasio. En resumen, hemos compartido una gran amistad y, gracias a ella, esta tesis y estos años han sido más felices.

También me gustaría agradecer a todo el resto de compañeros y amigos del ICMAB, por todos los buenos ratos de trabajo y cafetería, de tren (a los que nos ha tocado sufrir la RENFE juntos), de SAF, de club de los viernes, cenas, fiestas... ¡incluso viajes por el mundo! A Gerard, por su humor, es genial; a Belén, por su sonrisa; a Montse, ¡eeh!; a Jordi, que fue mi compañero de baile; a Gemma Gabriel, ¡que se nos casa dentro de ná!; a Neus, con quien surgió una bonita amistad gracias a un congreso en Toledo; a Andrea, pecattore!; a Emi, reina, ¿o loca de la colina? ¡me estás llevando por la mala vida!; a Roberto, a quien cada día le voy entendiendo un poco más el argentino; a Natalia y Carolina, las nuevas compañeras de despacho; a Jesús, muchas gracias por el informe y las sugerencias de la tesis... a Corina, a Jose Manuel, a Anna Llordés, a Manuel, a Sandra, a Adrián, a Eli, a Liber, a Aitor, a Karina, a Oscar Castaño, a Mariona, a Joffre... a los compañeros de volley: Félix, Carmelo, Anna, Ariadna, Albert, Vicente... ¡Y a todos los que me estoy olvidando!

Muchas gracias a toda la gente de Administración, cuyo trabajo suele ser poco reconocido pero imprescindible para que todo funcione adecuadamente; a Montse Salas, con quien me he reído mucho; a nuestra super-bibliotecaria Tonia, a los informáticos: al hombre de la bata blanca (Javier); a Marc, a Nacho... ¡¿qué haríamos sin vosotros?!, y a toda la gente de mantenimiento: Toni Pons, Josep y a Jose, por esos bailoteos en las fiestas del instituto. Al resto del grupo de Crecimiento Cristalino: Albert, Eniko... Y a mi tu tutor, el Dr. Ramón Yáñez, que ha estado siempre dispuesto a echar una firmita donde hiciera falta.

I would like to thank Marta Rosell and Gustav van Tendeloo for their collaboration, for the very nice high resolution images and electron diffraction patterns of the films. A Francesc del Servei de Microscòpia de la Universitat Autònoma de Barcelona y a Pep Bassas, Xavier Alcobé y Xavier Llovet de los Serveis Cientificotècnics de la Universitat de Barcelona; por su gran ayuda e interés en los distintos tipos de caracterización y medida de las muestras.

During my PhD I have had the opportunity of spending some time in other laboratories abroad, collaborations which resulted very fruitfull and from which many results are shown in this thesis.

I would like to thank all the research team of the Fuel Cell Department of Risoe, everybody was very helpful and nice during my stay there. Very special thanks to

Dr. Nikolaos Bonanos, for all the time he dedicated to my work, to the conductivity measurements of the $La_2NiO_{4+\delta}$ films. I learnt a lot about science and enjoyed very much my time there, it has been a pleasure to work with him. And thanks to Martin as well for the help during my stay at Risoe and for the discussions then and after about the electrical conductivity relaxation measurements.

I would also like to thank all the people from the Materials Department of the Imperial College. Thanks to Professor John Kilner and Dr. Stephen Skinner for giving me the opportunity of working with them, learning a new technique, using the IEDP equipment and for all the scientific discussions. And very special thanks to Mr. Richard Chater, who tought me how to use the SIMS and isotope exchange equipment and spent many hours (long days!) in the lab helping me. We solved together many problems which we found in the way, we discussed many aspects about the measurements and he also encouraged me when I felt despair and thought it was impossible to get any results. Thank you Richard for your friendship too. I also would like to thank Sarah and Jeremy for their help with the SIMS measurements. Y a Alberto, con quien coincidí de estancia en Londres... ¿qué habría sido de Londres sin esas pintas y esos nachos, y sin esas locuras transitorias...?

También a todos mis amigos de Zaragoza, con quienes he podido disfrutar desde hace muchos años, unas veces de la naturaleza, montaña o bicis y otras veces de la ciudad, tomando una cañita y convensando. Gracias por vuestra amistad, vuestros sueños y vuestra alegría, gracias a Oscar, a Tere, a Víctor, a Gabi, a Andrea, a Diego, a Laura, a Luismi, a Maite, a Guille... Gracias a Mariví y Ángela, con quienes, aunque nos veamos de ciento a viento, hemos conseguido mantener la amistad desde el cole.

Y por supuesto a las personas más importantes, gracias a quien soy como soy: a mis padres. Gracias, mamá. Gracias papá. Gracias por vuestro apoyo y por vuestro amor. Y al resto de mi familia: a mis hermanas Marta e Isabel, a mi tío Pepe, a mi yayo Félix..., que siempre dice que se considera el más tonto, pero en realidad es una de las personas más sabias del mundo, porque sabe que lo más importante en la vida es intentar ser feliz. A David.

Abstract

In the last years there has been a great interest in the study of the $La_2NiO_{4+\delta}$ compound due to its mixed ionic-electronic properties, which make it suitable in electrochemical devices, such as cathode in Intermediate Temperature Solid Oxide Fuel Cells (IT-SOFC), permeation membranes or gas sensors. The $La_2NiO_{4+\delta}$ phase structure is formed by perovskite-type $LaNiO_3$ layers alternated with rocksalt-type LaO layers, in which hyperstoichiometric oxygen can be incorporated. This layered structure is responsible for the anisotropy in the $La_2NiO_{4+\delta}$ properties, leading to electronic and ionic conductivity three orders of magnitude higher along the *ab* plane, in comparison with the *c*-axis direction.

This work is focused on the study, from a fundamental point of view, of epitaxial *c*-axis oriented $La_2NiO_{4+\delta}$ thin films deposited by PI-MOCVD technique on different substrates, in order to achieve a better comprehension of the microstructural characteristics, their variation with strain and their influence in its high temperature transport properties. Moreover, the epitaxial growth of the films permits the measurement of the properties of the $La_2NiO_{4+\delta}$ in two perpendicular directions, to have a diret inset of the anisotropy.

The $La_2NiO_{4+\delta}$ phase is the $n = 1$ member of the $La_{n+1}Ni_nO_{3n+1}$ Ruddlesden-Popper family, in which the structure of each member is formed by a n number of perovskite layers alternated between rock-salt layers. We have also attempted to deposit *c*-axis oriented films of the $n = 2$, $n = 3$ and $n = \infty$ members and studied the variation of the transport properties through the different members of the family.

First, Chapter 1 consists of an introduction to the mixed ionic-electronic conductors (MIEC) and to the solid oxide fuel cell (SOFC) cathodes, as a possible application of the $La_2NiO_{4+\delta}$ material. The most remarkable properties of the $La_2NiO_{4+\delta}$

phase, and of the $n = 2$, 3 and ∞ members of the $La_{n+1}Ni_nO_{3n+1}$ family are analyzed, as well as the state of the art in the preparation of thin films of these materials.

In Chapter 2, the Metalorganic Chemical Vapor Deposition (MOCVD) technique is described, accompanied by a detailed description of the selected experimental deposition parameters and of the Pulsed Injection MOCVD equipment used. Chapter 3 summarizes all the techniques used for the $La_{n+1}Ni_nO_{3n+1}$ thin film characterization.

In Chapter 4, the optimized experimental parameters for the deposition of epitaxial $La_2NiO_{4+\delta}$ thin films are described. Structural, morphological and microstructural characterization is performed as a funciton of film thickness, substrate used and temperature. Total conductivity of epitaxial layers is also described and discussed.

In Chapter 5 we have studied the oxygen exchange and transport of the $La_2NiO_{4+\delta}$ thin films by two different techniques: the oxygen isotope exchange and the electrical conductivity relaxation. Results are discussed as a function of microstructure.

Finally, in Chapter 6, the study is completed describing the first results of the deposition of the other members of the Ruddlesden-Popper family. Evolution of the total conductivity properties of the $La_{n+1}Ni_nO_{3n+1}$ films has been related to the n number of perovskite layers.

List of Acronyms and Symbols

A considerable amount of acronyms and symbols have been used throughout this manuscript. Although most of them have already been described in their context, they are listed below in alphabetical order.

acac 2,4-pentanedionate (acetoacetonate)
AC Alternating Current
AES Auger Electron Spectroscopy
AFC Alkaline Fuel Cells
AFM Atomic Force Microscopy
ALE Atomic Layer Epitaxy
APCVD Atmospheric Pressure Chemical Vapor Deposition
c Oxygen concentration
c^* Isotopic concentration
c^*_{bg} Background isotopic concentration
c^*_g Isotopic concentration in the gas phase
CL Cathodoluminescence
CVD Chemical Vapor Deposition
D^*_i Tracer experiment oxygen diffusion coefficient in the direction i
D_{Chem} Chemical diffusion coefficient
D_Q Electrical experiment diffusion coefficient
δ Oxygen hyperstoichiometric content
DC Direct Current
DMFC Direct Methanol Fuel Cells
E Strain

E_a Activation energy

ECR Electrical Conductivity Relaxation

ED Electron Diffraction

EDS Energy Dispersive Spectrometry

EELS Electron Energy Loss Spectroscopy

EMAT Electron Microscopy for Materials Science

EVD Electrochemical Vapor Deposition

F Faraday constant

FIB Focused Ion Beam

FTIR Fourier Transform Infrared

FWHM Full Width at Half Maximum

$g(t)$ Normalized conductivity

h Holes

HREM or HRTEM High Resolution Transmission Electron Microscopy

HTT High Temperature Tetragonal

IC Internal Combustion

IEDP Isotope Exchange Depth Profile Method

IR Infrared Radiation

ICMAB-CSIC Materials Science Institute of Barcelona

IT-SOFC Intermediate Temperature Solid Oxide Fuel Cell

k_o Kinetic rate constant

k_i^* Tracer experiment surface exchange coefficient in the direction i

k_{Ex} Chemical surface exchange coefficient

k_Q Conductivity experiment surface exchange coefficient

λ Cu wavelength (1.5406 nm)

l Film thickness

l_d Characteristic length of a material (D_{Chem}/k_{Ex})

LAO $LaAlO_3$

LPG Liquified Petroleum Gas

LPCVD Low Pressure Chemical Vapor Deposition

LTO Low Temperature Orthorhombic

LTT Low Temperature Tetragonal

LTLO Low Temperature Less Orthorhombic

μ Hole mobility

MCFC Molten Carbonates Fuel Cells

MIEC Mixed Ionic Electronic Conductors

MOCVD Metalorganic Chemical Vapor Deposition

NGO $NdGaO_3$

OMVPE Organometallic Vapor Phase Epitaxy

p Pressure

PAFC Phosphoric Acid Fuel Cells

PECVD Plasma Enhanced Chemical Vapor Deposition

PACVD Photo-Assisted Chemical Vapor Deposition

PEFC Polymer Electrolyte Fuel Cells

PI-MOCVD Pulsed Injection Chemical Vapor Deposition

Q_x, Q_y Coordinates from a reciprocal space map

r Film growth rate

R Universal gas constant

ρ Resistivity

RMS Root Mean Square

σ Conductivity

σ_e Electronic conductivity

SCT-UB University of Barcelona Technical Services

SEM Scanning Electron Microscopy

SIMS Secondary Ion Mass Spectrometry

SOFC Solid Oxide Fuel Cell

STEM Scanning-Transmission Electron Microscopy

STM Scanning Tunnelling Microscope

STO $SrTiO_3$

t Time

T Temperature

T_c Critical temperature

τ_f Finite flush time

τ_n Time constant

TACVD Thermal Activated Chemical Vapor Deposition

TEC Thermal Expansion Coefficient

TEM Transmission Electron Microscopy

TGA Thermogravimetric analysis

thd 2,2,6,6-tetramethyl-3,5-heptanedionate

TPB Three Phase Boundary

V_m Molar volume

w_o Thermodynamic factor

WDS Wavelength Dispersive Spectrometry

XRD X-Ray Diffraction

XRR X-ray reflectometry

YSZ Yttria Stabilized Zirconia

Contents

List of Figures

List of Tables

Chapter 1

Introduction

The current power generation economy based mainly on fossil fuels is not sustainable. The demand for energy is growing and the raw materials are diminishing, as oil, coal, and natural gas supplies are not replenished as they are consumed. If present usage levels are sustained, fossil energy resources created over several hundred millions of years will be used up within just some generations. In addition, there are environmental costs associated to massive combustion of fossil fuels which must be taken into account. Emissions from fossil fuel usage significantly degrade air quality all over the world. Moreover, the resulting carbon byproducts are substantially changing the world's climate. These resulting health and climate impacts are unacceptable. Furthermore, most of the people who consume fossil fuels do not live where fuels are extracted. This situation creates enormous economic motivation for the consuming nations to try to exert control over the regions that supply the fuels, thus generating international conflicts with the intrinsic negative social consequences.

Therefore, managing global energy supplies is increasingly becoming a key issue for the future of mankind. The substitution of the "black gold" by renewable energy sources and the development of new technologies, such as the fuel cell, are crucial. Fuel cells are now on the verge of being introduced commercially, revolutionizing the way we presently produce power. They can use hydrogen as fuel, offering the prospect of supplying the world with clean sustainable electrical power with many diverse applications. These include applications in the transportation, stationary

power and portable power sectors. Notwithstanding all these advantages it should be noted that hydrogen is not found naturally on earth as a free element, but forming compounds, and thus is not an energy source but an energy vector, a way to store energy. As such, the environmental friendliness of hydrogen will be determined by that of the primary energy source used to generate it [1].

1.1 Solid Oxide Fuel Cells

Fuel cells are electrochemical devices that are able to directly convert chemical energy to electrical energy, without any Carnot limitation. Hence, as the intermediate physical conversion is absent, their energy efficiencies are relatively high.

A fuel cell is mainly composed by an electrolyte, a cathode and an anode. Gaseous fuels are fed continuously to the anode while an oxidant is fed continuously to the cathode. The electrochemical reactions take place at the electrodes/electrolyte/gas interface to produce an electrical current [2]. Practical fuel cells are not operated as single units; rather, they are connected in electrical series to build up voltage. A series of cells is referred to as a stack.

There are several types of fuel cells under development, which are characterized by the electrolyte used and their operating temperature (see Table 1.1 [2]).

Table 1.1: Summary of the different fuel cell types

Fuel Cell type	**Abbreviation**	**Working Temperature**	**Fuel**	**Electrolyte**	**Charge Carrier**
Alkaline	AFC	100 °C	H_2	KOH aqueous	OH^-
Polymer Electrolyte	PEFC	80-110 °C	H_2	Nafion	H^+
Phosphoric Acid	PAFC	150-210 °C	H_2	H_3PO_4	H^+
Molten Carbonate	MCFC	550-650 °C	H_2, CO	$KLiCO_3$	CO_3^{2-}
Solid Oxide	SOFC	600-1000 °C	hydrocarbons	e.g. YSZ	O^{2-}

Among them, Solid Oxide Fuel Cells (SOFC) are operated at high temperatures (600 - 1000 °C) and, unlike low temperature fuel cells, can run without previous reforming on various fuels, such as natural gas (primarily CH_4), bio-gas, methanol and ethanol, liquified petroleum gas (LPG), naphtha, gasified coal and hydrogen [3] . The oxygen is reduced on the cathode side and the electrolyte transports the

required O^{2-} to the anode, where the fuel is then oxidized (see figure 1.1).

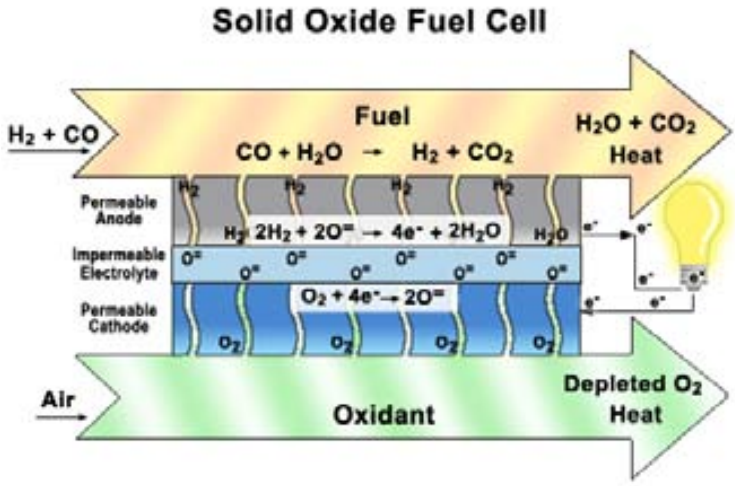

Figure 1.1: Schematic representation of a solid oxide fuel cell [4].

This anion diffusion generates an external electron flow to conserve electron neutrality. SOFCs are able to generate both electricity and high quality heat, by an exotermic reaction, which may be used for space heating, steam generation or combined power cycle applications. Due to the high temperatures required for the operation of a SOFC, major parts of its building units (cathode, electrolyte, anode and, particularly, interconnects) are made of expensive ceramic materials [5, 6]. SOFCs use a solid oxygen ion conducting electrolyte, typically yttria stabilized zirconia (YSZ), although new materials are under investigation, such as rare-earth doped ceria, Sr and Mg doped lanthanum gallate (LSGM), bismuth oxides, etc. The reactions occur at the three phase boundary (TPB) where the gas meets electrode and electrolyte material. The reaction occurring at the cathode TPB is:

$$1/2\ O_2 + 2e^- \rightleftharpoons O^{2-} \tag{1.1}$$

while the following reactions may occur at the anode TPB:

$$H_2 + O^{2-} \rightleftharpoons H_2O + 2e^- \tag{1.2}$$

$$CO + O^{2-} \rightleftharpoons CO_2 + 2e^- \tag{1.3}$$

The oxygen ions are conducted through the electrolyte, while the electrons are recovered through an external electric circuit. The overall reactions are:

$$H_2 + 1/2\ O_2 \rightleftharpoons H_2O \tag{1.4}$$

$$CO + 1/2\ O_2 \rightleftharpoons CO_2 \tag{1.5}$$

The efforts over the last decades, however, have shown that, in spite of its conceptual simplicity, SOFC technology is also quite demanding. Major problems on the way to an industrial scale application of solid oxide fuel cells are long-term stability and production costs, both related to the high operation temperatures of SOFC systems. On the one hand, high temperatures limit the choice of materials and complicate the production process. On the other hand degradation phenomena due to interdiffusion and chemical reactions, which restrict the lifetime of a SOFC, are usually more problematic at higher temperatures. Therefore the SOFC technology research effort is directed towards a lowering of the operating temperature of the fuel cell. Currently, to obtain the best performance from the electrolyte, anode and cathode materials operation has to be largely above 800 °C. One important goal in SOFC research is therefore the search for anode and cathode materials which offer a sufficient electrochemical performance already at intermediate temperatures (500-750 °C).

Lowering of the operating temperature would enable, from a materials point of view, increased durability of stack components, as well as affording a greater choice of cost effective materials, especially metallic alloys based interconnects, to build stack components.

1.2 Cathodes for Solid Oxide Fuel Cells

For an application as SOFC cathode, a material has to exhibit several general properties [5, 6]. The basic requirement for any electrode material is a high electronic conductivity. Further, the cathode material must be chemically stable under fuel cell operating conditions, in particular against the electrolyte. Compatibility with respect to the electrolyte refers not only to chemical inertness both during operation and preparation (which usually involves considerably higher temperatures), but also

to the thermo-mechanical compatibility of the two materials in contact, i.e. similar expansion coefficients. The key feature for a cathode material, however, is to have an improved performance, which is achieved by decreasing the corresponding polarization resistance. Two means of optimization can be employed: a) geometrical parmeters (e.g. porosity, particle size) can be varied, and b) materials properties may be improved, e.g., by modifying the dopant ion or dopant concentration, to obtain a high catalytic activity with respect to the oxygen reduction reaction. The ideal electrode must transport gaseous (or liquid) species, ions, and electrons; and, at the points where all three meet, the so-called triplepoint boundaries, the electrocatalysts must rapidly catalyze electro-oxidation (anode) or electroreduction (cathode) reactions. It is generally assumed that the electrodes must be porous, electronically conducting, electrochemically active, and have high active surface areas. Another possibility is to use dense mixed ionic and electronic conductor materials (MIEC), in which the threefold contact cathode/electrolyte/gaseous oxygen which limits the kinetics (due to a poor accessibility) is extended to a double interface gaseous oxygen/mixed conductor/electrolyte in the mixed conductor cathode concept [7].

1.3 Mixed Ionic Electronic Conductors (MIEC)

The aim of using a mixed conductor (MIEC) as a cathode is to combine ionic (O^{2-}) and electronic conductivities. Indeed, two reactions may occur at the cathode, depending on if an interstitial or vacancy ionic conductivity mechanism is involved (Kröger-Vink notations [8]):

$$1/2O_2(g) + 2e^- \rightarrow O_i'' \tag{1.6}$$

or

$$1/2O_2(g) + V_{\ddot{O}} + 2e^- \rightarrow O_O^x \tag{1.7}$$

These reactions express the reduction of ambient oxygen at the cathode/gaseous interface. The mixed conductor brings the electrons for the reduction and, at the same time, ensures the transport of the O^{2-} ions towards the second interface between the cathode and the solid electrolyte itself. The increased kinetics should permit to decrease the SOFC operating temperature. Other applications of such

materials concern membranes used for oxygen purification or for partial oxidation of hydrocarbons [9].

Significant developments have been made in the field of perovskite and perovskite-related mixed ionic-electronic conductors for their use as SOFC cathodes [10]. Most of this early work concerned SOFCs based on YSZ electrolytes working at high temperatures. However more recent work has focused on the use of doped CeO_2 as the electrolyte for applications at temperatures around 650 °C. As cathodes should be compatible with the electrolyte, it is necessary for the perovskite oxides initially identified as candidates for SOFC cathodes to be optimized through doping strategies [11].

As already mentioned, early candidates for cathodic operation included the lanthanum cobaltite, $LaCoO_3$ [5, 12, 13], and lanthanum manganite, $LaMnO_3$ [5, 14–16], based perovskites. These stoichiometric compositions were found unsuitable in terms of electrochemical performance for a cathode but doping of the A-site of the perovskite with an alkaline rare earth such as Sr dramatically improved the conductivity and, hence, high electrochemical performance at the cathode could be achieved. From these investigations, it was found that the ionic conductivity of the $La_{1-x}Sr_xCoO_{3-\delta}$ (LSC) composition was among the highest for oxide ion conductors [17], comparable or superior to that of YSZ, with only δ-Bi_2O_3 having a higher conductivity over a temperature range of 600-1000 °C [18]. In contrast to this ionic conductivity, the electronic conductivity was relatively low, whereas the Mn analog (LSM) was found to have high electronic conductivity of the order of 300 $S{\cdot}cm^{-1}$, but poor oxide ion conductivity [19, 20]. In these perovskite oxides, and also in fluorite-type oxides in which vacancy-based conduction mechanism is present, the dopant-vacancy interactions can limit the conductivity.

From this, it is evident that each material has both advantages and disadvantages when considered as cathode material. However, on further investigation the thermomechanical properties and, in particular, the thermal expansion coefficient of the LSC were found to be very high ($\geq$ 20 x 10^{-6} K^{-1}) and could not be used with the existing conventional electrolytes (YSZ (18% mol Y_2O_3) 10.5-11.0 x 10^{-6} K^{-1}). Therefore, while the level of ionic conductivity was attractive, it was necessary to counter the deficiencies discovered. Co-doping on the B-site with Fe to

form materials of composition $La_{1-x}Sr_xCo_{1-y}Fe_yO_{3-\delta}$ was identified as a promising solution. Fe was found to reduce the thermal expansion coefficient of the cathode material and consequently enable matching with the electrolytes, albeit with some reduction in the level of ionic conductivity particularly at the lower temperatures [21–23]. Among the attractive alternatives to the perovskites already mentioned for application as fuel cell cathodes are the Gd based perovsites (Al- and Sc- doped LSGM) and the compositions $Sm_{1-x}Sr_xCoO_{3-\delta}$ (SSCs), which have demonstrated to operate at temperatures as low as 500 °C [11].

K_2NiF_4 type oxides As the development of the perovskite oxide compositions appears to show intrinsic limitations, there has been increasing interest in alternative types of mixed conductors. Of most interest has been the recent development by a number of groups of the perovskite-related oxides of the K_2NiF_4 ($A_2BO_{4+\delta}$) structure shown in Figure 1.2. The structure is formed by layers of ABO_3 separated by AO layers. The large interest of this layered structures relies on their great flexibility in the oxygen stoichiometry. Indeed, it is possible to incorporate excess oxygen in the unusual form of an *interstitial* species and this provides an attractive alternative to the vacancy-based conduction mechanism, where the dopant-vacancy interactions can limit the observed conductivity. In the stoichiometric oxide ($\delta = 0$) a network of unoccupied interstitial sites appears in the structure. As the material oxidizes, excess oxygen ($\delta > 0$) is accommodated in those interstitial sites and the network becomes partially occupied [11].

In the $La_2NiO_{4+\delta}$ compound, the oxygen excess δ leads to improved capacities toward both oxygen reduction and efficient O^{2-} diffusion at temperatures between 500-800 °C, with better performances than any pure perovskite phase [24–30]. In addition to a relatively high oxygen-ion diffusion, La_2NiO_4-based phases with K_2NiF_4 type stucture present p-type electronic conductivity in the whole $p(O_2)$ range where the K_2NiF_4 phase exists and they are chemically compatible and have similar TEC values to the typical solid electrolytes (YSZ, doped ceria) [25, 27, 31]. Further investigations of electrochemical properties of $Ln_2NiO_{4+\delta}$ (Ln = Nd, Sm, Pr) [32] materials have indicated that by using alternative rare earth elements the oxygen diffusion and cathode performance can be enhanced. Other compositions, $La_2Ni_{1-x}Fe_xO_{4+\delta}$

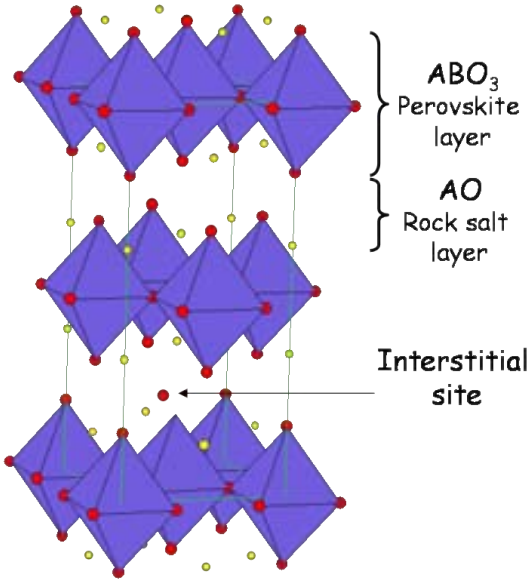

Figure 1.2: Representation of the $A_2BO_{4+\delta}$ structure.

and $La_2Cu_{1-x}Co_xO_{4+\delta}$ have shown attractive oxygen permeation properties with a maximum flow density of 10^{-7} mol·s^{-1}·cm^{-2} at 850 °C [26–28].

Other studies have shown that the $La_{2-x}Sr_xMO_{4+\delta}$ family (M = Ni, Fe, Cu, Co) are also mixed ionic electronic conductors (MIEC) exhibiting satisfactory performances in terms of electronic conductivity (due to the metal mixed valency), of ionic transport properties (due to the oxygen overstoichiometry), of electrocatalysis of the oxygen reduction and of thermal expansion coefficients [25, 28, 29, 31].

In summary, from the current results, it seems that pure $La_2NiO_{4+\delta}$ could be a suitable MIEC material to be used in electrochemical devices.

1.4 $La_2NiO_{4+\delta}$: State of the Art

Originally, $La_2NiO_{4+\delta}$ was investigated because it is isostructural with the superconducting phase $La_2CuO_{4+\delta}$. In $La_2CuO_{4+\delta}$ holes injected into the CuO_2 sheets by the excess oxygen ions make the material superconducting [33, 34]. Similar behavior was hypothesized for $La_2NiO_{4+\delta}$ [35–37], although no high temperature superconducting

properties were found [38].

Structure $La_2NiO_{4+\delta}$ is the $n = 1$ member of the Ruddlesden-Popper (RP) series $La_{n+1}Ni_nO_{3n+1}$, in which each n member's structure consists in the intergrowth of an n number of perovskite layers between each rock salt layer. The $n > 1$ members of the series will be described in detail in Section 1.5. The ideal K_2NiF_4 structure, usually called High Temperature Tetragonal (HTT) in the literature, can be considered as an intergrowth of $LaNiO_3$ perovskite blocks and LaO NaCl-type layers (see Figure 1.3). The structure is stable when a perfect match between the two types of units is achieved. In stoichiometric samples, $La_2NiO_{4.00}$, this happens for $T > T_{c2} \approx 770$ K. Below T_{c2}, a distorted structure is stabilized to relieve the stress (compressive in the NiO_2 sheets and tensile in the rock-salt layers) appearing as a consequence of the different thermal expansion coefficients of the La-O and Ni-O bonds. The symmetry of this new phase is orthorhombic *Bmab* and it is known as Low Temperature Orthorhombic (LTO) phase. By decreasing the temperature, the orthorhombic strain $s = 2(b - a)/(a + b)$ of the LTO phase increases. However, at $T = T_{c1} \approx 80$ K, the strain disappears ($s = 0$), and a new phase appears. Two possible transitions have been identified: from Low Temperature Orthorhombic (LTO) to Low Temperature Tetragonal (LTT) ($P4_2/ncm$ space group) or from Low Temperature Orthorhombic (LTO) to Low Temperature Less Orthorhombic (LTLO) ($Pccn$) [39, 40]. The former structural transitions can be described as the result of cooperative rotations of the NiO_6 octahedra. In the HTT ($F4/mmm$) phase, the octahedra are slightly elongated but not tilted, and turn around the [100] direction when the compound undergoes the HTT $\rightarrow$ LTO phase transition. The orthorhombic distortion and the value of the tilt angle ω increase by decreasing the temperature (from 5.3° at 250 K to 5.8° at 120 K in La_2NiO_4). At $T = T_{c1}$ they reach a limiting value due to the presence of the rare earth ion in the path of the apical oxygens. Then, the tilt axis changes suddenly from [100] to [110] and the LTT ($P4_2/ncm$) phase is stabilized. The displacements of the NiO_6 octahedra as well as the tilt axes, the tilt angles and the labeling of the O sites in the three space groups have been schematically represented in Figure 1.4 [40, 41].

It is quite difficult to obtain stoichiometric and homogeneous $La_2NiO_{4.00}$ ($\delta =$

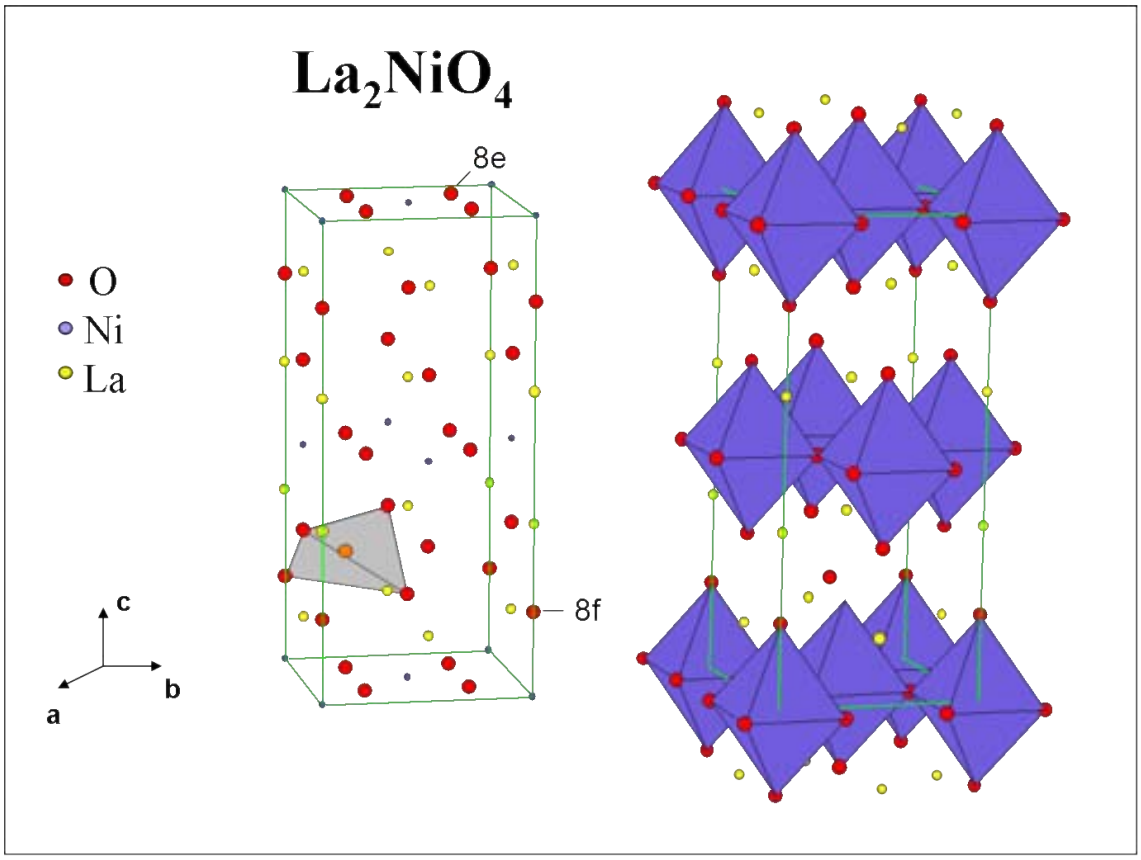

Figure 1.3: Representation of the La_2NiO_4 structure. The interstitial defect site is shown with an outline of the tetrahedral La coordination environment. The interstitial site is also tetrahedrally coordinated by apical oxygen ions.

0) phase. The reason for this is that this compound can very easily uptake oxygen, a reaction which is already observed at ambient temperature, and which proceeds quite rapidly for powder samples. The high reactivity of these undoped phases requires a handling under high quality inert gas atmosphere and may also explain the contradictory results for the physical and structural properties of the stoichiometric compounds found in the literature. Another difficulty to obtain pure phases, especially for the preparation of large single crystals, arises from the fact that all of these compounds may contain Ruddlesden-Popper type intergrowth phases. Actually, La_2MO_4 can also be written as $LaO(LaMO_3)_n$ (n = 1), yielding for n > 1

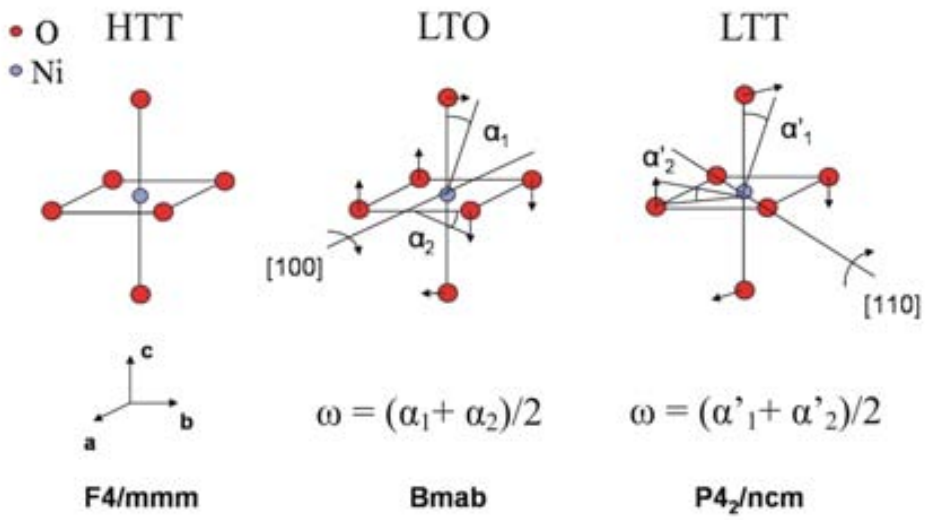

Figure 1.4: Schematic representation of the displacements of the O atoms in the HTT (F4/mmm), LTO (Bmab) and LTT ($P4_2/ncm$) phases.

to the formation of intermixed phases. Even intergrowth texture of NiO has been encountered in La_2NiO_4 [42].

The O-doping phase diagram has been studied by several groups with different techniques [39, 41, 43–47] and maximum δ values ranging from 0.16 to 0.25 have been reported [39, 43, 48].

The oxygen excess is accommodated in the $La_2NiO_{4+\delta}$ structure as interstitial defects placed at (0.25, 0.25, 0.25) (see Figure 1.3) [49, 50]. The defect site is located in the La_2O_2 rocksalt interlayer and is coordinated tetrahedrally by both La^{3+} and apical oxygen sites. The presence of vacant interstitial sites should also favor oxygen vacancies (so-called Frenkel defects) represented by:

$$O_O^x \leftrightarrow V_{\ddot{O}} + O_i'' \tag{1.8}$$

This intrinsic defect involving oxygen vacancies in equatorial sites (8e) is the most favorable one according to atomistic calculations by Minervini et al. [50]. This is another stabilizing factor which decreases the average size of the perovskite type NiO_2 layer; correspondingly, the average size of the rocksalt La_2O_2 layer is increased.

As has previously been mentioned, at ambient temperature the structure of the stoichiometric compounds $La_2NiO_{4.00}$ is orthorhombic (LTO), space group *Bmab* [40, 41, 43, 49], made of a stacking sequence of La_2O_2 bilayers, intrinsic positively charged, and NiO_2 monolayers, intrinsic negatively charged. The strain may be released by either a tilting of the NiO_6 octahedra in the [100] direction by an angle (Figure 1.4) [43, 49], or by an oxygen intercalation in the La_2O_2 double layers, resulting in overstoichiometric phases $La_2NiO_{4+\delta}$. In the latter case, the release of strain in the NiO_2 plane arises both from the partial oxidation of Ni^{2+} into Ni^{3+} and from a tilting of NiO_6 octahedra [51]. Frayret et al. provided very recently the first computational evidence that the intercalation of interstitial oxygen in $La_2NiO_{4+\delta}$ actually causes a tilting of NiO_6 octahedra. As a function of δ, at room temperature the system shows a sequence of pure phases LTO $\rightarrow$ LTT $\rightarrow$ HTT separated by biphasic regions of LTO/LTT and LTT/HTT. These biphasic regions are the result of miscibility gaps which follow from the unmixing of interstitial oxygen defects into oxygen-poor and oxygen-rich domains. Strong interstitial oxygen correlations give rise to these miscibility gaps.

Beyond $\delta = 0.17$, some ordering phenomena were evidenced by Demourgues et al. [48, 52, 53] from neutron diffraction and transmission electron microscopy. In the case of $La_2NiO_{4.25}$, ordering occurs both in the La_2O_2 layer and along the [111] direction of the parent tetragonal structure leading to a 2x2x1 superstructure corresponding to a monoclinic oxygen-ordered phase of space group C_2. In the intermediate range of oxygen incorporation ($0.04 < \delta < 0.18$), considerable debate surrounds the crystal structure adopted both at room and high temperatures. The electron diffraction patterns [54] performed for $0.04 < \delta < 0.20$ samples suggests a three-dimensional ordering of the interstitial oxygen ions, which occurs when δ equals to 1/2n, where n is an integer. The structural determination on single crystals with various oxygen excess ($0.05 \leq \delta \leq 0.11$) by neutron diffraction made at 300 K by Tranquada et al. [44] shows that tilting of the NiO_6 octahedra is always evidenced and that the interstitial oxygens in bulk crystals order one dimensionally in layers ordered periodically along the *c*-axis, similar to the staging of intercalates in graphite. This result is contrary to the conclusions of Hiroi et al. The interstitial oxygen will repel the nearest-neighbour oxygens displacing them away from the

interstitial. The tilts will then propagate within the planes and one would find the *Bmab* tilt pattern above and below the plane of the interstitial. Thus, the accommodation of the interstitial oxygen atoms involves a reversal of the usual *Bmab* tilt pattern on crossing the plane of the interstitials, creating an antiphase domain boundary. The tilt pattern in the intercalated phase creates an entire array of favorable positions, whereas none exist in the normal *Bmab* phase. Hence, it appears that once an interstitial oxygen occupies a (0.25, 0.25, 0.25) position in a particular layer, it will be energetically favorable for other oxygen atoms to occupy the same layer. The Coulomb repulsion between ionic interstitials will limit the density within an interstitial layer, and also the spacing of intercalated layers along the *c*-axis. In the case of alkali metals intercalated in graphite, the long-range repulsive interaction between layers leads to a periodic ordering of the alkali layers. Tranquada et al. [44] show that a similar periodic ordering of intercalated oxygen layers occurs in $La_2NiO_{4+\delta}$ over a significant range of δ. To describe the ordering they have adopted the notion of "staging" developed for intercalated graphite. A stage "s" ordering consists of single interstitial oxygen layers separated by "s" NiO_2 planes.

Although there are some discrepancies between the various proposed phase diagrams, most features are summarized by the schematic diagram in Figure 1.5 reported by Tranquada et al. [44, 55].

Thus $La_2NiO_{4+\delta}$ presents a complicated phase diagram in which subtle changes in oxygen stoichiometry induce structural variations, which could provoke changes in the $La_2NiO_{4+\delta}$ properties. By growing $La_2NiO_{4+\delta}$ thin films on single crystal substrates we expect to have a new point of view, as strains and changes in the film structure will be induced, which could affect their oxygen content and high temperature properties.

Oxygen Diffusion As materials with interstitial transport mechanism have just recently started to be studied as possible candidates for SOFC cathodes, significant efforts have been directed towards understanding the K_2NiF_4-type oxides and, in particular, the $La_2NiO_{4+\delta}$ [24, 50]. In $La_2NiO_{4+\delta}$, an electric field gradient is present between $La_2O_2^{2+}$ and NiO_2^{2-} layers. Therefore, the Coulomb potential

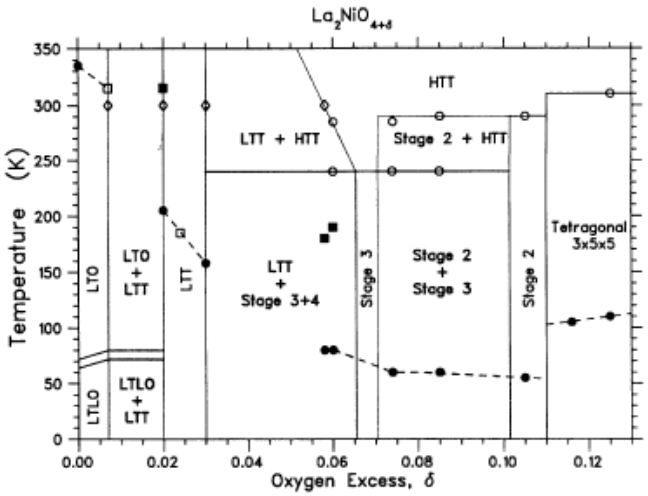

Figure 1.5: Schematic phase diagram of $La_2NiO_{4+\delta}$ (after Refs. [39, 44, 56]).

may prevent the (large) interstitial O^{2-} ions from leaving the $La_2O_2{}^{2+}$ layer, leading to an expected large diffusion anisotropy [24]. Lattice relaxation, atomic volumes evolution, and high oxygen polarizability seem to be the key factors governing direct diffusion mechanisms in this type of compound [51].

It has been proposed by Minervini et al. [50] that the mobility of the oxide ions in these materials occurs mainly through an interstitialcy mechanism in the *a*-*b* plane. Their atomistic simulations allow to study the energetics of oxygen excess accommodation and migration in $La_2NiO_{4+\delta}$. According to their results, the oxygen diffusion should be highly anisotropic, with activation energies such as $E_a(||a\text{-}b) =$ 0.3 - 0.9 eV and $E_a(\perp a\text{-}b) =$ 2.9 - 3.5 eV, depending on whether O_i" or O_i' diffusing species are considered.

A more recent work by Bassat et al. [24], in which the anisotropy of anionic conductivity in $La_2NiO_{4+\delta}$ was experimentally measured on a high-quality single crystal, has reported a surprisingly low activation energy for the transport in the *c*-axis direction. Such a value was not expected on the basis of a mechanism involving O^{2-} interstitial and equatorial oxygen ions. This result is, however, in agreement with the non-stoichiometry model described by Tranquada et al. [44], whereby

antiphase boundaries (APBs) should induce a stabilization of oxygen vacancies in the *a*-*b* plane. They suggest that a mechanism involving the diffusion of smaller O_i^- species via these oxygen vacancies occurs in this direction. This second mechanism, which contribution to the total ionic conductivity is weak, would also occur in the *a*-*b* plane in the low temperature range. On the other hand, the activation energy for the diffusion coefficient vs. T, measured in the *a*-*b* plane ($E_a \approx 0.9$ eV) is of the order of magnitude of the ceramics activation energy. It is in agreement with atomistic calculations, involving a push-pull mechanism with both O^{2-} interstitial and apical oxygen ions along the migration pathway. This in-plane migration of oxygen is the prevailing mechanism, as observed in ceramics. Interestingly, structural strains may be the driving force of the oxygen diffusion for both mechanisms. In this compound, the oxygen excess δ leads to interesting capacities toward both oxygen reduction and efficient O^{2-} diffusion, with better performances than any known perovskite phase [24]. With respect to the application, textured ceramics with *a*-*b* planes perpendicular to the surface are thus much promising.

Electronic Conductivity The electrical conductivity of $La_2NiO_{4+\delta}$ is characterized by a semiconductor-type electronic conductivity, which occurs via hopping of p-type charge carriers between mixed-valence nickel cations, with a small activation energy (typically in the range 50-100 meV) below 600 K [57–60] and showing a maximum between 600 and 700 K above which a smooth apparent change from semiconducting to a metallic-like behavior was observed [43, 58, 61]. Bassat et al. [58] presented convincing evidence for various La deficient $La_{2-x}NiO_{4\pm\delta}$ phases that the increase in resistivity with increasing temperature, previously attributed to a metal-insulator transition at $T > 600$ K, is actually due to oxygen loss and the associated decrease in the number of charge carriers.

The maximum reported conductivity values for polycrystalline bulk ceramics and films (maximum ≈ 80 S/cm) [26, 57, 58, 61–63], and on single crystal samples along the *a*-*b* plane (maximum ≈ 200 S/cm) [59, 64] seem acceptable for using such materials as cathodes of SOFC.

The electrical properties, as expected, are highly anisotropic as shown by studies on single crystals grown by skull melting [65]. Due to this high anisotropy, the

application of this material strongly depends on the capability to prepare highly textured or epitaxial samples.

1.5 $La_{n+1}Ni_nO_{3n+1}$: State of the Art

The homologous series of compounds with the general formula $A_{n+1}M_nO_{3n+1}$ that are structurally similar to the titanates, $Sr_{n+1}Ti_nO_{3n+1}$, reported by Ruddlesden and Popper in 1958 [66], are referred to as Ruddlesden-Popper (RP) phases.

The structure of the RP phases is made up of n consecutive perovskite layers $(AMO_3)_n$, alternating with rock salt layers, with AO along the crystallographic c-axis direction, so their formula can be represented by $(AO)(AMO_3)_n$, where n represents the number of connected layers of vertex sharing MO_6 octahedra. The well-known perovskite (AMO_3) and K_2NiF_4-type structures correspond to n = ∞ and n = l, respectively. Although the perovskite phase ($n = \infty$) is, in general, easily obtained, the higher the value of n, especially $n > 3$, the more difficult the phases are to obtain, due to kinetic factors, as it is complicated to order a structure formed by large perovskite blocks without obtaining any disorder. In rare cases, it is possible to stabilize the $n = 4$ and higher members of the series as a single phase; however, these structures are usually only observed as small defect domains inside the bulk microstructure of the lower n members. In general, the physical properties of the various phases within a series are governed primarily by the width of the perovskite slab (n value), the nature of the A ion, the M-O bond distance, the M-O-M bond angle, and the oxygen content [67]. The physical properties of the $n = 1, 2, 3$ phases are expected to be highly anisotropic.

The average oxidation state of nickel in the system $La_{n+1}Ni_nO_{3n+1}$ (n = 1, 2, 3, ∞) varies from 2+ for $n = 1$ to 3+ for $n = \infty$, and as a consequence the series has been investigated for potential magnetic, electronic, and charge-ordering properties. Different studies on the n = 1, 2, 3, or ∞ phases in the literature evidence that the electronic transport in $La_{n+1}Ni_nO_{3n+1}$ depends to a large extent on the number of perovskite blocks, n, gradually varying from an insulating to a metallic behavior upon increasing n [68–71]. Very recently there has been a renewed interest to study the electronic high temperature properties of these compounds in

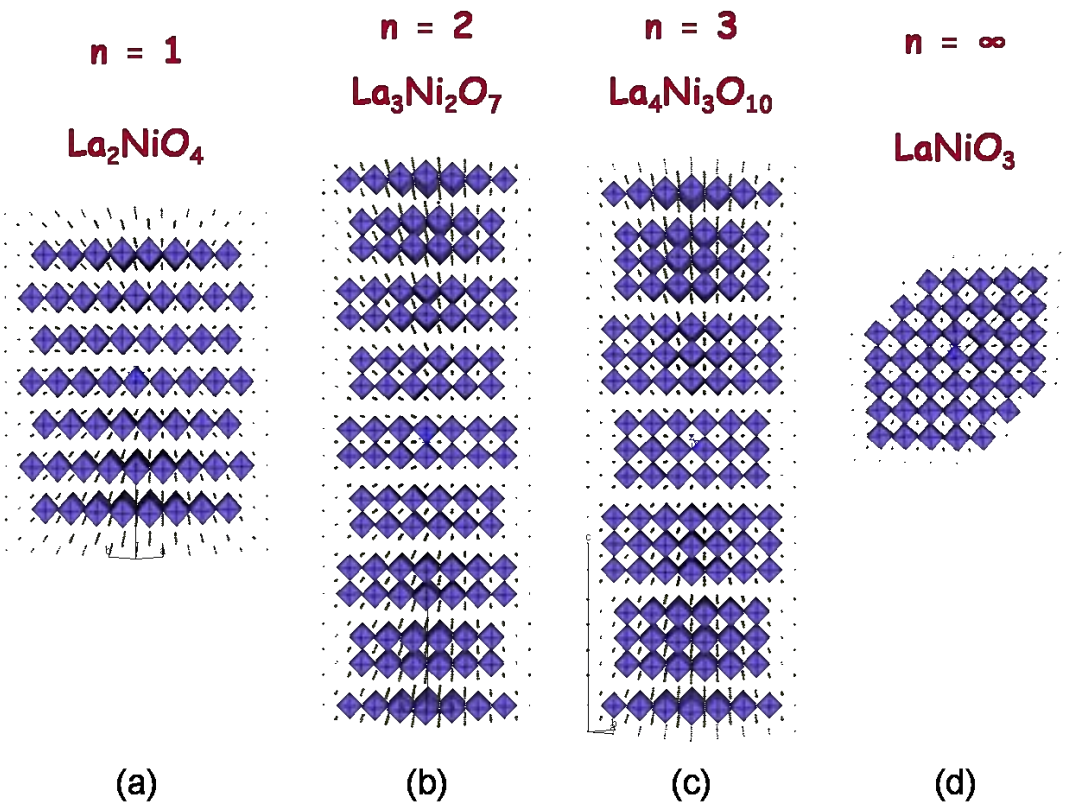

Figure 1.6: The idealized structure of $La_{n+1}Ni_nO_{3n+1}$ phases: (a) $n = 1$, (b) $n = 2$, (c) $n = 3$ and (d) $n = \infty$.

view of their potential application as cathodes for SOFCs [62].

$La_2NiO_{4+\delta}$ is the $n = 1$ member of the $La_{n+1}Ni_nO_{3n+1}$ Ruddlesden-Popper (RP) series (see Figure 1.6) [67, 72], and has been explained in detail in Section 1.4.

Although the $n = 2$ phase $La_3Ni_2O_{7-\delta}$ as synthesized in air is reported to have a slight oxygen defficiency $\delta \approx 0.08$, annealing in high-pressure oxygen gives rise to the stoichiometric $La_3Ni_2O_7$, and annealing in hydrogen increases δ as far as 0.65 [73]. Its structure is reported as orthorhombic *Fmmm* (with only one Ni site) on the basis of Rietveld-refined X-ray powder diffraction (XRD) data [73]. $La_3Ni_2O_{6.92}$ is also reported as *Fmmm*, but the $\delta = 0.35$ phase is tetragonal $I4/mmm$ [73]. Controversy exists concerning the properties of $La_3Ni_2O_7$, probably originated from uncertain oxygen content from sample to sample [69, 73, 74]. Four phases of $La_3Ni_2O_{7-\delta}$

with $\delta = 0$, 0.08, 0.16 and 0.65 can be prepared as shown in Figure 1.7 [73]. The slightly oxygen deficient sample, $La_3Ni_2O_{6.92}$ is semiconducting, while the fully oxygenated $La_3Ni_2O_{7.00}$ is marginally metallic and the fully reduced phase, $La_3Ni_2O_{6.35}$ is semiconducting [73].

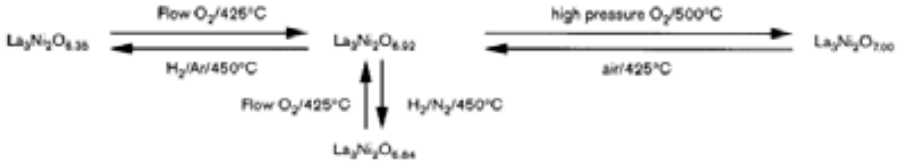

Figure 1.7: Preparation of the four phases of $La_3Ni_2O_{7-\delta}$ with $\delta = 0$, 0.08, 0.16 and 0.65 (after Ref. [73]).

Air-annealed $n = 3$ samples are nearly stoichiometric $La_4Ni_3O_{10}$ [75]. The structure is reported on the basis of Rietveld-refined neutron powder diffraction data as orthorhombic *Cmca* [75]. This *Cmca* structure is distorted from an *Fmmm* parent structure in the same manner as is $La_2NiO_{4+\delta}$, i.e., NiO_6 octahedral rotations. $La_4Ni_3O_{10}$ has metallic conductivity behavior in the whole temperature range with a metal-to-metal transition observed at T $\approx$ 548 K [62, 70].

$LaNiO_3$ ($n = \infty$) crystallizes in the rhombohedrally distorted perovskite-type structure [76–79]. The phase is metallic down to 1.5 K [69].

The room-temperature resistivity decreases from $\rho \approx 250$ mΩ·cm for the $n = 2$ member to $\rho \approx 1.8$ mΩ·cm for the $n = \infty$ member. The Seebeck data suggest that charge transport takes place via both electrons and holes in the case of the $n = 2$ and 3 members, but through electrons in the $n = \infty$ member [69].

1.6 Thin Films of $La_{n+1}Ni_nO_{3n+1}$: State of the Art

Studies concerning the preparation of $La_{n+1}Ni_nO_{3n+1}$ epitaxial films are rather scarce, particularly for $La_2NiO_{4+\delta}$, and have evidenced the difficulty to prepare pure phases, intergrowth defects being common in these compounds, particularly for n > 1 [80].

Satyalakshmi et al. have grown epitaxial $LaNiO_3$ thin films on $LaAlO_3$, (LAO),

$SrTiO_3$, (STO), and YSZ by pulsed laser deposition method using an oxygen partial pressure of 350 mTorr and a substrate temperature of 700 °C. The as-deposited $LaNiO_3$ films are metallic down to 10 K [81]. Other authors have grown epitaxial $LaNiO_3$ thin films on (001) $SrTiO_3$ substrates by laser molecular-beam epitaxy [82], ozone-assisted molecular-beam epitaxy [83] and nebulized spray pyrolysis [84]. The resistivity of the thin film measured in this case was 0.28 mΩ·cm at 278 K and 0.06 mΩ·cm at 80 K, respectively [82]. Finally, very recently another group has deposited epitaxial thin $LaNiO_3$ films onto monocrystalline (1 0 0)-plane oriented $NdGaO_3$ substrates by using a reactive d.c. magnetron sputtering technique.

To our knowledge, the $n = 2$ and $n = 3$ members of the RP family have only been obtained as thin films by Raju et al [85]. Starting with acetylacetonate precursors, they obtained oriented films of metallic $LaNiO_3$ and of near stoichiometric $La_4Ni_3O_{10}$ and $La_3Ni_2O_7$ by Nebulized Spray Pyrolysis .

Polycrystalline $La_2NiO_{4+\delta}$ films with a different degree of orientation have been obtained by a citric acid-based technique [86], by spray pyrolysis [85, 87], sol-gel technique [88, 89] and Pulsed Injection Metal Organic Chemical Vapor Deposition (PIMOCVD) technique [90–92]. However, to our knowledge, there is only a recent report in the literature about high quality c-axis oriented $La_2NiO_{4+\delta}$ epitaxial films deposited by pulsed laser deposition [93].

The possibility of depositing dense films of $La_2NiO_{4+\delta}$ on porous ceramic substrates was studied by spray pyrolysis technique, using an aerosol generated ultrasonically from organic solutions of metal β-diketonate precursors [87] and by complex sol-gel method [88]. Abrutis et al. [87] found that, depending on the oxygen concentration in the aerosol flow, films of dense or porous morphology could be obtained. A porous layer of MIEC materials can be used as a catalytic layer in solid state catalytic devices or as electrodes in SOFC, while dense, gas-tight films on porous substrates can be used as membranes for oxygen separation. The cracking of dense as-deposited or annealed films is the main difficulty in preparing gas-tight membranes. Nevertheless, thin, dense membranes with negligible leakage were successfully prepared on porous substrates. Li et al. [88] also fabricated a dense supported membrane of $La_2NiO_{4+\delta}$ on porous α-Al_2O_3 substrate at 1123 K, which is much lower than the temperature needed for conventional solid-state synthesis. The oxygen flux mea-

sured was around 0.3 ml·cm^{-2}·min^{-1} at 923 K, which is significantly higher than that of the bulk membrane, showing its great potential for the application in both air separation and catalytic membrane reactor.

Smith et al [86] have also studied the use of $La_2NiO_{4+\delta}$ as permeation membranes. They synthesized polycrystalline $La_2NiO_{4+\delta}$ by a citric acid-based technique and measured the steady-state oxygen permeation as a function of oxygen gradient, temperature (850-1000 °C), and membrane thickness (0.3-2.5 mm). The $La_2NiO_{4+\delta}$ membranes show high permeation rates, comparable to those found for the perovskite-related $La_{1-x}Sr_xCo_{1-y}Fe_yO_{3-\delta}$ materials. The self-diffusion coefficient and surface exchange coefficients showed Arrhenius-type behavior with activation energies 40 ± 20 and 110 ± 60 kJ/mol, respectively, in agreement with literature data obtained by $^{16}O_2/^{18}O_2$ exchange/secondary ion mass spectroscopy analysis performed at lower temperatures.

Fontaine et al. [89] presented the development of a reduced-temperature SOFC cathode based on thin films of $La_2NiO_{4+\delta}$ elaborated via a polymeric method. Polycrystalline thin films of $La_2NiO_{4+\delta}$ were synthesized on yttria stabilized zirconia (YSZ) substrates by dip-coating using a polymeric sol. Crack-free films were obtained after sintering in air at temperatures ranging from 800 °C to 1000 °C.

Fabrications of $La_2NiO_{4+\delta}$ thin film layers by liquid-injection metalorganic chemical vapor deposition were investigated by Facheux et al [90–92]. In their first results polycrystalline dendritic layers of $La_2NiO_{4+\delta}$ tetragonal (or orthorhombic) phase were observed on (001) Si substrates while layers of a perovskite-like cubic structure were observed on (001) MgO, (001) $LaAlO_3$ and (001) $SrTiO_3$ single crystal substrates [90]. In subsequent articles by the same group [91, 92] they reported on the synthesis of films presenting an epitaxial growth on three kinds of substrates (MgO (1 0 0), $LaAlO_3$ (0 1 2) and $SrTiO_3$ (1 0 0)) with the (1 1 0) plane of the tetragonal cell of $La_2NiO_{4+\delta}$ parallel to the surface of the substrates and with two other minority orientations with *a*- and *c*- axis perpendicular to the surface. But high resolution TEM analysis revealed that the local structure did not exactly correspond to the ideal structure of the tetragonal $La_2NiO_{4+\delta}$ phase; but to a perovskite-like cubic structure with many planar structural faults corresponding to the LaO layers [92].

To date the only reported conductivity values for $La_2NiO_{4+\delta}$ films correspond to

films grown on $SrTiO_3$ (100) by spray pyrolysis, showing semiconducting behavior at high temperatures consistent with the results on bulk samples [58]. Very recently Kim et al. [93] have reported the synthesis of epitaxial (001) oriented thin film of $La_2NiO_{4+\delta}$ grown on $LaAlO_3$ (001) by pulsed laser deposition (PLD). Electrical conductivity relaxation (ECR) experiments were performed on a 300 nm film showing that the oxygen transport on the film was found to be controlled by surface exchange reaction.

Other authors [94] have synthesized thin films of Sr doped lanthanum nickelate, i.e., $La_{2-x}Sr_xNiO_4$ (0.5<x<1.5) by pulsed-laser deposition (PLD). They obtained *a*- and *c*-axis-oriented epitaxial thin films on $LaSrAlO_4$ (100) and $(LaAlO_3)_{0.3}(SrAl_{0.5}Ta_{0.5}O_3)_{0.7}$ (001) substrates, respectively. Due to the in-plane anisotropy of the lattice mismatch, the lattice parameters of the *a*-axis-oriented films vary with x in a different manner from those of the ceramics. In the *a*-axis-oriented films, resistivity at low temperatures, and optical spectra show large anisotropy between the *b* and *c* axes, indicating the quasi-two-dimensional nature of the electronic structure in $La_{2-x}Sr_xNiO_4$.

To date studies concerning $La_2NiO_{4+\delta}$ thin film preparation and properties studies are summarized in Table 1.2.

Table 1.2: Summary of the studies of thin $La_2NiO_{4+\delta}$ films

Ref.	**Technique**	**Films**		**Doped**	**LTP**	**HTP**			
		Poly	Epi			σ	OP	ECR	IE
[87]	spray pyrolis	X							
[88]	sol gel	X					X		
[86]	citric-acid based	X					X		
[89]	dip-coating	X							
[90]	PI-MOCVD	X							
[91, 92]	PI-MOCVD		X (?)		X				
[85]	spray pyrolysis	X				X			
[93]	PLD		X					X	
[94]	PLD		X	X	X				

Poly = Polycrystalline; Epi = Epitaxial;
LTP = Low Temperature Properties; HTP = High Temperature Properties;
σ = Conductivity ; OP = Oxygen Permeation;
ECR = Electrical Conductivity Relaxation; IE = Isotope Exchange

It can be noticed that, even though $La_2NiO_{4+\delta}$ thin films have been prepared and some of their properties studied by several groups, a complete study of thin films has not yet been described.

In this thesis we have attempted to do a complete study of the growth, microstructure and high temperature properties of *c*-axis oriented epitaxial $La_2NiO_{4+\delta}$ thin films. We have therefore deposited $La_2NiO_{4+\delta}$ thin films of different thickness on two different substrates, in order to induce strain in opposite directions, and we have studied the effect of the strain in the $La_2NiO_{4+\delta}$ structure (cell parameters) and in the high temperature transport properties: total conductivity, oxygen transport and surface exchange.

Chapter 2

PI-MOCVD Deposition Technique

2.1 Introduction to Chemical Vapor Deposition (CVD)

The Chemical Vapor Deposition (CVD) process consists in a chemical reaction of gaseous species which takes place on or near a substrate surface producing a solid material, which forms the film. The reaction gaseous products are evacuated from the deposition zone by a gas flux.

Although CVD has been used to produce ultrafine powders, it is mainly a deposition technique for films and coatings. Therefore, we will center the description of the technique for these applications.

The conventional CVD method, so called thermal activated CVD (TACVD), uses thermal energy to activate the chemical reactions. Depending on the pressure value in the reaction environment, there are two main classes of thermal CVD: atmospheric pressure CVD and low-pressure CVD (usually 0.01-100 Torr) [95]. However, the CVD reactions can also be initiated using different energy sources. This has given rise to other variants of CVD methods such as plasma enhanced CVD (PECVD) and photo-assisted CVD (PACVD) which use plasma and light, respectively, to activate the chemical reactions. Atomic Layer Epitaxy (ALE) is a special mode of CVD where a monoatomic layer can be grown in sequence by sequential saturating surface reactions. Such CVD variants are useful for the controlled growth of epitaxial films,

and the fabrication of tailored molecular structures. Other variants of CVD include metalorganic CVD (MOCVD) which uses metalorganic as the precursor rather than the inorganic precursor used in the conventional CVD method. Other CVD variants such as pulsed injection MOCVD and aerosol assisted CVD use special precursor generation and delivery systems, unlike conventional CVD. Flame assisted vapor deposition (FAVD) uses a flame source to initiate the chemical reaction and/or heating the substrate. Electrochemical vapor deposition (EVD) is another variant of CVD that is suitable for the deposition of dense films onto porous substrates [96].

The variety of chemical precursors used in the CVD systems is very wide. The most important reactive families for obtaining ceramic materials are:

- *metal carbonyls*, such as $Fe(CO)_5$ for Fe deposition;
- *metal hydrides*;
- *halides*, very reactive, they hydrolyze spontaneously at room temperature and need extreme storage and handling security precautions;
- *halohydrides*, such as $SiCl_2H_2$ which reacts with NH_3 for Si_3N_4 deposition;
- *metalorganic compounds*, which due to their special characteristics are used for the MOCVD technique (*Metalorganic CVD*), also named OMVPE (*organometallic vapor phase epitaxy*), as it is commonly used to obtain of epitaxy of semiconductor compounds.

Generally, metal halides and halohyrides are more stable than the corresponding hydrides. The metalorganic precursors offer the advantage of lower reaction and deposition temperatures than halides and hydrides and are less toxic and pyrophoric. Therefore, they are gaining wider application especially in the deposition of II-VI and III-V semiconductors, as well as high-T_c superconductors.

Although CVD is a complex chemical method, it has the following distinctive advantages:

(a) The capability of producing highly dense and pure coatings.

(b) It produces uniform films with good reproducibility and adhesion at reasonably high deposition rates.

(c) CVD can be used to uniformly coat complex shaped components and deposit films with good conformal coverage (low-pressure CVD). This is a distinct characteristic of CVD processes, in contrast to physical vapor deposition techniques.

(d) CVD can be used to deposit large surfaces and diverse shapes, compared with Physical Vapor Deposition (PVD) methods.

(e) It has the ability to control crystal structure, surface morphology and orientation of the CVD products by controlling the CVD process parameters.

(f) Deposition rate can be adjusted readily. Low deposition rate is favored for the growth of epitaxial thin films.

(g) Reasonable processing cost for the conventional CVD technique.

(h) The flexibility of using a wide range of chemical precursors such as halides, hydrides and organometallics, which enable the deposition of a large spectrum of materials including, metal, carbides, nitrides, oxides, sulphides, III-V and II-VI materials.

(i) Relatively low deposition temperatures (500-1000 °C), which enables the deposition of refractory materials at a small fraction of their melting temperatures.

However, the drawbacks of CVD include:

(a) Chemical and safety hazards caused by the use of toxic, corrosive, flammable and/or explosive precursor gases. This limitation is generally overcome with metalorganic precursors.

(b) Difficulty to deposit multicomponent materials with well controlled stoichiometry using multi-source precursors because different precursors have different vaporization rates. However, this limitation can be overcome using single source chemical precursors or using the Pulsed Injection technique.

2.2 Metalorganic Chemical Vapor Deposition Technique (MOCVD)

As previously mentioned, Metalorganic Chemical Vapor Deposition (MOCVD) is a variant of CVD, which has been classified according to the use of metalorganics as precursors. MOCVD can be used to deposit a wide range of materials as almost every metallic element has a known volatile organometallic compound.

There are four categories of metalorganic compounds frequently used: β- diketonates, such as 2,2,6,6-tetramethyl-3,5-heptanedionate (thd) and 2,4-pentanedionate (also known as acetylacetonate, acac); alkoxides, such as ethoxide, isopropoxide, and butoxide; alkylmetal, such as ethylzinc and phenylbismuth; and carboxylates, such as benzoate and ethylhexanoate.

The selection criteria of a suitable chemical precursor for coating applications are the following [96]:

(a) Commercial availability of high purity compounds.

(b) Low toxicity, explosiveness and non-inflammability.

(c) Stability at room temperature.

(d) Low vaporization temperature. Similar vaporization temperatures for different precursors in multicomponent systems.

(e) Constant vapor pressure larger than 10^{-1} Torr, maintained at a constant temperature. In some cases, for very volatile compounds, refrigeration systems are required.

In general, the CVD process involves the following key steps:

1. Generation of active gaseous reactant species.
2. Creation of a gas mixture containing the precursor elements.
3. Transport of the gaseous species into the reaction zone.

4. Activation of the necessary chemical reactions needed for obtaining the desired solid product.

5. Gaseous by-products are removed from the boundary layer through diffusion or convection.

6. The unreacted gaseous precursors and by-products will be transported away from the deposition chamber.

As to the film formation process, it can be subdivided in five steps, as is shown in figure 2.1:

1. Diffusion of the precursor molecules towards the boundary region in contact with the substrate.

2. Gaseous reactants undergo gas phase reactions forming intermediate species (pyrolysis).

3. Adsorption and superficial diffusion of the intermediate species.

4. Nucleation and growth processes. Steps 3 and 4 are common to all the physical and chemical vapor phase crystal growth techniques.

5. Recombination of the exhaust gases and desorption of the gas phase.

Kinetics of the process

CVD tends to be a non-equilibrium process. The kinetics of a CVD process involves chemical reactions in the gas phase, on the substrate surface, chemisorption and desorption. Ideally, the chemical kinetics of a CVD process could be derived from the analysis of all possible reaction pathways including those sequential and competing reactions. Surface reactions and chemical reactions in the gas must ideally be described by their formula, and followed by their rate equations. The overall reaction rate is limited by the slowest reaction step. Three different cases can be distinguished [96]:

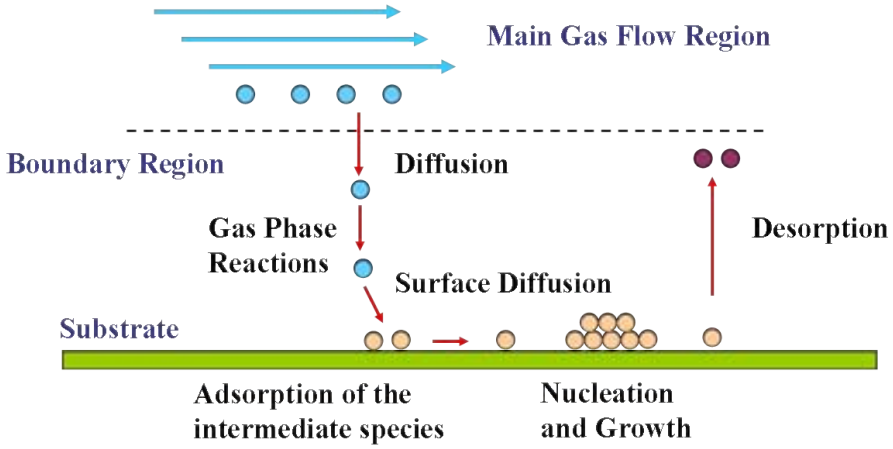

Figure 2.1: Film growth process from metalorganic molecules.

1. At low temperatures, the reaction rate is very slow compared with the diffusion transport rate: in this case the growth rate is limited by the reaction kinetics. Therefore the growth rate depends on the temperature following Arrhenius law:

$$k = k_o e^{(\frac{-E_a}{RT})} \tag{2.1}$$

where k_o is a kinetic rate constant, E_a is the apparent activation energy, R is the universal gas constant and T is the deposition temperature.

2. At higher temperatures, the reaction rate at the surface is very high, consequently the growth rate is limited by the transference rate of the reactive species to the substrate. In this case we work in a diffusion controlled regime. As the diffusion processes are quite independent from the temperature, the growth will not vary much when the temperature increases.

3. At even higher temperatures a decrease in the growth rate is observed due to a desorption phenomenon. By increasing even more the temperature an homogeneous reaction in gas phase can occur in addition to the heterogeneous reaction on the substrate surface. This process gives rise to the formation of

particles in the gas phase and to the reduction of the film growth and will, therefore, affect the microstructure and the adherence of the films. In Figure 2.2 the film growth rate is represented vs. the temperature for each of these regimes.

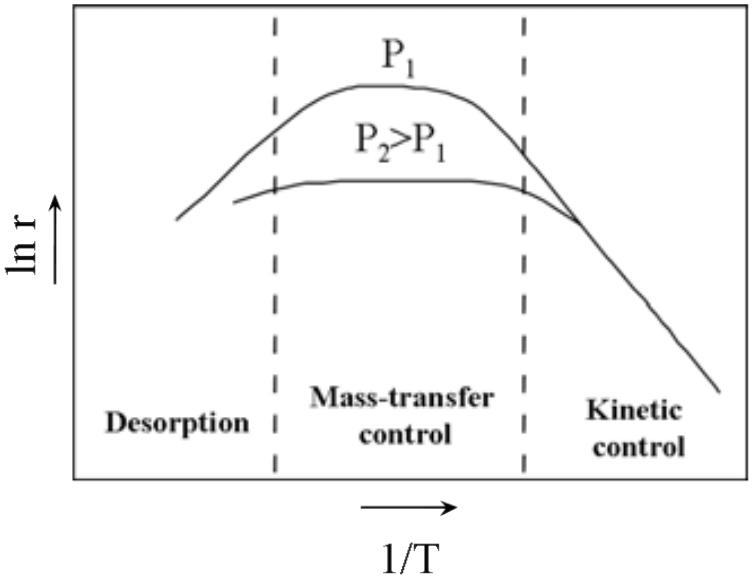

Figure 2.2: Arrhenius plot of the film growth rate (r) as a function of temperature (T).

In diffusion controlled processes, the gas flux diffused is inversely proportional to the pressure square root. Hence, the growth rate increases as the total pressure decreases, being between 1 to 2 orders of magnitude higher in low pressure CVD (LPCVD) reactors (which work at pressures between 0.1 and 10 Torr) compared to atmospheric pressure CVD (APCVD) reactors.

At high temperatures the desorption process becomes important, specially for low total pressures, and has the effect of decreasing the film growth rate, as can be observed in Figure 2.2. In systems that work at high gas precursor partial pressures, as in the case of atmospheric reactors, gas phase homogeneous nucleation can occur, which increases with increasing temperatures. The formation of solid microparticles in the gas phase produces a decrease in the film growth rate in addition to the contamination with microparticles, which can precipitate on the film during the

growth process giving rise to a change in its structure. In LPCVD systems this phenomenon is largely attenuated.

2.3 Description of the Pulsed Injection MOCVD

The conventional MOCVD technique presents some difficulties for the deposition of multicomponent oxides or multilayers, as the synthesis of high quality films requires the introduction in the reactor zone of a very stable vapor phase with a high control of the precursor composition. The low thermal stability of some organometallic compounds (such as Ba, and rare earth elements) due to hydrolysis or polymerisation and the difference in vapor pressures from one precursor to another in multielement systems, reduce the evaporation rate with time. This reduction leads to difficulties in the vapor phase composition control and, consequently, in the deposition of films with the correct stoichiometry. In the same way, many of the most commonly used metalorganic precursors are solid, thus the control of their evaporation rate depends on the aggregation state of the powder, and on other geometrical factors of the evaporator (which affect the gas flow).

Senateur and co-workers [97] developed ten years ago the "Pulsed Injection Metal Organic Chemical Vapor Deposition" (PI-MOCVD). The new technique consists in the sequential injection of micro-droplets (e.g. some microliters) of a solution of the organometallic precursor in an evaporation zone by means of a high-speed electrovalve (Figure 2.3). The injection rate control is relatively simple and versatile, by using two control parameters: frequency (1-100 Hz) and valve aperture time (2-8 ms).

The advantages of the Pulsed Injection MOCVD compared with the conventional MOCVD are:

- The thickness, stoichiometry and growth rate of the film can be controlled with great precision, as the precursor flux is controlled simply by the valve aperture time, electrovalve injection frequency, number of droplets and the precursor concentration of the solution.
- The precursors are maintained under an inert atmosphere and at room temperature, permitting the use of thermally non-stable precursors.

Figure 2.3: High-speed electrovalve.

- It is possible to obtain combinations of complex composition from one sole multicomponent solution.
- It is possible to use several injectors with different solutions to obtain multilayers and superlattices [98, 99].
- The reproducibility of the deposited layers are enhanced using the pulsed injection MOCVD.

2.4 Film Deposition Process and Optimization

The preparation of the lanthanum nickelate films has been performed using a Pulsed Injection MOCVD system, which was previously built and tested in our laboratory. The experimental equipment is shown in Figure 2.4.

Solid β-diketonates La(thd)$_3$ and Ni(thd)$_2$ (thd = 2,2,6,6-tetramethylheptane-3,5-dionate) from Strem Chemicals were solved in 1,2-dimethoxyethane and used as precursors. The electrovalve, which in our case is a simple vehicle fuel injector, is electronically controlled and injects precise microdoses of organic solution with the precursor mixture at the required concentration. The injected liquid volume was fixed to an aperture time of 2 ms and the pulse frequency was varied from 0.5 to 1 Hz. To assure the reproducibility of the droplets volume, the solution is under an overpressure of 0.7 bar. The evaporation temperature was fixed to 280 °C. After the flash evaporation, the precursors and solvent vapors are rapidly carried by the

Figure 2.4: Pulsed Injection MOCVD system.

flow of Ar towards the substrate. Oxygen, used as reactive gas, is introduced from the bottom of the reactor. The total gas flow was varied between 1 and 1.33 l/h with different ratios of oxygen and argon. The chosen solvent is very volatile, thus obtaining its vaporization previously to that of the precursors. As a result a physical separation of the precursors and solvent in the gases is obtained. The PI-MOCVD reactor has a T-shape geometry (Figure 2.5). Two injectors can be connected to the stainless steel evaporator (Figure 2.6).

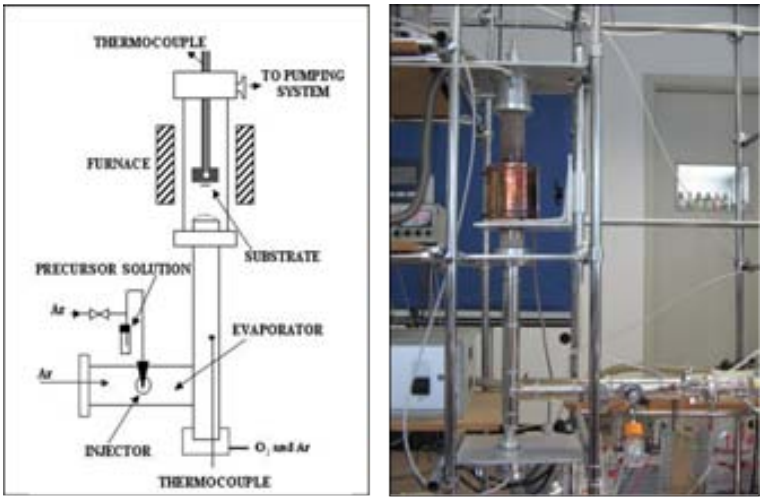

Figure 2.5: T-shape geometry PI-MOCVD reactor.

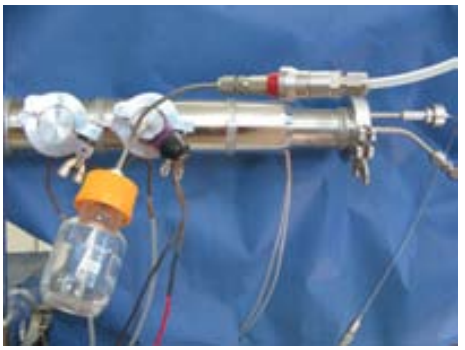

Figure 2.6: Evaporation zone.

To prevent the precursor condensation before reaching the reaction zone there is a second thermocouple in the intermediate zone, which permits the adjustment of the temperature slightly above the evaporation temperature. Before reaching the reaction zone the gases go through a diffusor which makes possible to obtain a uniform gas flow in the region. Previous tests have shown a uniform film thickness deposition over a 20 mm diameter substrate. The substrates are adhered to a metallic stainless steel susceptor facing down, perpendicularly to the gas flow direction, which comes from the bottom of the reactor. Inside the susceptor a thermocouple is introduced, with the end very close to the substrate. The evaporator zone and the transport path are heated by means of external electric heaters and the reaction zone by a tubular resistive furnace, which can reach temperatures up to 900 °C. Both ends of the reactor are connected to the gas and pump lines, which are controlled by mass flow controllers and pump systems, respectively. During the deposition experiment the gas flows upwards, while the evacuation is done from the top and, once the experiment is finished, the gas flow and pumping directions are inverted, preventing a non-controlled residual deposition on the substrate surface.

A previous study made with this equipment and concerning the preparation of Co_3O_4 films [100, 101] allowed us to define the experimental parameters value range and perfectly define and control the deposition process to obtain uniform thin films. From these tests it was concluded that when the working pressure is increased (e.g. up to 30 Torr), the growth rate of the deposited films decreases and less oriented films were obtained. Therefore, the reactor total pressure was maintained at 10 Torr, limiting the pumping rate of the vacuum rotatory pump by means of a regulation valve.

Droplet control and reproducibility studies were also performed, first externally and subsequently by injecting the precursor solution inside the PI-MOCVD system under the experimental conditions. The droplet volume value increases from 7 to 11 μl/droplet as the opening time of the valve is varied from 2 to 3 ms. It has been demonstrated that the droplet volume is not particularly affected by the number of droplets injected in the system, as shown in Table 2.1, in which mean droplet volume values have been measured for lanthanum nickel oxide deposition experiments of different duration. A droplet volume variation, coming from the difficulty controlling

Table 2.1: Mean droplet volume values

Number of droplets injected	**Mean droplet volume (μl/droplet)**
125	8.1
250	6.5
400	8.0
500	6.4
600	6.7
1000	7.4
1500	7.9
2000	7.1

the bottle overpressure in our system, has been detected. By varying the injection frequency from 1 to 2 Hz the film growth rate per precursor solution injected decreases, and less oriented phases are obtained. Therefore, a injection frequency of 1 Hz has been preferred in all cases.

In summary, the main selected experimental parameters are:

- Total pressure: 10 Torr
- Valve opening time: 2 ms
- Injection frequency: 1 Hz

2.5 Characterization of the Metalorganic Precursors

Solid β-diketonates La(thd)$_3$ and Ni(thd)$_2$ (thd = 2,2,6,6-tetramethylheptane-3,5-dionate) (Figure 2.7) from Strem Chemicals were dissolved in 1,2-dimethoxyethane and used as liquid precursors.

Preliminary ex-situ studies, consisting in thermogravimetric analyzes (TGA), carried out under argon at atmospheric pressure, were done to assess the volatility and correct vaporization process of the precursors.

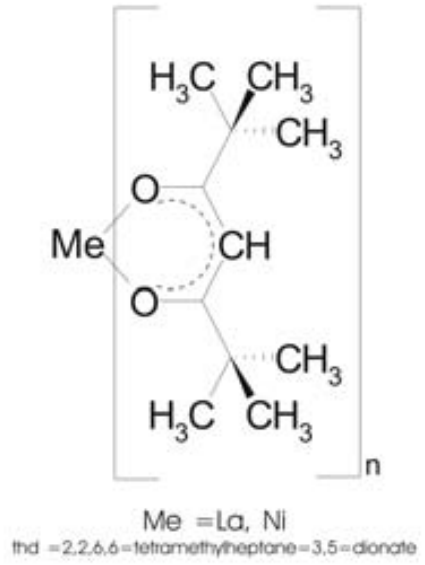

Figure 2.7: Precursors used: $La(thd)_3$ and $Ni(thd)_2$.

Thermogravimetric analyzes (TGA) allow to determine weight changes on a sample as a function of temperature and time for a particular gas atmosphere. A precisely known mass of the sample (with a weight of 5-70 mg) is heated in a controlled way in the thermobalance, while the change of weight is measured and registered.

TGA experiments were carried out in a Perkin Elmer TGA 7 balance with a maximum sensibility of 0.1 μg. The temperature was increased from room temperature to 400 °C at a rate of 2 °C/min with an argon flow of 75 ml/min.

Figure 2.8 displays TG curves under Ar for $La(thd)_3$ and $Ni(thd)_2$. In the case of $La(thd)_3$ (Figure 2.8.a), a two-step evaporation process is observed. The first step around 170-180 °C represents a small mass loss, probably due to impurities in the precursors. A second mass loss in the temperature range of 200-310 °C is observed, giving a total residue of less than 5% of the initial mass, very similar to the results reported by Bedoya et al. [102]. The low residue indicates that the complex evaporates almost completely under atmospheric pressure. The TG analysis of the same precursor after a long storage period in air and at room temperature gave similar result to the "fresh" precursor analysis, confirming its high stability and

inertness.

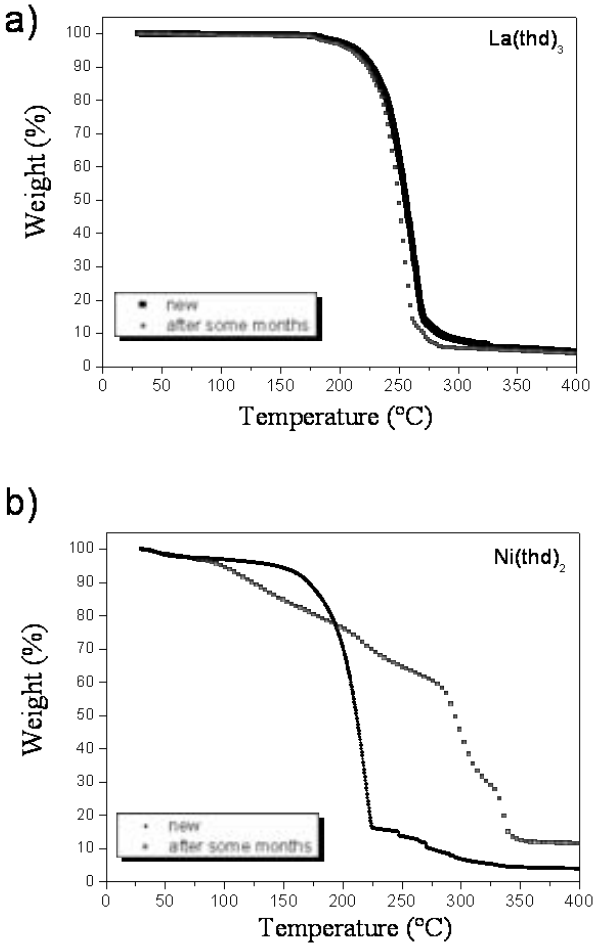

Figure 2.8: TGA representation of the $La(thd)_3$ and $Ni(thd)_2$ precursors in Ar at atmospheric pressure.

On the contrary, the thermal analysis of the $Ni(thd)_2$ precursor showed a quite different behavior. As can be seen in Figure 2.8.b, the precursor presents a first mass loss around 60 °C, which could either be due to a loss of absorbed water, as this precursor is highly hydrophilic, or to the evaporation of hexane (precursor synthesis residue), as previously observed by Lane et al. [103] in a $Ni(thd)_2$ precursor

synthesized by Inorgtech. A second evaporation process appears between 115-220 °C, after which a considerable quantity of material is still present in the thermobalance. Only after heating up to 325 °C the total decomposition takes place, giving a residue of around 4% of the initial mass. The weight loss between 115-220 °C is probably due to a partial decomposition during heating. The initial purple color of the $Ni(thd)_2$ product had turned into a green and more compact powder for the precursor which had been exposed to air during a long period of time. A more complex decomposition is detected in the TGA of the air-exposed precursor, with an enhanced evaporation between 115-220 °C and with higher temperatures needed to reach the following evaporation steps, sign of a possible degradation of the $Ni(thd)_2$ precursor. In that case, more than 10% of residue remained after heating up to 400 °C.

To avoid contact with ambient air and steam, responsible for the nickel precursor degradation, this precursor has been stored separately in vacuum sealed pockets.

The results obtained in the TGA analyzes have helped us to fix the evaporation temperature at 280 °C, well above the $Ni(thd)_2$ decomposition takes place, but ensuring the total evaporation of $La(thd)_3$. As the TGAs have been performed in atmospheric pressure and the precursor evaporation is performed at 10 Torr, it is known that this low pressure will enhance the evaporation process. Instantaneous and total volatilization of the precursor solution is thus expected to occur in the evaporation zone of our system.

Chapter 3

Film Characterization Techniques

3.1 Surface Morphology Characterization

3.1.1 Scanning Electron Microscopy (SEM)

Electron microscopes are based on electron-solid interactions. Depending on their nature, we can classify electron microscopy in different techniques summarized in figure 3.1: Auger electron spectroscopy (AES), cathodoluminescence (CL), scanning electron microscopy (SEM), energy dispersive X-ray spectroscopy (XEDS), electron diffraction (ED), transmission electron microscopy (TEM), electron energy loss spectroscopy (EELS) and scanning-transmission electron microscopy (STEM).

We have used three of these techniques: the scanning electron microscopy (described in this section), the electron diffraction (ED) and the transmission electron microscopy (described in section 4.3 on page 72).

The Scanning Electron Microscopy (SEM) technique consists mainly of a high energy (1-30 keV) electron beam which is scanned across the surface of a sample, which has to be electrically conductive. Insulating samples should be coated with a carbon or gold film to permit the electrical current circulation, or lower voltages should be used (1-5 keV). The incident electrons cause low energy secondary electrons to be generated, and some escape from the surface. The secondary electrons

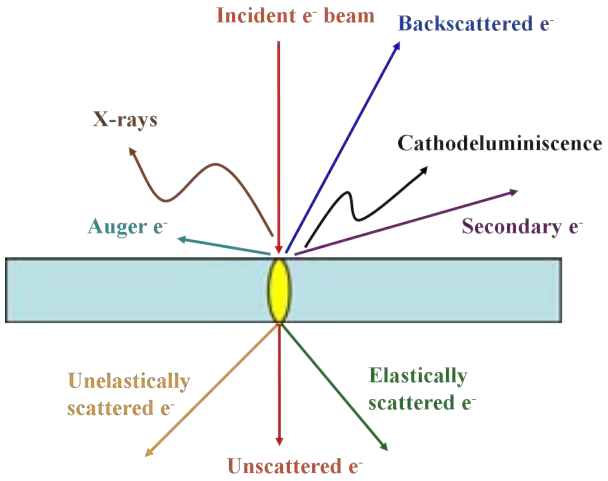

Figure 3.1: Interaction of the electron beam with the specimen leading to the different electron microscopy techniques.

emitted from the sample are detected providing an image of the superficial morphology. The signal of the backscattered electrons permits obtaining a qualitative image of the zones with different mean atomic number, and gives therefore an image of the "chemical composition" of the film. The X-ray signal gives spectra and images of the chemical composition of the sample.

Different microscopes were used and are listed below:

- *Hitachi S-570* with 3.5 nm of resolution, which can be operated between 0.5 and 30 kV. It is located at the Microscopy Service of the Autonomous University of Barcelona.

- *JEOL JSM-6300* with 3.5 nm of resolution, this microscope is connected to a LINK ISIS-200 Energy Dispersive X-Ray (EDAX) analysis spectrometer, which allows qualitative and semi-quantitative element detection. Even though we tried to perform a semi-quantitative analysis of our samples, the results were not satisfactory. The signal of the elements from the thin film is very weak and the results were not quantitatively meaningful. Moreover, there was an overlapping at 4.65 keV between the La_{L_α} peak of the film with a peak corresponding the Ti of the $SrTiO_3$ substrate and also at 5 keV between the

La_{L_β} peak of the film with a peak corresponding to Nd from the $NdGaO_3$ substrate. Therefore a not very intense peak ($La_{L_{\beta_2}}$) had to be chosen as reference for the La. Consequently, for the composiiton analysis we used a Wavelength Dispersive Spectrometer (WDS) described in Section 3.2.1.

This microscope is located at the Microscopy Service of the Autonomous University of Barcelona.

- *Phillips 515* with a 5 nm resolution which can be operated between 0.2 and 30 kV and which is located at the Materials Science Institute of Barcelona (ICMAB-CSIC).

3.1.2 Atomic Force Microscopy (AFM)

Atomic Force Microscopy (AFM), introduced by G. Binnig et al. [104] in 1986, was inspired by the Scanning Tunnelling Microscope (STM), which is based on placing an atomically sharp tip sufficiently close to the surface of a conducting sample so that electrons can tunnel between tip and surface. The tunnelling current as a function of position of the tip provides a three dimensional image that reflects the electronic structure of the uppermost surface atoms. In AFM, not the current, but the atomic force between tip and surface is measured. The AFM tip is situated at the end of a cantilever, the deflections of which are being measured with picometer resolution. In the original design a STM tip was used for this purpose, today optical methods are mainly employed to detect the small deflections of the cantilever. By moving the tip over a sample, a three-dimensional view of the surface topography is obtained with a lateral resolution of down to $\approx$ 1 nm and a vertical resolution of down to $\approx$ 0.01 nm. The actual resolution will be limited by the sharpness, i.e. the end radius, of the tip. AFM can be operated in a contact and a noncontact mode. In its repulsive "contact" mode, the instrument lightly touches the tip at the end of a cantilever to the sample. As a raster-scan drags the tip over the sample, the vertical deflection of the cantilever is measured, which indicates the local sample height. Thus, in contact mode the AFM measures hard-sphere repulsion forces between the tip and sample. In noncontact mode, topographic images are derived from the measurement of attractive forces, while the tip does not touch the sample. AFM enables an

accurate determination of surface roughness, grain sizes and shapes. An advantage of the method is that all analyzes can be conducted in air without any special sample preparation. Even soft materials such as polymers or biological specimens can be imaged. The versatility of AFM further allows the measurement of a variety of different forces, including magnetic interactions and friction [104]. In our case we opereted in contact mode AFM using a PicoSPM from Molecular Imaging located in the Materials Science Institute of Barcelona (ICMAB-CSIC).

3.1.3 Optical Profilometry

An optical profilometer measures surface roughness by means of optical interferometry, the interference and non-interference of monochromatic light as it reflects from the surface. This technique allows obtaining of topographic mapping with a depth resolution down to 1 nm. Since the measurements are based on the optical properties reflected from a surface, the optical properties of each surface must be homogeneous for the whole measured area. In many cases it may be necessary to coat the sample with Au to maintain uniform optical properties across the specimen. We have used the noncontact-type Zygo NewView 200 profilometer, which operates using white light interferometry, located in the Materials Department of the Imperial College (London). We obtained images of the surface of the $La_2NiO_{4+\delta}$ thin films measured by the isotope exchange depth profile method (IEDP) (explained in Section 3.4.3) and we measured the depth of the craters obtained from the nitrogen ion beam sputtering during the ^{18}O concentration profiles measurement by SIMS technique (Figure 3.2).

3.2 Compositional Analysis

3.2.1 Electron Microprobe

The Electron Probe Microanalysis (EPMA) is an elemental analysis technique which uses a focused beam of high energy electrons (5 - 30 keV) to non-destructively analyze a solid specimen surface (including thin films and particles) for inducing emission of characteristic X-rays (0.1 - 15 keV). The X-ray spectrum is obtained at different primary electron energies, E. The higher the value of E the deeper the

Figure 3.2: ZYGO Newview Interferometer.

electrons penetrate into the specimen. This increases the relative line intensities in the spectrum in favor of the substrate lines. Line intensities in EPMA are usually related to spectra taken from reference specimens under same conditions to obtain so-called K-values. This eliminates instrumental parameters. For thin film analysis the K-values are plotted against E and fitted using calculated K-values with the thickness and composition as free parameters.

A microprobe is basically an electron microscope that has been optimized to produce a very stable electron beam that remains focused on one spot rather than scanning over a sample as the more common SEMs (Scanning Electron Microscopes) do. Detection limits are of the order of 100 ppm with wavelength dispersive spectrometry (WDS) and 1000 ppm with energy dispersive spectrometry (EDS). For the analysis of our films we have used a Cameca SX-50 Microprobe (with four crystal analyzers for WDS and one EDS spectrometers) located in the University of Barcelona Technical Services (SCT-UB). The typical voltages used were 12, 15 and 20 keV, and the lines analyzed were K_a for Ni and O, L_a for La for films deposited on STO and L_b for La for films deposited on NGO, as there is an overlapping between the La L_a and the Nd L_l lines. A thin film analysis program (STRATAGem) was used to determine the exact composition and thickness of the thin films without interference

of the substrate composition.

3.2.2 Secondary Ion Mass Spectrometry (SIMS)

Secondary Ion Mass Spectrometry (SIMS) is the most sensitive of all the commonly-employed surface analytical techniques; this is because of the inherent sensitivity associated with mass spectrometric-based techniques. In SIMS the surface of the sample is subjected to bombardment by high energy ions, which leads to the ejection (or sputtering) of both neutral and charged (+/-) species from the surface. The ejected species may include atoms, clusters of atoms and molecular fragments. These secondary ions are measured with a mass spectrometer to determine the quantitative elemental or isotopic composition of the surface (see Figure 3.3).

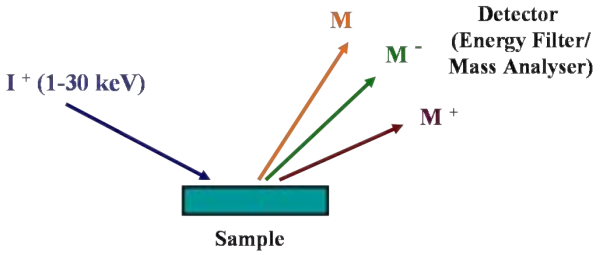

Figure 3.3: Secondary Ion Mass Spectrometry basics.

Detection limits for most trace elements are between 10^{12} and 10^{16} atoms per cubic centimeter. Achievable detection limits are highly dependent on the type of instrumentation used, the primary ion beam used and the analytical area, among other factors. Depending on the current (pulsed or continuous) and dimensions of the primary ion beam (often Cs^+, O^- or Ga^+) then the analysis may be extremely surface sensitive or could go very deep into the sample, eroding a crater in real time.

In the field of Surface Analysis, it is usual to distinguish Static SIMS and Dynamic SIMS. Static SIMS is the process involved in surface atomic monolayer analysis, usually with a pulsed ion beam and a time of flight mass spectrometer, while Dynamic SIMS is the process involved in bulk analysis, closely related to the sputtering process, using a DC primary ion beam and a magnetic sector or quadrupole mass spectrometer.

The ^{18}O and ^{16}O concentration depth profiles of samples after having been exchanged in a ^{18}O-rich atmosphere have been measured using two different Dynamic SIMS instruments:

- An Atomika 6500 quadrupole-based analyzer, sputtering normally with a nitrogen primary ion beam (N_2^+) at 1.25 keV (Figure 3.4).

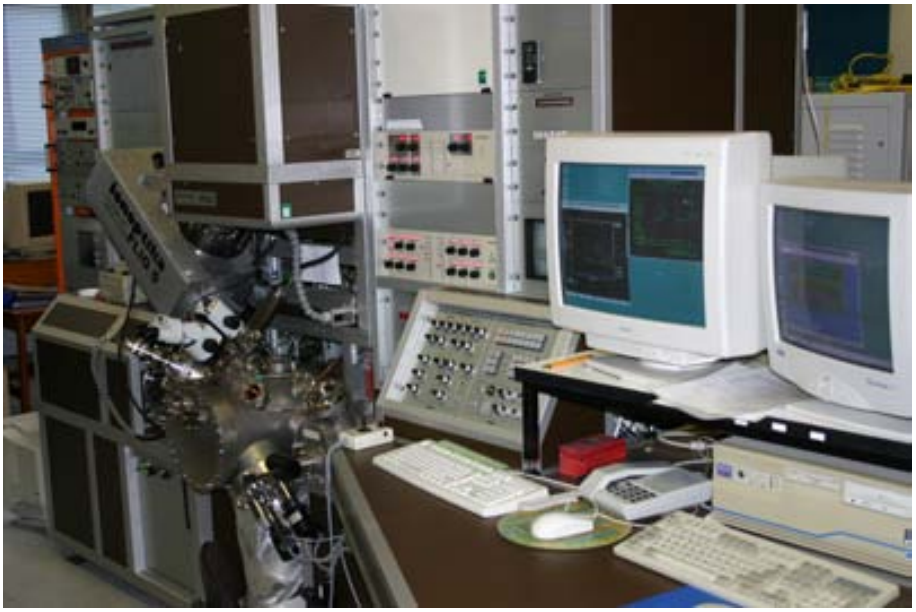

Figure 3.4: Atomika 6500 quadrupole-based analyzer.

- A FEI FIB200 TEM instrument coupled to a SIMS detector. In this case the Focused Ion Beam (FIB) milling uses a focused Ga^+ beam of 30 keV (Figure 3.5).

Both instrument are located in the Materials Department of the Imperial College (London).

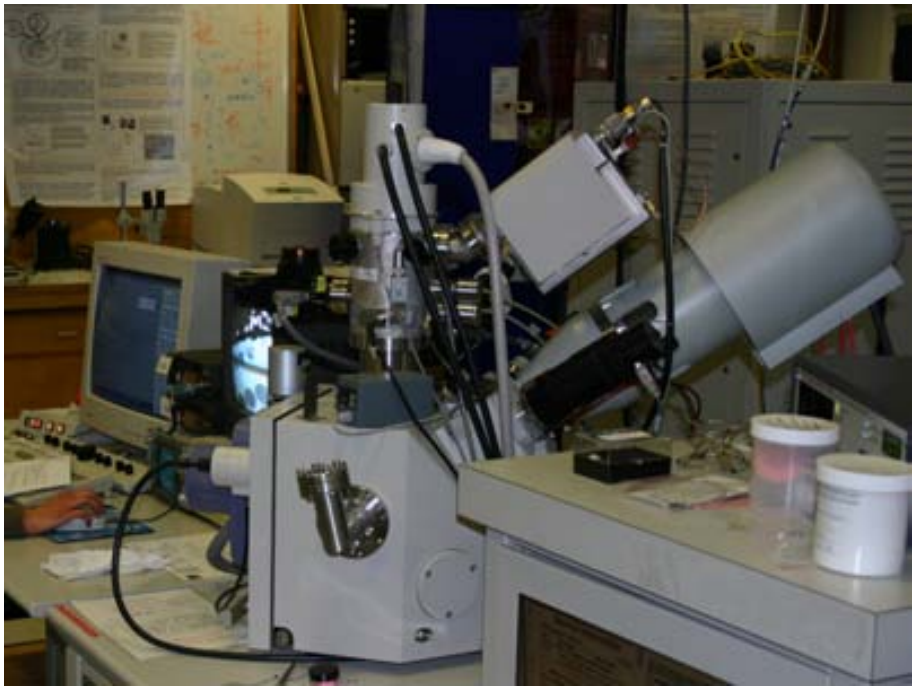

Figure 3.5: FEI FIB200 TEM instrument coupled to a SIMS detector.

3.3 Structural and Microstructural Characterization

3.3.1 X-Ray Diffraction (θ-2θ)

The structural characterization of the films has been performed by X-ray diffraction. XRD is a routine technique in materials science in the elucidation of structures and also to verify phase purity.

Interaction of X-rays with a sample creates secondary "diffracted" beams (actually generated in form of cones) of X-rays related to interplanar spacings in the crystalline powder according to a relation called Bragg's Law

$$2dsin\theta = n\lambda \tag{3.1}$$

derived by the English physicists Sir W.H. Bragg and his son Sir W.L. Bragg in 1913 to explain why the cleavage faces of crystals appear to reflect X-ray beams at certain angles of incidence (theta, θ). The variable d is the distance between atomic layers in a crystal, and the variable lambda λ is the wavelength of the incident X-ray beam (see Figure 3.6); n is an integer.

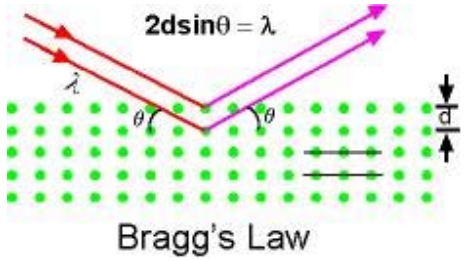

Figure 3.6: Schematic description of Bragg's law.

Diffractometers come in two basic varieties: θ-θ in which the X-ray tube and detector move simultaneously (Bragg-Brentano geometry) or a θ-2θ in which the X-ray tube is fixed, and the specimen moves at 1/2 the rate of the detector to maintain the θ-2θ geometry.

The "angle" of the diffraction (recorded as 2θ by convention) is related to the interplanar spacing, d, by the Bragg law, and the intensity of the diffraction maximum is related to the strength of those diffractions in the specimen. A spectrum

of the reflections of the family of planes parallel to the sample surface is obtained. The analysis of this spectrum permits the identification of the crystalline species (available in the ASTM database) of the sample. A more precise analysis of the diffraction profile permits the measurement of structural parameters.

In the case of films with a preferential orientation, the relationship between the intensity of the peaks of a diffraction diagram is very different from that of the ASTM database, which correspond to powder samples, and therefore, with random orientation.

Routine diffraction patterns were registered by a Rigaku *Rotaflex* Ru-200B with rotating anode ($\lambda = 1.5418$ Å (Cu Kα)). The working conditions were typically: 2θ scanning between 5° and 125°, with a 0.02° step and a scanning speed of 4°/min. In some cases, a Siemens D-500 ($\lambda = 1.5418$ Å (Cu Kα)) was also used, with the same working conditions. Both diffractometers are located in the Materials Science Institute of Barcelona (ICMAB-CSIC).

Measurements as a function of temperature were performed in a Siemens D-500 powder diffractometer with theta/2theta Bragg-Brentano geometry and with a temperature chamber which can reach up to 800 °C in a controlled atmosphere. This diffractometer is located in the University of Barcelona Technical Services (SCT-UB).

3.3.2 Texture Analysis by X-Ray Diffraction

We studied the preferential orientations of the textured thin films by rocking curves and ϕ-scan measurements with a Philips MRD diffractometer with a texture goniometer located at the University of Barcelona Technical Services (SCT-UB). Rocking curve measurements were made by doing an ω (angle of incidence) scan at a fixed 2θ angle (diffraction angle). The width of the curves is caused by the distribution of domain orientations in the sample and is therefore used as a measure of the quality of the film. ϕ-scans were done by measuring an hkl reflection, sweeping the ϕ angle (in- plane rotation around the center of the sample) and maintaining 2θ constant, $\omega = \theta$ and ψ (rotation around the axis formed by the intersection between the sample and diffraction planes) $\neq 0$ fixed. As a result, the symmetry and the texture in the plane of the sample are obtained.

The accurate determination of the lattice parameters was done performing the area scan of an out-of-plane reflection of the layers using a Bruker D8 DISCOVER diffractometer with a 4-angle goniometer and GADDS detector. With this type of goniometer the angles ω, θ, χ or ψ, and ϕ can be independetly controlled (Figure 3.7). The GADDS is an area detector which allows the simultaneous data collection of a large 2θ and χ range without sample or detector movement.

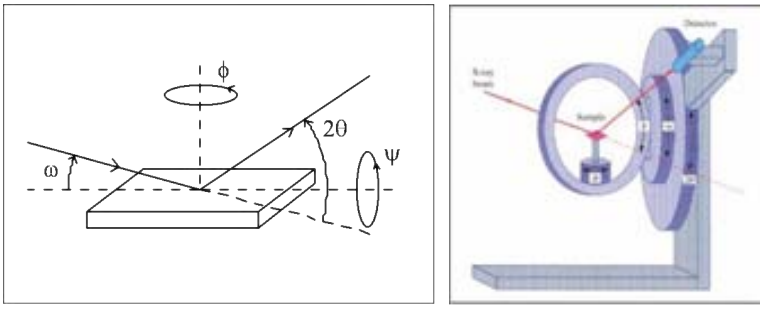

Figure 3.7: Illustration of the four-circle diffractometer geometry and relevant angles.

This diffractometer is located in the Materials Science Institute of Barcelona (ICMAB-CSIC).

3.3.3 Thickness Measurement by Reflectometry

X-ray reflectometry (XRR) is performed by measuring the intensity of the X rays reflected by a sample, at grazing angles, when the condition $\omega = 2\theta/2$ is satisfied. Working in θ-2θ mode we assure that the incidence angle is half of the diffraction angle. The surface and interphase reflections are due to different electronic densities in the different layers, which correspond to different reflection indexes in classical optics. For incidence angles θ below the critical angle, θ_c, the X-rays penetrate only a few nanometers into the sample and a total external reflection is produced. For most materials the critical angle is lower than 0.3°. Above θ_c the penetration depth increases rapidly. At every interface where the electron density changes, a part of the X-ray beam is reflected. Due to the interference between the X-ray beams scattered from the different interfaces one is able to record a scan consisting of so-called thickness fringes, i.e., intensity maxima corresponding to constructive interference

and minima due to destructive interference. The period of the interference fringes and the fall in the intensity are related to the thickness and the roughness of the layer (layers in case of multilayers), respectively. The reflection can be analyzed using Fresnel's classical theory. The interference maximum of order m, for a path difference $\Delta = m\lambda$, is found for:

$$m\lambda = \Delta \approx 2d\sqrt{\theta_m^2 - \theta_c^2} \Leftrightarrow \theta_m^2 \approx m^2 \frac{\lambda^2}{4d^2} + \theta_c^2 \tag{3.2}$$

from where the thickness can be directly calculated as:

$$d^2 = \frac{\lambda^2 m^2}{4(\theta_m^2 - \theta_c^2)} \tag{3.3}$$

The typical range for measurements are between 0 and 5° in θ.

The diffractometer used for the reflectometry measurements is the same Rigaku used for the θ-2θ measurements, and which is located in the Materials Science Institute of Barcelona (ICMAB-CSIC).

3.3.4 High Resolution Electron Microscopy (HREM)

The microstructure of the layers was studied by transmission electron microscopy (TEM). TEMs work by using a tungsten or now, more usually, LaB_6 filament to produce an electron beam in a vacuum chamber. The emitted electrons are accelerated through an electromagnetic field that also narrowly focuses the beam. The beam is then passed through the sample material. The specially prepared sample is a very thin (less than 100 nm) slice of material. The electrons pass through the sample and the diffraction pattern and image are formed at the back focus plane and image plane of the objective lens. If we take the back focus plane as the objective plane of the intermediate lens and projector lens, we will obtain the diffraction pattern on the screen. It is said that the TEM works in diffraction mode. If we take the image plane of the objective lens as the objective plane of the intermediate lens and projector lens, we will form image on the screen. It is the image mode.

It is possible to simultaneously study the microstructure of the illuminated zone from the diffraction pattern, orient it and select certain spots by different aperture diaphragms, which will induce different types of image contrast. TEMs can produce

images with resolution down to 0.2 nm. This resolution is smaller than the size of most atoms (not O^{2-} nor some cations) and therefore images can be produced using TEM that show the true structural arrangement of atoms in the sample material in some cases.

Electron diffraction (ED) and high-resolution electron microscopy (HREM) studies were performed using a JEOL 4000EX microscope located in the Electron Microscopy for Materials Science (EMAT) in Antwerp.

3.4 Transport Properties and Oxygen Exchange Characterization

3.4.1 Electrical Conductivity Measurements

For the conductivity measurements two parallel Ag contacts were painted on the surface of the samples (Figure 3.8). The planar resistance of the films was measured by using an HP4192A impedance analyzer by AC at a fixed low frequency of 1 kHz, provided the substrate resistance is much higher than that of the film, so the current can be considered to be flowing entirely through the film. At this frequency it was proved that there is no capacitive contribution to the total impedance. The laboratory equipment is shown in Figure 3.9. AC frequency was used instead of DC in order to avoid possible problems of charge polarization and accumulation in the electrodes, which could affect the measurement. The contact resistance was checked by a four point measurement and it was estimated to be low enough not to be taken into account. The sample is located inside a tubular furnace, which temperature can be varied from room temperature to 1000 °C and in which different gases can be introduced. Electrical properties have been measured under oxygen and nitrogen flow and under mixtures of these two gases (specially to obtain a gas mixture with a concentration similar to air). The oxygen partial pressure in the nitrogen flow is estimated to be about 50 ppm.

Considering that the current is flowing homogenously across the thickness of the film, which is a valid approximation given the large ratio between the distance between parallel contacts and the thickness of the films (L $\approx$ 3 mm, for a film of 100

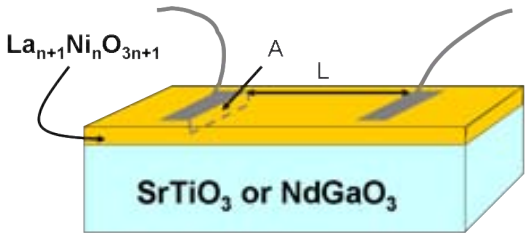

Figure 3.8: Scheme of the conductivity measurements of a $LaNiO_3$ film on a STO/NGO substrate. The thickness of the thin film is grossly exaggerated when compared to the thickness of the substrate.

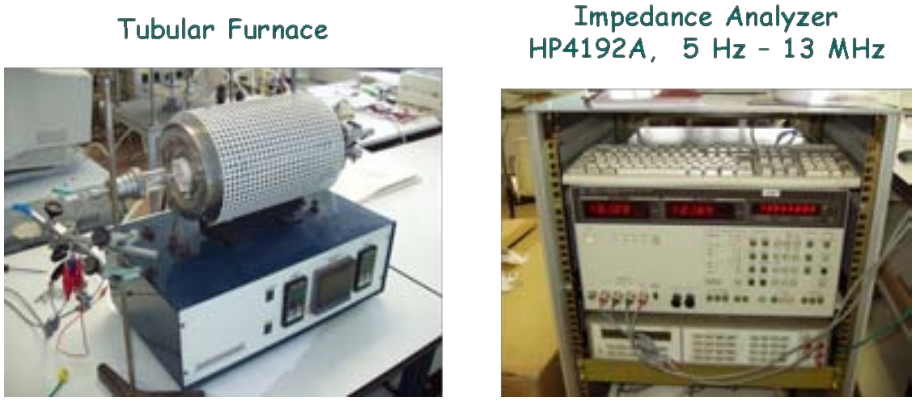

Figure 3.9: Conductivity measurements equipment.

nm thickness: t = 100 nm ⇒ L/t = 3 x 10^4), the measured electrical resistance can be simply expressed as:

$$R = \rho \frac{L}{A} \tag{3.4}$$

in which ρ is the resistivity of the material, L is the distance between the two electrodes and A the cross sectional area, i.e., the length of the electrode multiplied by the thickness of the films. Thereby, the resistivity (ρ) can ve readily calculated from the measured resistance at each temperature and oxygen pressure, and the conductivity (σ) can be calculated using Eq. 3.5:

$$\sigma = \frac{1}{\rho} \tag{3.5}$$

at each temperature and oxygen pressure.

3.4.2 Electrical Conductivity Relaxation Measurements

In Electrical Conductivity Relaxation (ECR) experiments, the sample is first held at equilibrium at an initial oxygen partial pressure. At constant temperature, the gas atmosphere is then switched abruptly to a different oxygen pressure. The change in the conductivity of the sample, which reflects the change in the oxygen content, is recorded until the new equilibrium is established. By analyzing the normalized conductivity as a function of time (g(t)),

$$g(t) = \left(\frac{\sigma(t) - \sigma_0}{\sigma_\infty - \sigma_0}\right) \tag{3.6}$$

where σ_0, σ_∞ and $\sigma(t)$ are the initial, final and time = t conductivity values, respectively, and solving Fick's law for the given initial and boundary conditions, the chemical diffusion coefficient, D_{Chem}, and the chemical surface exchange coefficient, k_{Ex}, can be obtained. Figure 3.10 shows a schematic of the $La_2NiO_{4+\delta}$ thin film on a STO/NGO substrate with the two silver contacts.

Since the measured $La_2NiO_{4+\delta}$ films are very thin (<350 nm), it is reasonable to assume that the oxygen transport is controlled by the surface exchange rate. For a single surface reaction and a small oxygen pressure change, the normalized conductivity of a plane sheet is

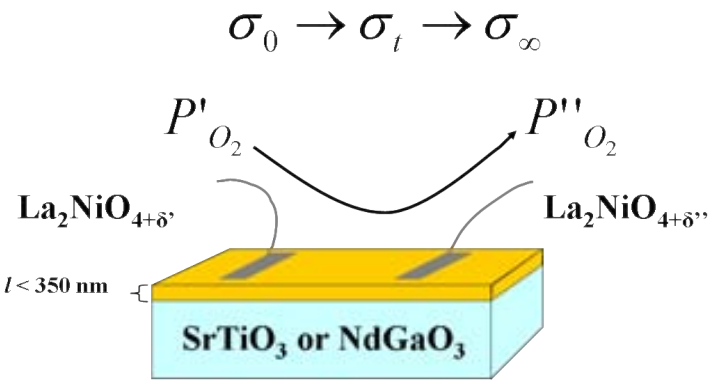

Figure 3.10: Schematic of the ECR measurements of a $La_2NiO_{4+\delta}$ film on a STO/NGO substrate. The thickness of the thin film is grossly exaggerated when compared to the thickness of the substrate.

$$g(t) = 1 - exp(-\frac{t}{\tau}) \tag{3.7}$$

with

$$\tau = \frac{l}{k_{Ex}} \tag{3.8}$$

where τ is the time constant and l is the thickness of the film.

The oxygen pressure was measured by two "RAPIDOX 2000" oxygen sensors, self-contained process analyzers using zirconia sensor technology, situated before and after the furnace. The oxygen pressure changes were performed by simultaneously switching from a O_2/N_2 gas mixture with a P'_{O_2} oxygen partial pressure to a gas mixture with a different oxygen partial pressure P''_{O_2}. A scheme of the experimental setup is shown in Figure 3.11.

3.4.3 Isotope Exchange Depth Profile Method (IEDP)

The tracer oxygen diffusion coefficient D^* and the tracer surface exchange coefficient k^* were determined by the isotopic exchange depth profile (IEDP) technique using the secondary ion mass spectrometry (SIMS) after isotopic exchange of ^{18}O for ^{16}O in the $La_2NiO_{4+\delta}$ samples.

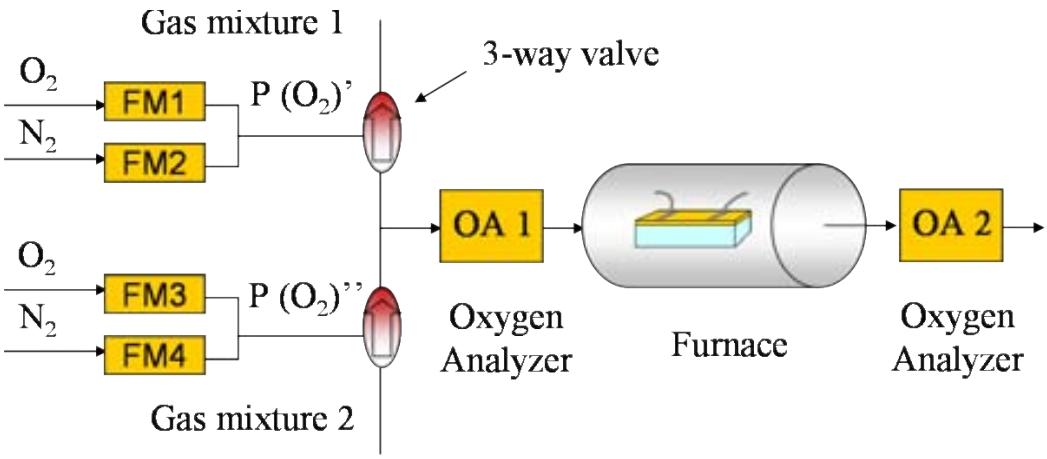

Figure 3.11: Electrical conductivity relaxation measurement equipment.

Prior to the isotopic exchanges, as deposited samples were situated in a silica tube, which was heated by a "roll-on" furnace (see Figure 3.12). The apparatus was evacuated to $< 2 \times 10^{-7}$ mbar by means of a rotary pump plus a turbomolecular pump. The samples were then subjected to anneals in pure oxygen (research grade 99.9995%) of natural isotopic abundance (^{18}O molar fraction of 0.002) for a period of time approximately one order of magnitude greater than the oxygen-18 tracer anneal time at the same temperature as the exchange which will take place after. The samples were then cooled down to room temperature, the ^{16}O removed, an ^{18}O enriched gas (24.9 or 68.5%) introduced, and then heated up to different temperatures. The heating and quenching of the samples could be achieved either by means of predefined temperature ramps, with the help of a fan for the cooling, or by rapidly heating the sample by rolling the preheated furnace over the sample holder. A constant temperature was maintained for the required duration of the anneal (30 or 60 min), and finally the sample was quenched by rolling the furnace off the sample holder. Once the sample had cooled, the labelled oxygen was cryogenically recovered using molecular sieve sorption pumps. Before and after the exchange anneals the isotopic composition of the labelled oxygen was measured by introducing a small quantity of the gas into a quadrupole residual gas analyzer via a controlled leak valve, which proved that there was no change in the ^{18}O concentration. The heating

and cooling temperatures vs. time were recorded and taken into account to obtain the corrected effective exchange time.

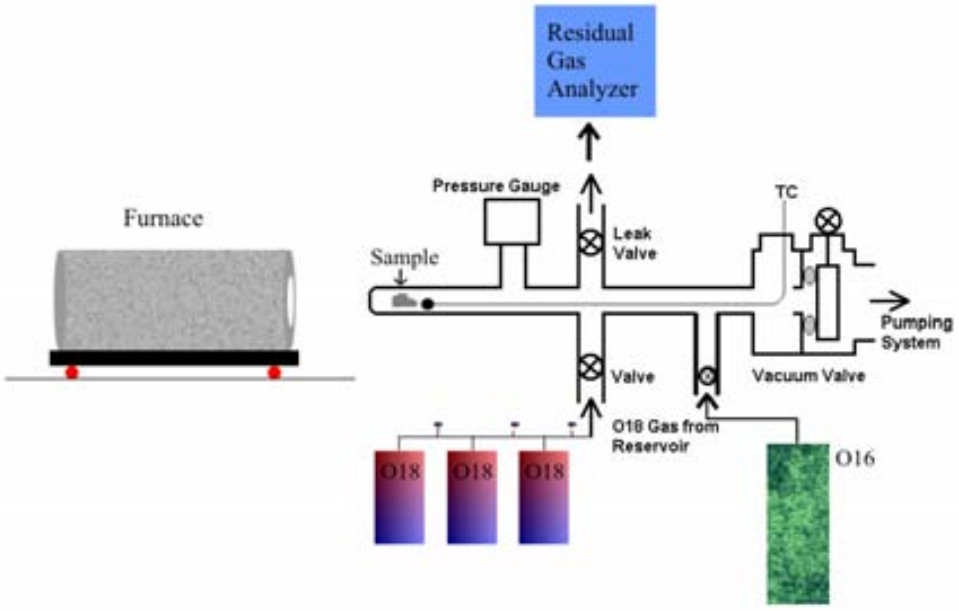

Figure 3.12: ^{18}O exchange rig.

The ^{18}O and ^{16}O concentration depth profiles in the films were measured by Secondary Ion Mass Spectrometry (SIMS) using an Atomika 6500 quadrupole-based analyzer and sputtering with a nitrogen primary ion beam (N_2^+) at 1.25 keV. Alternatively, a FEI FIB200 TEM instrument coupled to a SIMS detector was used. In this case, the FIB milling uses a focused Ga^+ beam of 30 keV with an ultimate lateral resolution of about 5 nm. Subsequently the depth of the etched craters was measured by profilometry using an optical microscope based interferometer (ZYGO Corp. NewView 200).

To measure the diffusion along the traverse direction (c-axis direction), areas of about 350 x 350 μm were analyzed as a function of depth. To ensure that only the oxygen transport in the transverse direction along the film thickness was in-

vestigated, the analyzed areas were selected far from the sample edge, avoiding the influence of any planar diffusion coming from there. The concentration profiles were collected for different exposure times, and exchange temperatures. In order to evaluate a possible influence of films strain due to different lattice mismatch, films grown onto different substrates (STO and NGO) were analyzed. The sudden variation of the ^{18}O + ^{16}O signal in the SIMS profiles when eroding down to the substrate for the different film thicknesses served as a calibration of the milling rate. The oxygen concentration profiles were analyzed using the analytical solutions to the diffusion equation for a plane sheet model developed by Crank [105] and fitting by least squares numerical fit. In our case, the $La_2NiO_{4+\delta}$ film thickness is taken to be half the plane sheet thickness. This analysis takes into account the time that the sample has been exposed to the gas phase during heating and cooling steps [106]. A set of D_c^* and k_c^* values corresponding to oxygen transport along the *c*-axis direction were extracted at each exchange anneal temperature.

To determine the oxygen transport along the *a*-*b* plane in the epitaxial films with *c*-axis orientation, that is along the longitudinal direction in the plane of the film, a dense and uniform Au thin film of approx. 80 nm thickness was sputtered to protect the $La_2NiO_{4+\delta}$ film surface and prevent oxygen exchange from the substrate surface. A trench was then defined in the surface of the Au films penetrating down to the substrate. The lateral edge of the film was opened to allow the exchange with the oxygen-18 enriched exchange gas phase and thus ensuring the diffusion of the ^{18}O species only along the *a*-*b* planes of the $La_2NiO_{4+\delta}$ film. After exposure, the oxygen concentration depth profiles were determined from the top part of the film (after removing all the Au layer sputtered on that region) by using the line scan mode in the Atomika SIMS system. The longitudinal concentration profiles were analyzed using a semi-infinite plane solution of the diffusion equation published by Crank [105]. For this film orientation the analysis provided D_{ab}^* and k_{ab}^* coefficients for the oxygen exchange and transport along the *a*-*b* planes of the structure. A more detailed analysis of the procedure and the results obtained are described in Section 5.2.

Chapter 4

Preparation and Characterization of $La_2NiO_{4+\delta}$ Thin Films

4.1 Deposition of $La_2NiO_{4+\delta}$ Thin Films

4.1.1 Substrate Requirements

Two different types of single crystal substrates with perovskite structure have been used to epitaxially grow the films: $SrTiO_3$ (100) (noted STO) and $NdGaO_3$ (110) (noted NGO). STO presents a cubic structure with a cell parameter of 3.905 Å and NGO is orthorhombic with pseudo-cubic in-plane parameters of 3.863 and 3.854 Å. These substrates and orientations were chosen in order to promote *c*-axis oriented epitaxial growth of the layers, due to the low mismatch with the basal perovskite plane of the $La_2NiO_{4+\delta}$ structure. If we consider the $La_2NiO_{4.18}$ structure reported by Metha and Heaney (ICSD Collection Code 44121) [107]: orthorhombic with a = 5.4652, b = 5.4687, c = 12.678 Å cell parameters, it has a basal a-b plane parameter a_p = 3.866 Å, which corresponds to a mean mismatch of +1% (tensile) on STO substrates, and about -0.19% (compressive) on NGO (110) substrates (see Figure 4.1).

In Figure 4.2 the structure scheme of *c*-axis oriented grown $La_2NiO_{4+\delta}$ shows

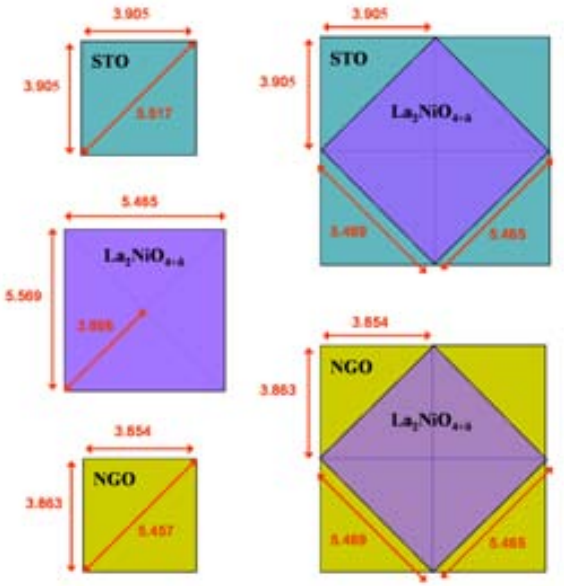

Figure 4.1: Base plane match of *c*-axis oriented $La_2NiO_{4+\delta}$ on STO and NGO substrates.

the parallel arrangement of the perovskite blocks of the $La_2NiO_{4+\delta}$ structure onto those of the substrates (STO and NGO).

4.1.2 Optimization of the Experimental Parameters

As already described in Section 2.4, the general experimental conditions were established by former studies performed with this equipment. For the selection of the initial working experimental parameters to prepare high quality $La_2NiO_{4+\delta}$ thin films we took into account the optimized parameters by Faucheux et al. [90, 91]. Thus, the initial working conditions were: evaporation temperature of 280 °C (selected from the TGA analysis), reactor temperature of 600 °C, reactor pressure of 10 Torr, total gas flow of 1 l/h (1:1 ratio of O_2:Ar), valve opening time of 2 ms, injection frequency of 1 Hz, total concentration solution of 0.02 M and a La/Ni ratio in the precursor solution equal to 2.33. Under these experimental conditions the 012 reflections of the $LaNiO_3$ phase appeared in the XRD patterns, instead of those of the expected $La_2NiO_{4+\delta}$ phase, indicating a deviation in the La/Ni film compo-

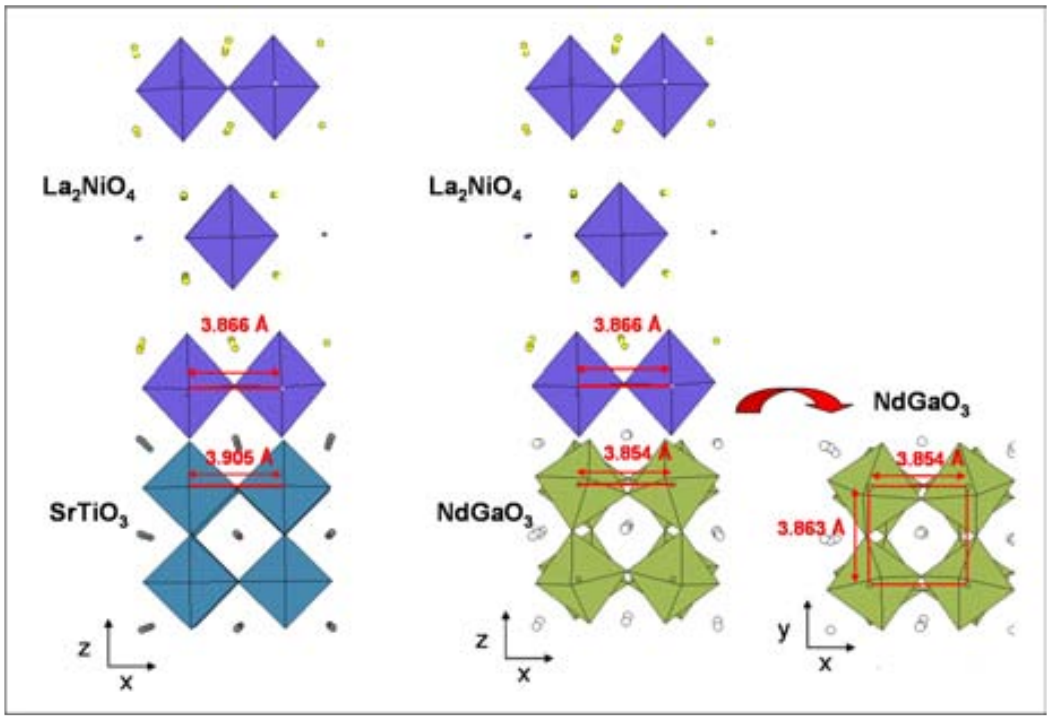

Figure 4.2: Structures scheme of *c*-axis oriented $La_2NiO_{4+\delta}$ on STO and on NGO.

sition. Therefore, the La/Ni ratio in the solution was increased up to 3.67, where the $La_2NiO_{4+\delta}$ reflections were obtained in the diffraction patterns of the deposited films.

The deviation in the composition transfer between vapor and condensed phase is typical for the MOCVD processes and occurs because each precursor has a different decomposition and deposition yield. The deposited lanthanum nickelates were nickel-rich compared with the injected precursor solution, which has previously been observed by Lane et al. in $LaNiO_3$ layers [108] and by Faucheux et al. in $La_2NiO_{4+\delta}$ layers [90].

Under the described experimental conditions and with a La/Ni ratio of 3.67 in the precursor solution, films at different temperatures from 700 to 850 °C were deposited. The obtained X-ray diffraction patters of the films grown on STO substrates are shown in Figure 4.3.a and those grown on NGO substrates in Figure 4.3.b. Films deposited on both substrates at 700 °C showed the 00l reflections of $La_2NiO_{4+\delta}$ structure, but with broader and less intense peaks in comparison with higher temperatures. The crystallinity of the films improves at 750 °C, showing narrow 00l reflections with a small peak corresponding to the La_2O_3 phase. If the deposition temperature is increased, along with the 00l reflection, more reflections corresponding to La_2O_3 appear, while the crystallinity of the $La_2NiO_{4+\delta}$ phase decreases. As shown in the SEM pictures (Figure 4.4), samples deposited on STO at 750 and 800 °C were rather flat. On the contrary samples deposited at 700 °C showed small crystallites at the surface, and samples deposited at 850 °C were totally detached from the substrate. Samples deposited on NGO had a quite similar surface morphology for each deposition temperature.

Composition analysis by WDS of films deposited at 750 °C showed a La/Ni concentration ratio close to 2.52, which is higher than the desired value around 2 and which is associated to the presence of La_2O_2 in the layers. We used mainly the analysis of La/Ni composition on STO, as it provides a better accuracy than on NGO, due to an overlapping between some lines of film and NGO substrate in the WDS spectra. In order to optimize the solution concentration at this temperature we prepared samples varying the La/Ni ratio from 2.67 to 3.67. The XRD patterns corresponding to this series can be seen in Figure 4.5.

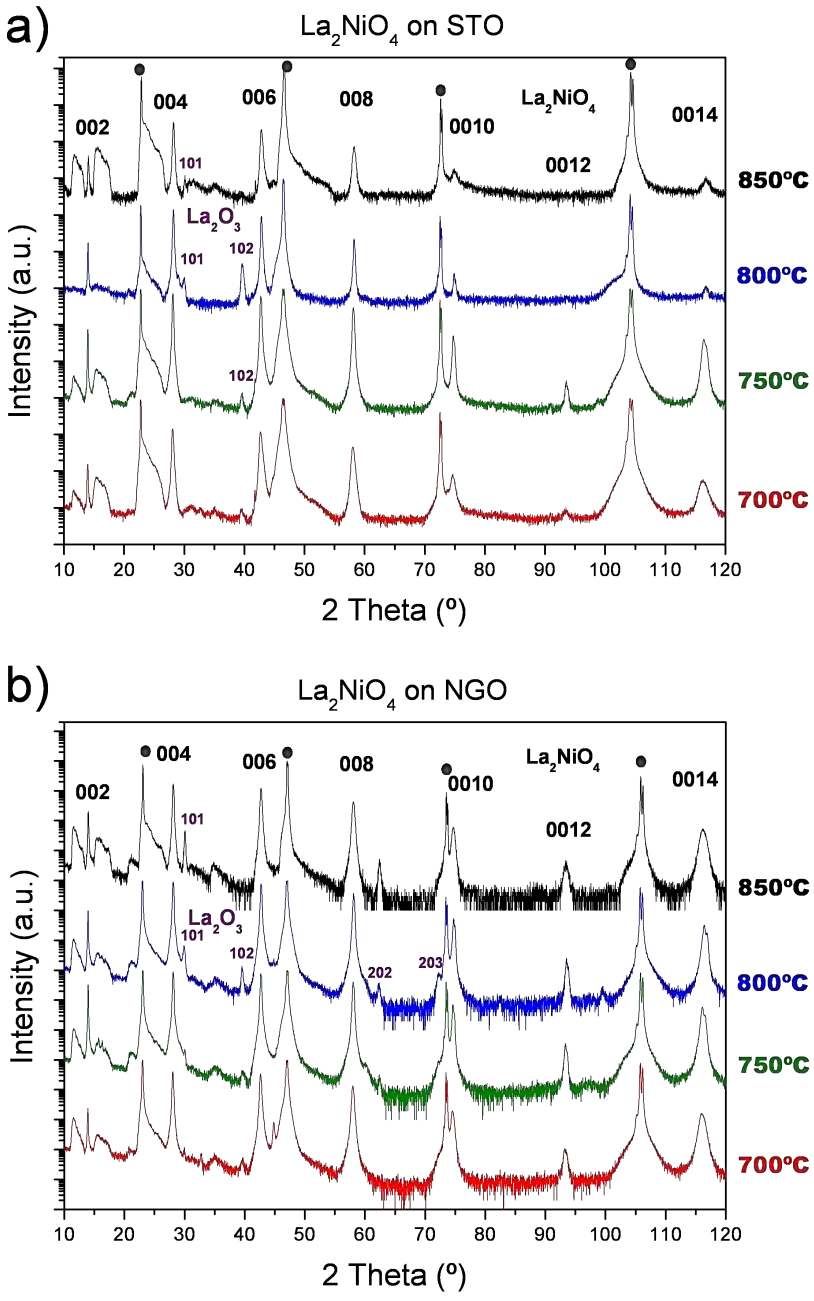

Figure 4.3: XRD patterns of films deposited on STO (a) and on NGO (b) at different temperatures. The positions for substrate peaks (circles), for the 00l peaks corresponding to c-axis oriented $La_2NiO_{4+\delta}$ (black) and for the peaks corresponding to the La_2O_3 phase are indicated. The broad peaks at low angles are an instrumental contribution of the diffractometer used.

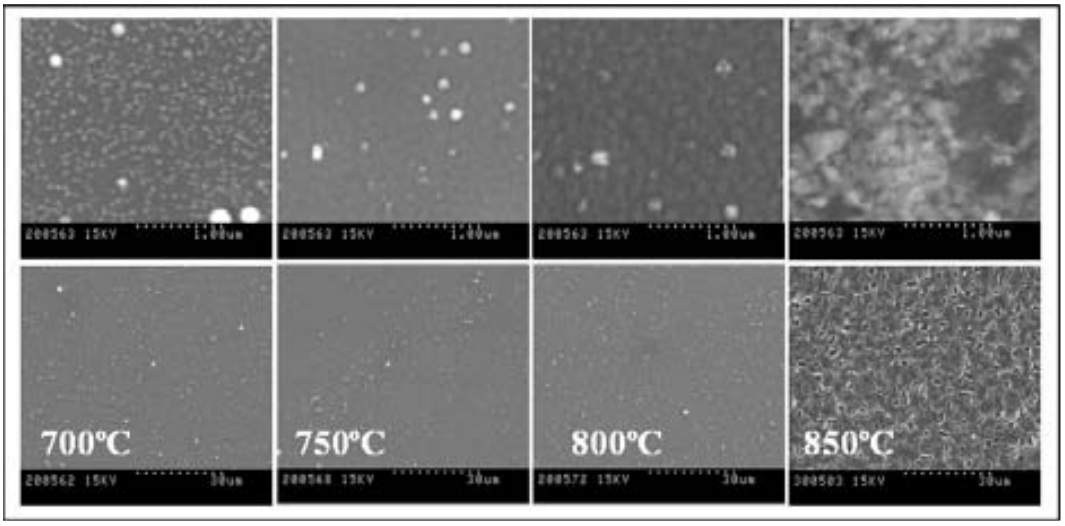

Figure 4.4: SEM surface images of $La_2NiO_{4+\delta}$ films grown on STO at different temperatures. Magnification of top row: 30000 x; of bottom row 1000 x.

By decreasing the precursor concentration ratio La/Ni from 3.67 to 3, the La_2O_3 phase peaks disappeared, and thus only intense and narrow $La_2NiO_{4+\delta}$ 00l reflections were observed, showing the high purity, crystallinity and orientation of the films. For La/Ni precursor ratios lower than 3, the 00l reflection positions were displaced towards the position of the $La_3Ni_2O_7$ phase reflections and new peaks associated to this phase appeared. A slight broadening of the diffraction peaks along with a low relative intensity of the weaker peaks were also observed.

WDS measurements in these samples gave the La/Ni ratio values which are detailed in Table 4.1.

Table 4.1: La/Ni concentration ratio in the $La_2NiO_{4+\delta}$ deposited films for different La/Ni ratios in the precursor solution

La/Ni ratio solution	**La/Ni ratio film**
2.67	1.73
3.00	2.17
3.67	2.52

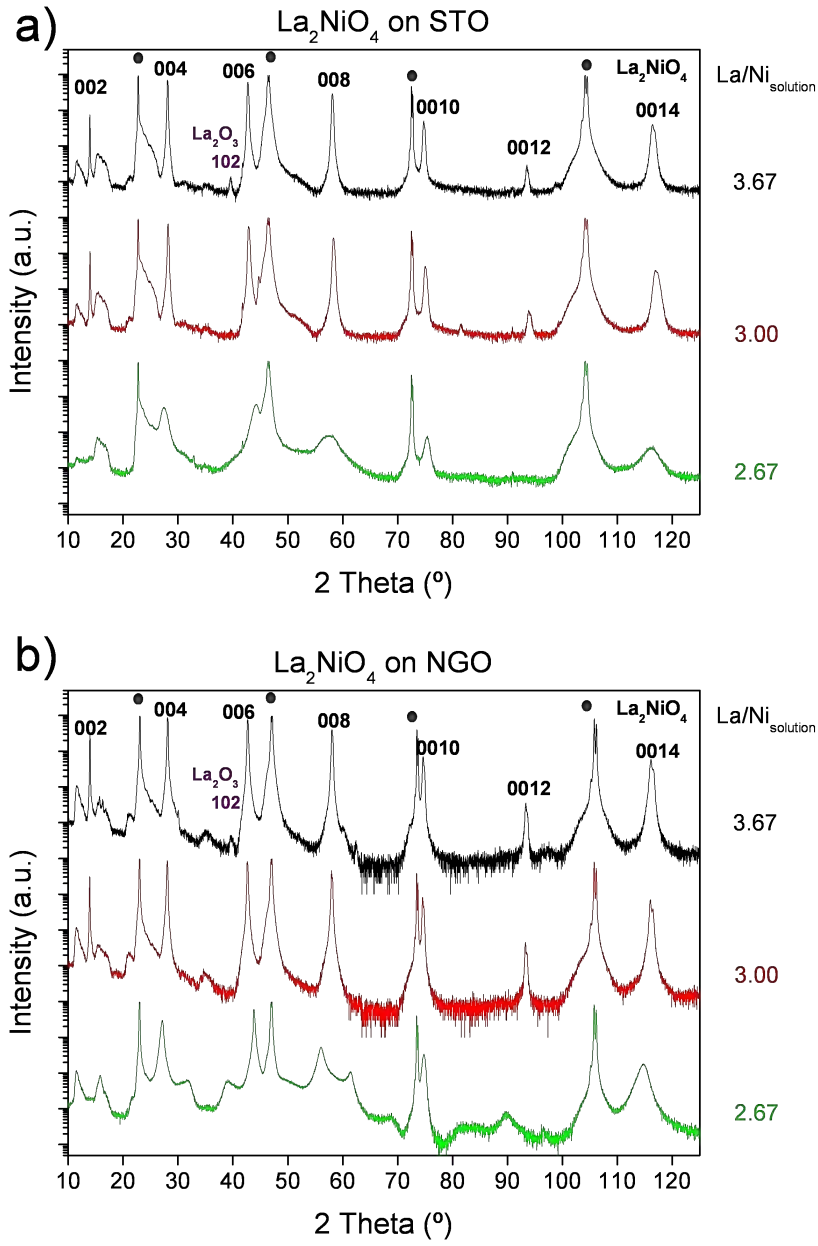

Figure 4.5: XRD patterns of films deposited on STO (a) and on NGO (b) at different precursor concentration ratios. The positions for substrate peaks (circles), for the 00l peaks corresponding to c-axis oriented $La_2NiO_{4+\delta}$ (black) and for the peaks corresponding to the La_2O_3 phase are indicated.

In view of the XRD patterns, by using La/Ni solution values close to 3 the growth of films with a composition very close to the expected La/Ni = 2 is obtained for films deposited at 750 °C.

The optimum conditions to prepare high quality epitaxial $La_2NiO_{4+\delta}$ films were thus defined as:

- Evaporation temperature: 280 °C
- Deposition temperature: 750 °C
- Injector aperture time: 2 ms
- Pulse frequency: 1 Hz
- Molar ratio of La/Ni in the precursor solution: 3.00
- Total concentration of the solution: 0.02 M
- Total gas flow of 1 l/h
- Ratio of oxygen to argon: 1:1

4.2 Structural and Morphological Characterization of $La_2NiO_{4+\delta}$ Thin Films

The XRD patterns of the epitaxial *c*-oriented $La_2NiO_{4+\delta}$ films on STO and NGO substrates grown under the selected optimal conditions are shown in Figure 4.6.

In order to determine the growth rate of our layers under these optimized conditions, we prepared samples with different thickness by varying the number of droplets injected from 250 to 2000. The film thickness was determined by XRR for the thinner films (from 25 to 60 nm) and estimated by microprobe measurements for the thicker layers ($\geq$ 100 nm). Figure 4.7 shows the XRR pattern of a layer prepared by injecting 400 pulses and with an estimated thickness of 33.85 nm. The growth rate at such experimental conditions was approximately 305 nm/h with 85 Å of film grown per pulse. Typical estimated and measured thicknesses are shown in Table

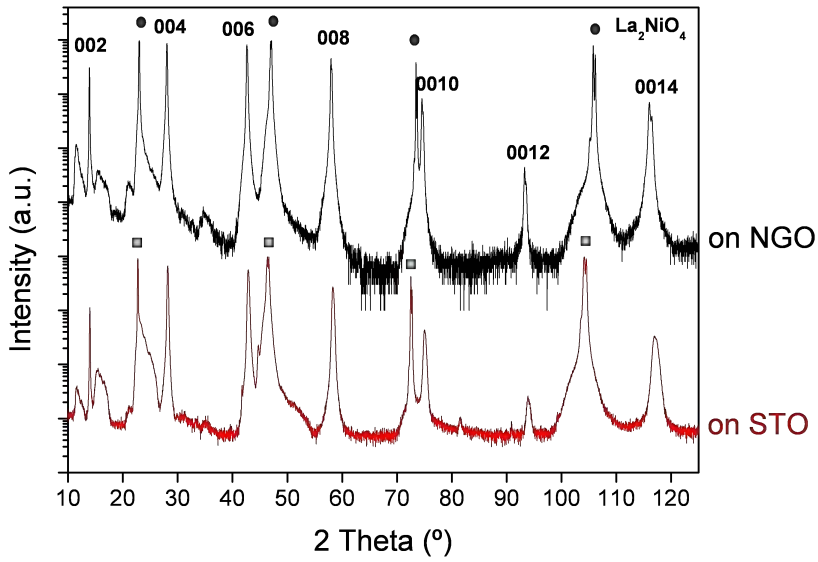

Figure 4.6: XRD patterns of films deposited on STO and on NGO under the selected optimal conditions. The positions for substrate peaks: STO (squares) and NGO (circles) and for the 00l peaks corresponding to *c*-axis oriented $La_2NiO_{4+\delta}$ are indicated.

4.2 for a series of experiment with a different number of droplets injected. The thickness values estimated by WDS were consistent with this growth rate. The surface of our thin layers was too flat and details could not be observed with enough quality using the scanning electron microscope. Thus, the surface morphology of the layers was studied using the AFM technique. For films deposited on both substrates, the roughness value increases from RMS (root mean square) = 3-6 nm (for 28 nm thick films) up to RMS = 35-55 nm (for 300-350 nm thick films) (see Figure 4.8).

Table 4.2: Film thickness vs number of droplets injected

Droplets	**Thickness**
	XRR
200	13.5 nm
400	33.9 nm
600	52.9 nm
	WDS
1000	69.5 nm
1500	118.4 nm
3000	356.3 nm

The quality and the epitaxial relationship between the substrate and the layers were studied by XRD. The narrow rocking curve (FWHM = 0.2°) of the 008 reflection confirms the high degree of *c*-axis orientation of the films (Figure 4.9). This curve corresponds to a 200 nm film grown on NGO. The quality of the film orientation decreases with film thickness (FWHM = 0.63° for 300 nm-thick films grown on NGO) and when the substrate is changed (FWHM = 0.78° for 325 nm-thick films grown on STO) due to a larger mismatch between the film and the substrate.

The fourfold symmetry in the phi-scan of the 208 $La_2NiO_{4+\delta}$ reflection (Figure 4.10) and its relation with the 204 reflection of the NGO substrate confirms the in-plane alignment of the film, which corresponds to the expected parallel arrangement of the perovskite blocks of the $La_2NiO_{4+\delta}$ structure onto those of the substrate.

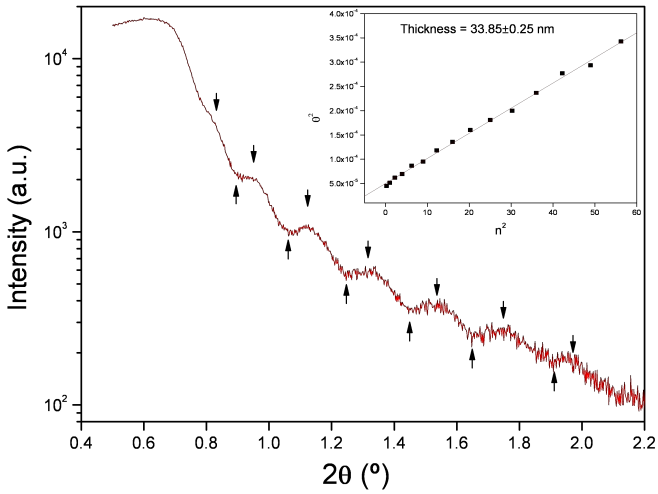

Figure 4.7: Reflectometry of a $La_2NiO_{4+\delta}$ film grown on STO.

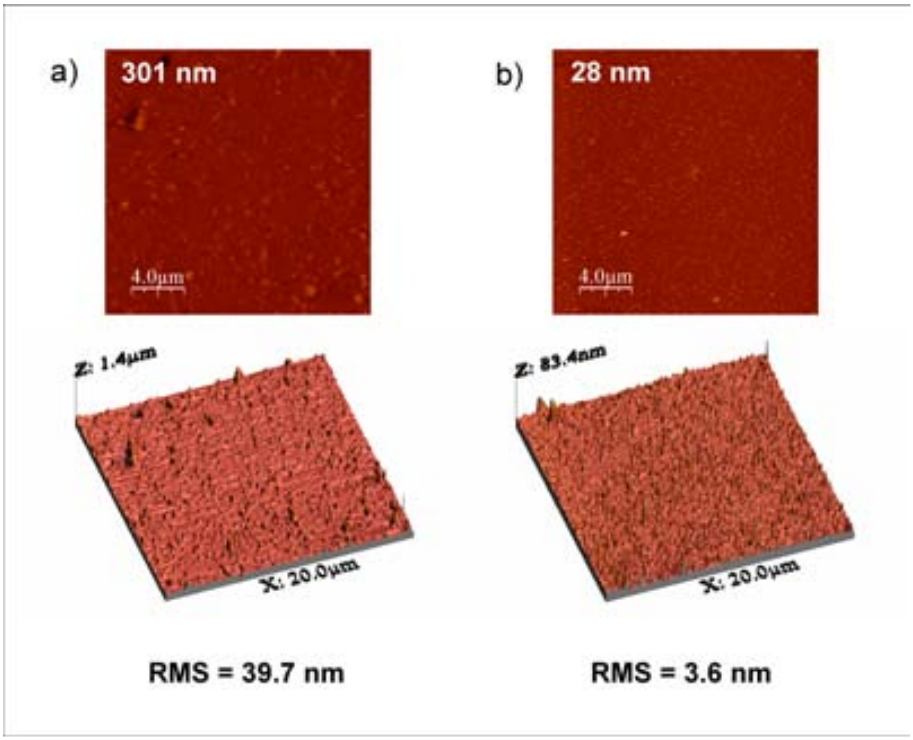

Figure 4.8: AFM image of a thick and a thin film deposited on STO.

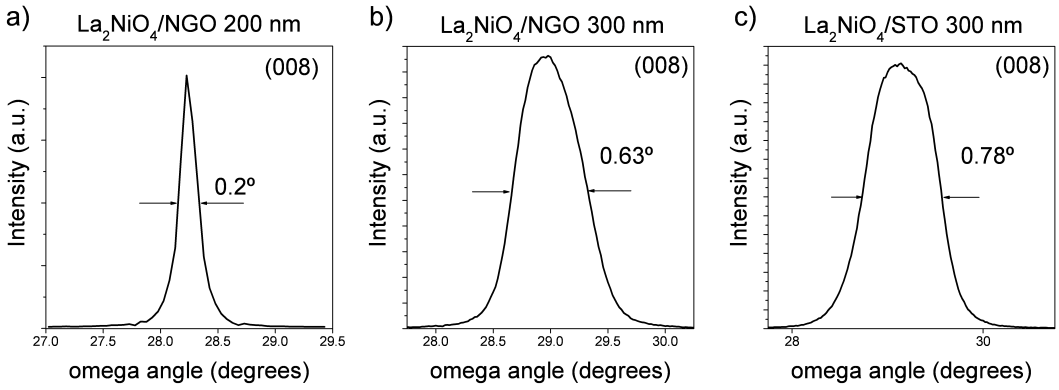

Figure 4.9: X-Ray rocking curve of the 008 reflection of an a) 200 nm thick $La_2NiO_{4+\delta}$ layer grown on NGO; 300 nm thick $La_2NiO_{4+\delta}$ layer grown on NGO; 300 nm thick $La_2NiO_{4+\delta}$ layer grown on STO.

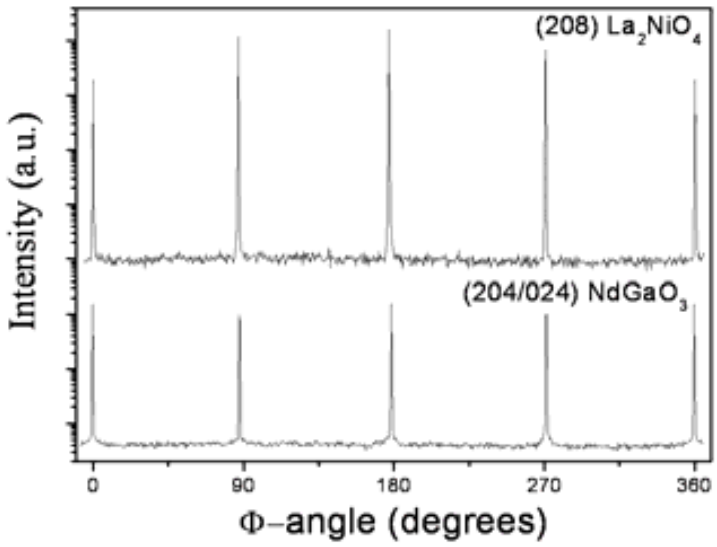

Figure 4.10: Phi-scan of the (208) reflection of a 200 nm-thick $La_2NiO_{4+\delta}$ layer grown on NGO.

4.3 Microstructural Characterization of $La_2NiO_{4+\delta}$ Thin Films

Details of the microstructure of the layers were observed using TEM/HREM microscopy. The high quality and epitaxy of the $La_2NiO_{4+\delta}$ thin films deposited on STO and NGO were confirmed by the cross-section images of the film/substrate interfaces along with the corresponding ED patterns, as can be seen in Figure 4.11.

The ED patterns are formed by a superposition of the patterns from substrate and film. The more intense reflections, which form a square pattern, are due to the substrate, whereas the weaker reflections are due to the film. The reflections in all observed reciprocal space sections can be indexed in a tetragonal unit cell with cell parameters equal to those determined from the XRD data, and confirmed the epitaxial arrangement of both film and substrate structures observed by XRD data. In real space, the visible periodic layers along the c-axis correspond to the $La_2NiO_{4+\delta}$ layer sequence - NiO_2 - LaO - LaO - NiO_2 -. According to the computer simulated images (inset in Figure 4.11.a), the bright dots at this particular thickness and defocus value correspond to columns of heavy atoms.

In the case of film deposited onto STO, a perovskite-type buffer layer a few unit cells thick is formed at the film-substrate interface, as depicted in Figure 4.11.a. The position of both interfaces, substrate/buffer and buffer/film, are indicated by white and black arrowheads, respectively. Considering that the STO substrate has a perovskite structure and $La_2NiO_{4+\delta}$ is perovskite-related, it is safe to conceive that the perovskite stacking will remain continuous across the interface and a $LaNiO_3$ perovskite buffer layer is therefore formed between the substrate and the film. The image simulation (inset in Figure 4.11.a.) including a 3 unit cells thick $LaNiO_3$ buffer layer shows a good fit with the experimental image. As can be seen in Figure 4.11.b., films deposited on NGO did not show any buffer layer. In that case, the steps in the substrate surface due to the miscut angle produce anti-phase boundaries (APB) clearly seen in the image, indicated by a white arrowhead. The APB are periodic and their density is rather large, with a distance of 50 to 60 nm from one to the other, as it corresponds to the density of steps at the substrate surface, as we just mentioned. On the other hand, the APBs are very unfrequent in the films deposited

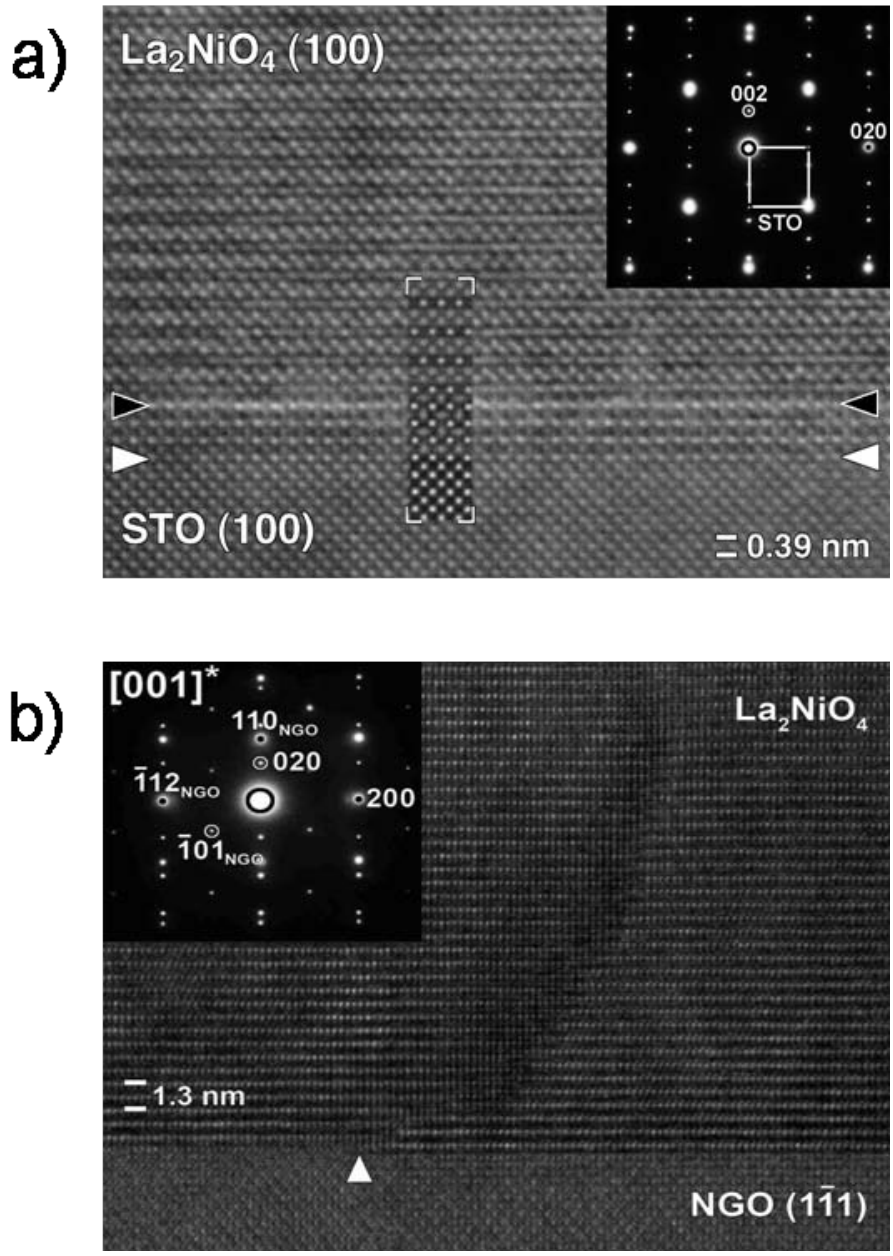

Figure 4.11: a) Cross-section HREM image of a *c*-axis oriented $La_2NiO_{4+\delta}$ film deposited on STO (001) and corresponding ED pattern, along the [100] direction. A calculated image of the substrate / buffer / film interface with a 3 unit cell thick buffer layer, for a focus value f = -70 nm and t = 5 nm is shown as an inset b) Cross-section HREM image of a *c*-axis oriented $La_2NiO_{4+\delta}$ film deposited on NGO (110) and corresponding ED pattern, along the [100] direction. Antiphase boundary generated by a surface step on the substrate is marked with an arrow.

onto STO, as they are mainly due to a change in the thickness of the $LaNiO_3$ buffer layer.

Lower magnification cross-section images of the same $La_2NiO_{4+\delta}$ film deposited on NGO are shown in Figure 4.12, in which the high quality of the film is observed to continue through the whole film thickness.

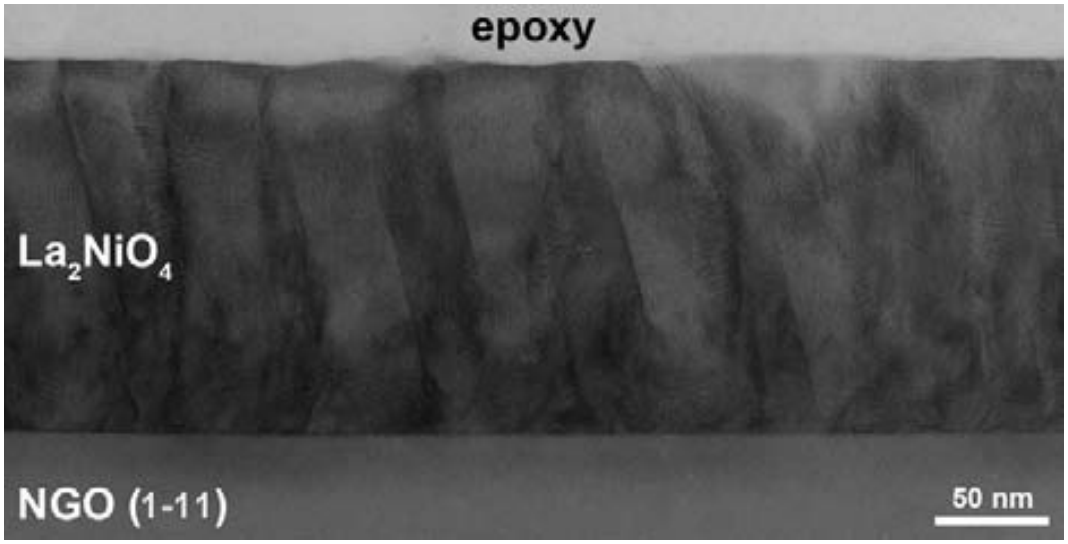

Figure 4.12: Cross-section HREM images of a c-axis oriented $La_2NiO_{4+\delta}$ film deposited on NGO (110).

4.4 Variation of the Cell Parameters and the Strain with Thickness

As has previously been mentioned, by varying the number of pulses during the deposition, $La_2NiO_{4+\delta}$ epitaxial films of different thickness were deposited on STO and NGO. The in-plane (a and b) and out-of-plane (c) parameters were determined by measuring the angular position of the $22\underline{10}$ reflection of the $La_2NiO_{4+\delta}$ films in the reciprocal space, using an X-Ray Diffractometer with a texture goniometer. This reflection was chosen because it has a large 2θ value, which increases the accuracy of the parameter determination. To take into account the possible systematic errors

in the measurements, the position of the 203 reflection of the STO was used as a reference. In the case of the NGO, as the cell is orthorhombic, we can distinguish two different in-plane cell parameters: a and b, for which we used as reference two different reflections, 334 and 150, respectively. The c parameter was also determined from the position of the 00$\underline{14}$ reflection in a standard theta-2theta configuration.

The Q_x and Q_y coordinates from a reciprocal space map are given by the equations:

$$Q_x = sin\theta sin(\theta - \omega) \tag{4.1}$$

$$Q_y = sin\theta cos(\theta - \omega) \tag{4.2}$$

- 2θ is the detector position at which the reflection from reciprocal lattice points hkl can be observed.

- ω is the angle made by the incident X-ray beam with the sample surface.

The in- and out-of-plane cell parameters, a and c, respectively, are calculated by the following equations:

$$a = \frac{\lambda * h}{2Q_x} = \frac{\lambda * h}{2sin\theta sin(\theta - \omega)} \tag{4.3}$$

$$c = \frac{\lambda * l}{2Q_y} = \frac{\lambda * l}{2sin\theta cos(\theta - \omega)} \tag{4.4}$$

where

- $\lambda = 1.5406$ nm is the Cu-K_α wavelength

- h and l = Miller reflexion indexes (h k l), equal to 2 and 10 in this case (2 2 10 reflection)

A typical reciprocal space map in Q_x, Q_y coordinates of the $La_2NiO_{4+\delta}$ 22$\underline{10}$ reflection, in this case for a 100 nm film deposited on NGO, can be seen in Figure 4.13. The 334 NGO substrate reflection clearly appears with two components: Kα_1 and Kα_2, while the $La_2NiO_{4+\delta}$ 22$\underline{10}$ peak is slightly asymmetrical, which could also

be due to the two Kα components of the X-rays. A reciprocal space map such as this was systemmatically performed to each $La_2NiO_{4+\delta}$ thin film, the position of both the film and the substrate peaks were fitted to a gaussian curve, and from the position of the center, the in- and out-of-plane cell parameters were extracted.

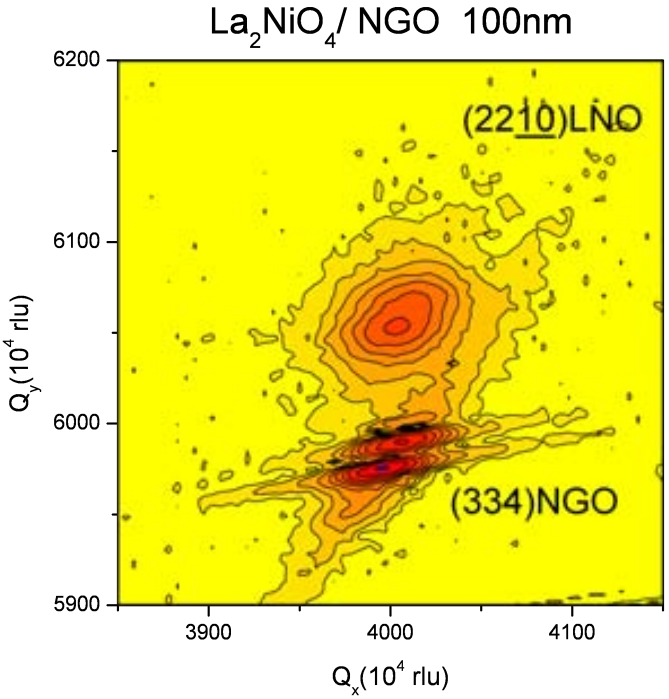

Figure 4.13: Reciprocal space map in which the $La_2NiO_{4+\delta}$ 22$\underline{10}$ reflection and the the 334 NGO substrate reflection appear.

The in-plane and out-of-plane lattice parameters as a function of the layer thickness between 25 and 375 nm for as-deposited films are shown in Figures 4.14 and 4.15, respectively. The variation of the cell parameters with thickness is related to the strain effect induced by the film/substrate mismatch and depends on the selected substrate surface structure. As STO presents a cubic structure we cannot distinguish between the two in-plane cell parameters (a and b), while NGO is orthorhombic with different pseudo-cubic in-plane parameters (3.863 and 3.854 Å), so

two different in-plane parameters can be distinguished in the deposited $La_2NiO_{4+\delta}$ film on NGO. The spread of values, particularly for STO, could be due to the lower quality of the epitaxy in comparison to the films deposited on NGO.

On NGO, the $La_2NiO_{4+\delta}$ a and b parameters increase (a from 3.849 Å at 22 nm to 3.856 Å at 373 nm and b from 3.856 Å at 33 nm to 3.860 Å at 330 nm; Figure 4.14) and the c-parameter decreases (from 12.719 Å at 33 nm to 12.697 at 375 nm; Figure 4.15) with thickness due to the compressive stress in the a-b plane induced by the film/substrate mismatch, while the opposite behavior is observed for the $La_2NiO_{4+\delta}$ cell parameters on STO (a decreases from 3.890 Å at 33 nm to 3.877 Å at 350 nm and c increases from 12.617 Å at 33 nm to 12.646 Å at 350 nm) due to the tensile stress. In summary, for both substrates, thinner films are strained (in an opposite direction for each substrate), while thicker films are more relaxed and tend to common cell parameter values. The total volume is not constant, it diminishes with the thickness for films deposited onto STO (from 191.57 $Å^3$ at 33 nm to 189.66 $Å^3$ at 350 nm) while it slightly increases with thickness for films deposited onto NGO (from 188.87 $Å^3$ at 33 nm to 189.14 $Å^3$ at 350 nm). Throughout the manuscript, when a set of data points have the same error, the error bars are indicated only for the first data point of each set, for the sake of clearness.

We have to point out that in bulk or ceramic samples the structure and lattice parameters for the $La_2NiO_{4+\delta}$ system depend and are related to the δ (oxygen overstoichiometry) value [39, 49, 109]. Unfortunately, in our case, as the samples are thin films and have a small mass, we cannot apply the standard methods to determine the oxygen stoichiometry. Thereby we could not assign any δ values to our films or associate the variation of the cell parameters with that of the δ value.

We have also estimated the strain of the films in the different crystallographic directions as:

$$E_{xx} = \frac{a_s - a_o}{a_o} \tag{4.5}$$

$$E_{yy} = \frac{b_s - b_o}{b_o} \tag{4.6}$$

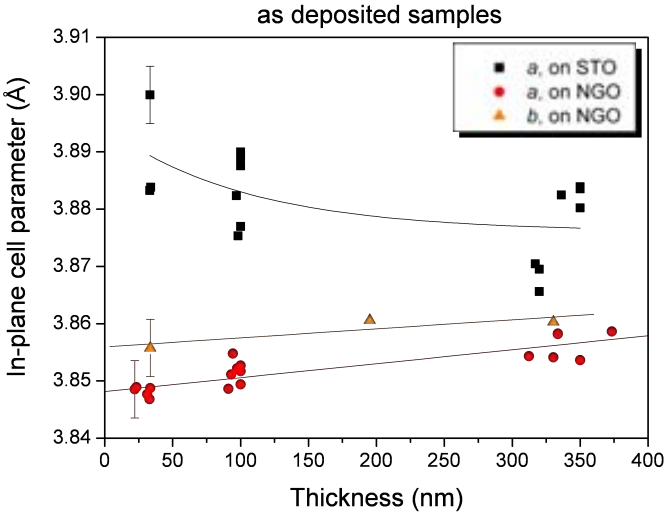

Figure 4.14: Variation of the in-plane cell parameter with thickness for as-deposited $La_2NiO_{4+\delta}$ films on both substrates.

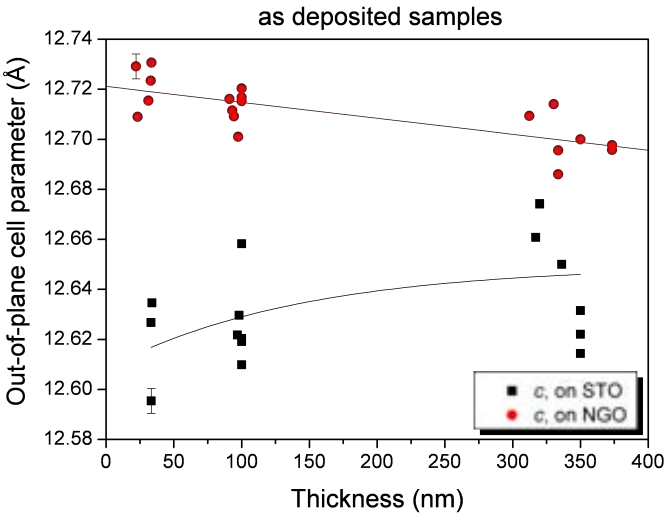

Figure 4.15: Variation of the out-of-plane cell parameter with thickness for as-deposited $La_2NiO_{4+\delta}$ films on both substrates.

$$E_{zz} = \frac{c_s - c_o}{c_o} \tag{4.7}$$

where E_{xx}, E_{yy} and E_{zz} are the strain in the x, y (a-b plane) and z (c-axis) directions; a_s, b_s and c_s are the stained cell parameter values (measured) and a_o, b_o and c_o are the cell parameters values in equilibrium (a_o = 3.8645 Å, b_o=3.8670 Å, c_o = 12.678 Å), considering the $La_2NiO_{4.18}$ structure reported by Metha and Heaney (ICSD Collection Code 44121) [107]), which are very close to the extrapolated values estimated from the representation of our measured cell parameters vs. film thickness.

We have measured a tensile strain in the a-b plane for the $La_2NiO_{4+\delta}$ films grown on STO which decreases with thickness from approximately 0.7 to 0.3% and a quite smaller compressive strain which varies from approximately -0.4 to -0.2% for films grown on NGO (Figure 4.16). In the perpendicular direction the opposite behavior occurs: for films deposited on STO a strain from approximately -0.5 to -0.3 % is observed, while on NGO the strain varies from approximately 0.4 to 0.2 %.

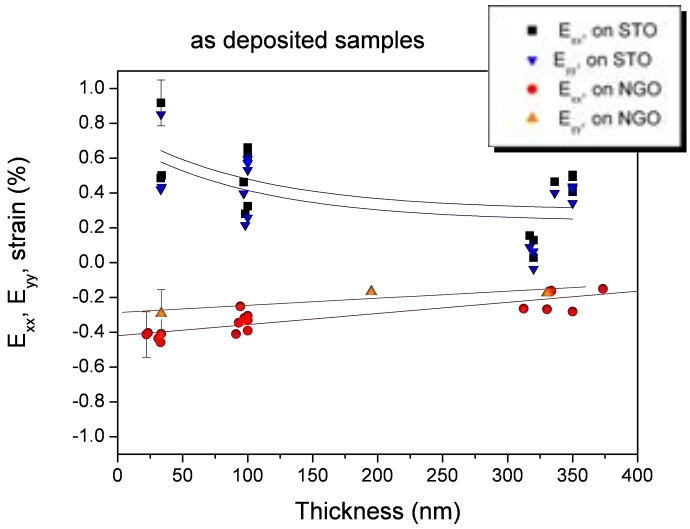

Figure 4.16: Variation of the in-plane strain with thickness for as-deposited $La_2NiO_{4+\delta}$ films on both substrates.

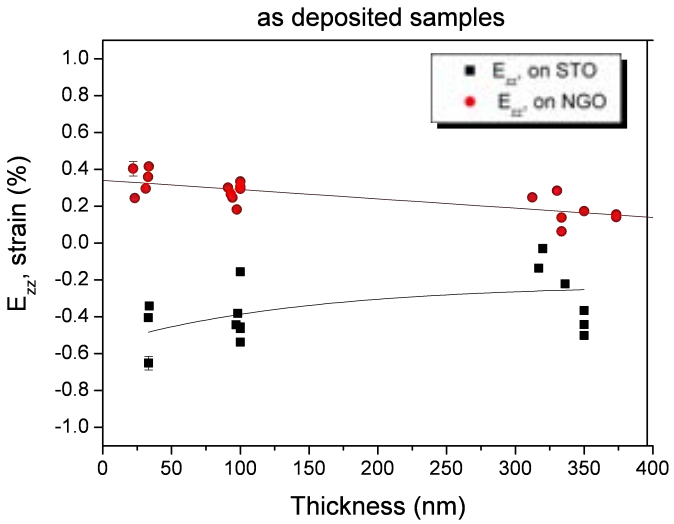

Figure 4.17: Variation of the out-of-plane strain with thickness for as-deposited $La_2NiO_{4+\delta}$ films on both substrates.

4.5 Structural Evolution of $La_2NiO_{4+\delta}$ Thin Films at High Temperature

4.5.1 Evolution of the *c*-parameter with Temperature and Atmosphere

Since this material is expected to work at high temperatures, we performed the structural characterization as a function of temperature by studying the variation of the *c*-parameter by high temperature XRD measurements in two different atmospheres, air and in nitrogen, in which the oxygen partial pressure is estimated to be around 50 ppm. The samples were first heated up to 973 K at a constant heating rate of 30 °C/min and the XRD patterns were performed during the cooling process following the procedure shown in Figure 4.18, in which the time lapse of each diffraction pattern is indicated (8 min). Several XRD patterns were collected at constant temperature to account for any evolution or decomposition. The temperature was lowered in a controlled way (20 °C/min) and five plateaux at 973, 773, 573, 373 and

298 K were programmed, permitting the acquisition of the diffraction patterns. The XRD patterns were performed from $2\theta = 65$ to $2\theta = 80°$ to detect the 00$\underline{10}$ reflection of the $La_2NiO_{4+\delta}$ and the 300 reflection or 330 reflection of the STO and NGO substrates, respectively, that were used for the determination of the c-parameter.

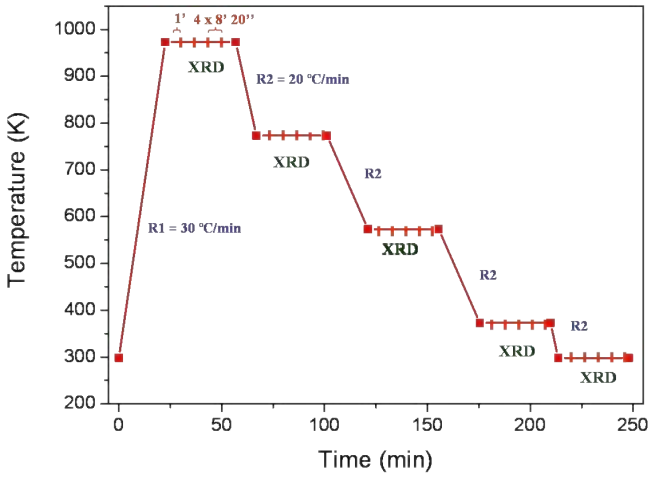

Figure 4.18: High temperature XRD measurements procedure.

An example of the XRD patterns between 71 and 76° for the 33 nm $La_2NiO_{4+\delta}$ thin film deposited on STO is shown in Figure 4.19. In it the evolution of the position of the substrate 300 and the film 00$\underline{10}$ peaks with the temperature can be seen. Due to thermal expansion, the cell parameters increase as the sample is heated, and therefore the position of the peaks are found at lower 2θ values. From the position of the 00$\underline{10}$ peak of the $La_2NiO_{4+\delta}$ phase, the c-parameter is calculated at each temperature, using as a reference the position of the 300 STO reflection at room temperature.

The c values determined during the cooling process after having stabilized the structure at each temperature are plotted in Figures 4.20 and 4.21 for films deposited on STO and on NGO substrates, respectively. The error bar for each data point in these two figures is approximately $\pm$ 0.005 Å, too small to be shown in the

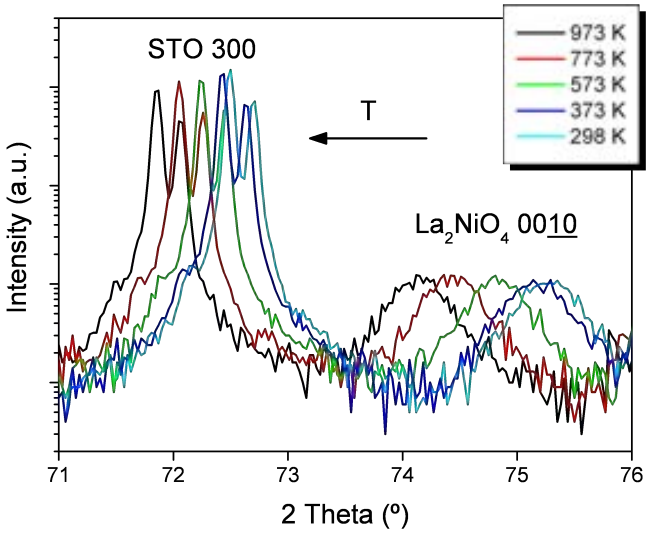

Figure 4.19: XRD patterns of a 33 nm $La_2NiO_{4+\delta}$ film deposited on STO recorded at different temperatures.

figures (as large as the data points). During the first measurement of the 330 nm $La_2NiO_{4+\delta}$ film on STO in air, the sample moved from its support and only the data corresponding to the first two temperatures could be registered. The experiment was then repeated in air in order to obtain the data for the whole temperature range and, it can be observed that slightly lower values of c were obtained at high temperatures.

We can observe in Figures 4.20 and 4.21 that, as expected, the c values are larger in air in comparison to nitrogen. This can be related to the fact that the δ equilibrium value of the $La_2NiO_{4+\delta}$ films should be higher at higher oxygen pressures and that the c-parameter is expected to increase with δ, as reported in the literature [39, 49, 109].

In Figure 4.20 we observe that for the $La_2NiO_{4+\delta}$ films deposited on STO the c-parameter increases linearly with temperature up to approximately 773 K, temperature above which the slope decreases, probably due to the oxygen loss predicted above this temperature. Skinner [110] has previously observed a decrease in the c parameter related to a decrease in the δ value at high temperatures, by the deter-

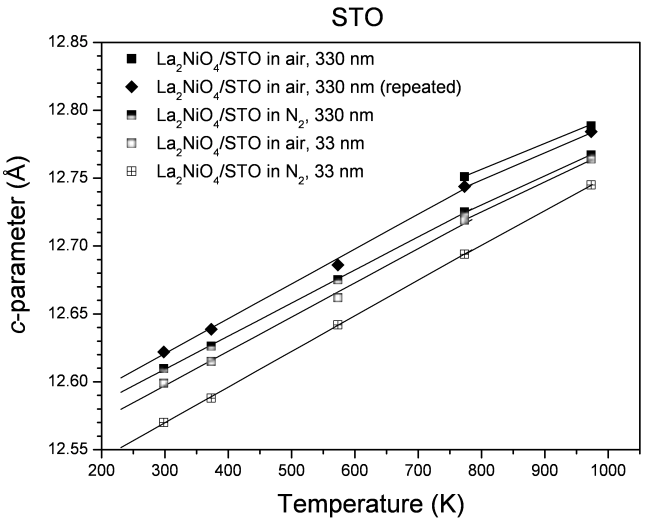

Figure 4.20: Variation of the out-of-plane cell parameters with temperature in air and in nitrogen for thin and thick $La_2NiO_{4+\delta}$ films deposited on STO substrates.

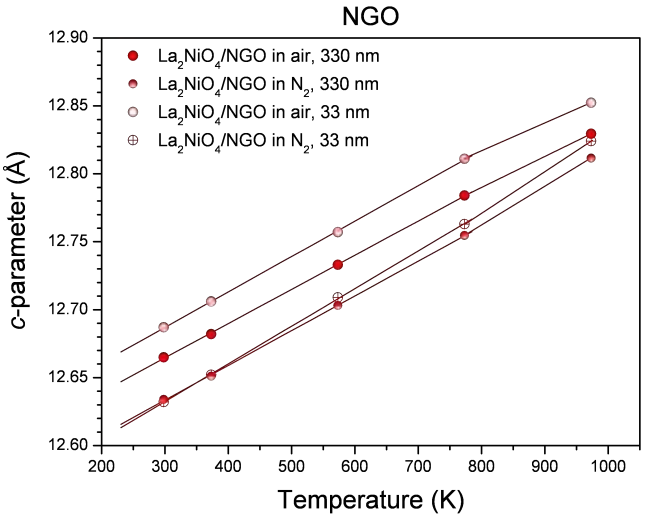

Figure 4.21: Variation of the out-of-plane cell parameters with temperature in air and in nitrogen for thin and thick $La_2NiO_{4+\delta}$ films deposited on NGO substrates.

mination of the $La_2NiO_{4+\delta}$ cell parameters from neutron diffraction measurements in vacuum during the heating and cooling process for $La_2NiO_{4+\delta}$ single crystal. In the case of the 33 nm thin film in nitrogen atmosphere, the change of slope between low and high temperatures is not appreciable, which we think could be due to a slower kinetic oxygen exchange in nitrogen atmosphere, enhanced for thinner, more stressed films. When the temperature is decreased from 973 to 773 K, oxygen is expected to be incorporated into the $La_2NiO_{4+\delta}$ films, and the c-parameter is then expected to be higher than the value which would be obtained by following the low temperature slope. If no oxygen is introduced into the film, the c-parameter is expected to follow the low temperature linear behavior. Slow oxygen exchange kinetics in nitrogen atmosphere have also been observed for the films grown on STO in this experiment (Figure 4.21) and, also, during the conductivity measurements, as will be explained next in Section 4.6. In addition, this is in agreement with the smaller chemical surface exchange coefficient measured by us by electrical conductivity relaxation measurements for thin more stressed films in comparison to thicker more relaxed films. These results will be explained in detail in Section 5.3.

We can also observe that the difference in the out-of-plane cell parameter between the two gas atmospheres ($\Delta c = c_{air} - c_{nitrogen}$) is larger for the thin 33 nm $La_2NiO_{4+\delta}$ film than for the thick 330 nm $La_2NiO_{4+\delta}$ film grown on STO. This larger difference could be associated to a larger difference in oxygen content $\Delta\delta$ in the $La_2NiO_{4+\delta}$ film between air and nitrogen atmosphere, or to the oxygen exchange limitation in nitrogen atmosphere previously mentioned. The 33 nm $La_2NiO_{4+\delta}$ thin film, due to a larger stress, might not be able to incorporate fastly as much oxygen as the thicker 330 nm film during the cooling process in nitrogen atmosphere. Therefore, the thin $La_2NiO_{4+\delta}$ film might have a lower δ content in comparison to the thick $La_2NiO_{4+\delta}$ film at low temperatures in nitrogen atmosphere, and therefore a larger $\Delta\delta$ difference.

In Figure 4.21 we can observe the variation of the c-parameter with temperature in air and in nitrogen atmosphere for films deposited on NGO substrates. As in the case of the films deposited on STO, the difference in c between both atmospheres (Δc) is larger for the thin, more strained film. For both samples, the c parameters increase linearly with temperature and a slight change in the slope is also detected

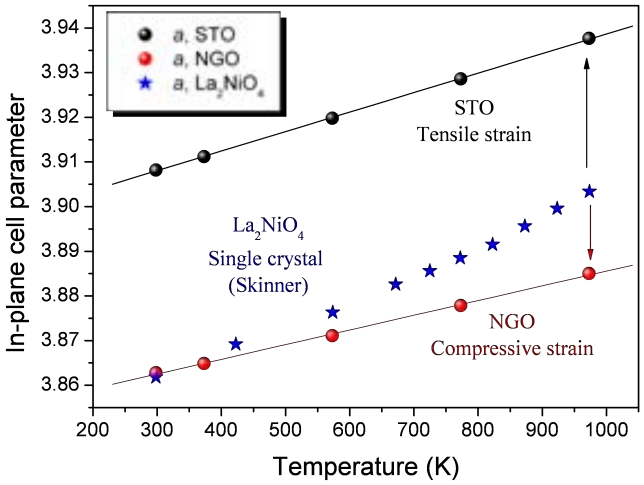

Figure 4.22: Variation of the in-plane cell parameters with temperature for NGO and STO substrates and for $La_2NiO_{4+\delta}$ single crystal from Ref. [110].

above 773 K. In air atmosphere the expected slope decrease associated to an oxygen loss is observed, while in nitrogen atmosphere the slope is larger at high than at low temperatures. This slope change, in this case, seems not to be related to the loss of oxygen in the $La_2NiO_{4+\delta}$ films but to the kinetic limitation previously mentioned and, possibly, to an added strain effect. In Figure 4.22 the variation of the NGO and STO substrate cell parameters measured by us are plotted together with the in-plane cell parameters measured by Skinner [110] in vacuum for $La_2NiO_{4+\delta}$ single crystals. It is clearly observed that the thermal expansion coefficient (TEC) of the STO and NGO substrates is smaller than that of the in-plane parameters of the $La_2NiO_{4+\delta}$ single crystal. The smaller expansion of the substrate is expected to limit the expansion of the in-plane of the $La_2NiO_{4+\delta}$ structure for the film grown on top. We can expect the films grown on NGO to be subjected to a compressive strain, which will increase with temperature (as the difference in cell parameters between the $La_2NiO_{4+\delta}$ single crystal and the substrate increases with temperature), and for films grown on STO subjected to a tensile strain, which will decrease with

temperature. Thus, for films grown on NGO, as the temperature increases, the strain will become larger and, as a result, a larger expansion of the c-parameter may be occuring to compensate the in-plane expansion limitation (which is in agreement with observations in Figure 4.21).

To have a deeper understanding of the relationship between the strain, δ, the temperature and the gas atmosphere, the oxygen content and the in-plane cell parameters of the $La_2NiO_{4+\delta}$ thin films should also be measured as a function of temperature, which, unfortunately, has not been possible with the diffractometer used.

To complete the study of the $La_2NiO_{4+\delta}$ structure as a function of the surrounding atmosphere, we have also measured the c-parameter evolution at 973 K switching the atmosphere from air to nitrogen as shown in Figure 4.23. These measurements have also been performed with the high temperature X-ray Diffractometer by measuring the same $00\underline{1}0$ reflection of the $La_2NiO_{4+\delta}$. The films have been heated up to 973 K and, once the temperature has been reached, a XRD pattern has been acquired every 8 minutes. After approximately one hour the atmosphere was rapidly changed to pure nitrogen, and the same process was repeated for another 60 minutes. This procedure was repeated two or three times depending on the sample.

Different observations can be done from this experiment. The first one is that the c-parameter seems to be stable in air, and not so stable in nitrogen, atmosphere in which the c-parameter decreases slightly with time. This structural change with time could be an irreversible process, as after a new gas change to air the c-parameter does not recover its previous value, but a slightly lower one. This irreversibility may be due to effects of strain release or nonstoichiometry.

The stabilization kinetics of the c-parameter after an atmosphere variation depends on the final gas atmosphere. The c-parameter stabilizes in a few seconds when atmosphere is switched from nitrogen to air, while the contrary occurs when the switch is from air to nitrogen, that is, the c-parameters decrease slowly and it takes from 15 to 30 minutes to reach a quasi-stabilized value. From this behavior it can be deduced, that the oxygen exchange in air atmosphere is kinetically more favorable than the oxygen exchange in nitrogen atmosphere.

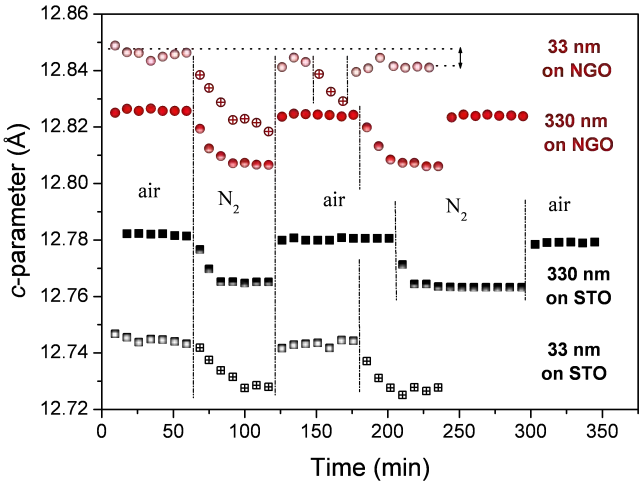

Figure 4.23: *c*-parameter evolution at 973 K by switching the gas atmosphere from air to nitrogen, for $La_2NiO_{4+\delta}$ films deposited on NGO and STO substrates.

4.5.2 Stability Studies

As this material could be applied as a cathode in electrochemical devices, and thus, it would be submitted to an oxidizing atmosphere for long periods of time, we have also performed aging experiments. A thick $La_2NiO_{4+\delta}$/NGO film (330 nm) was heated at 600 °C during 400 h and consecutively to 800 °C for the same period of time. The aging effects were characterized by performing XRD patters at room temperature before and after each treatment (Figure 4.24).

No major structure variation was detected (Figure 4.24.b) after the treatment at 600 °C for 400 h. On the contrary, after the ageing at 800 °C a broadening and loss of intensity of the 00l $La_2NiO_{4+\delta}$ reflections along with extra peaks assigned to the presence of La_2O_3 phase impurities (Figure 4.24.c) were detected. Other authors [62] have detected the formation of a mixed valence Ni^{2+}/Ni^{3+} oxide phase after a thermal aging at 900 °C of bulk $La_2NiO_{4+\delta}$ samples, but those phases were not observed in our case.

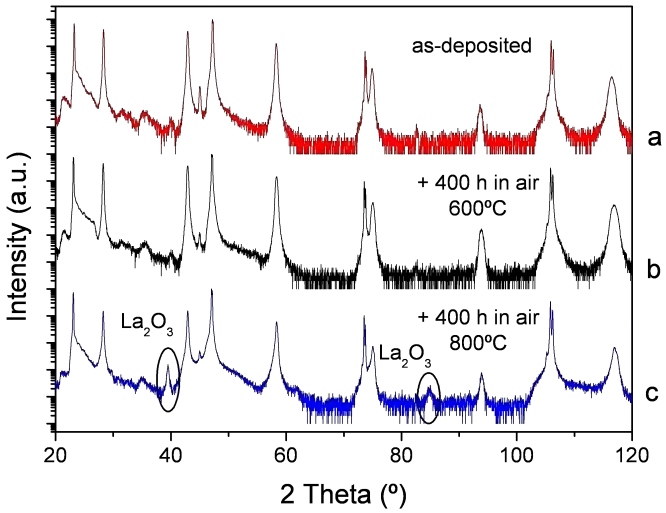

Figure 4.24: XRD patterns of a 330 nm thick film deposited on NGO (a) as-deposited (b) after a 400 h anneal in air at 600 °C (c) after a 400 h anneal in air at 800 °C.

4.6 Total Conductivity Properties of $La_2NiO_{4+\delta}$ Thin Films

As already mentioned, $La_2NiO_{4+\delta}$ is expected to be highly anisotropic in the total conductivity, both ionic and electronic, showing maximum transport along the *a*-*b* planes of the structure. In our case, as the films have been epitaxially grown with the *c*-axis perpendicular to the surface of an insulating substrate, the measured conductivity corresponds to that along the *a*-*b* planes.

The measurements have been performed on films of different thickness from 33 to 335 nm deposited on two different substrates and as a function of temperature from room temperature to 700 °C, with constant temperature plateaux every 50 °C. In Figure 4.25, in which the conductivity measured in oxygen atmosphere is plotted as a function of temperature, it can be seen that, as expected, the total conductivity increases with temperature and reaches a maximum around 400-450 °C. Above this temperature, the conductivity starts to decrease due to a depletion of oxygen from the lattice [25, 110–112], which had been already detected in the XRD high temperature experiments. The errors in the value of the conductivity for the different films have been estimated to be of approximately 10% for thin films and up to 25% of the conductivity value for films thicker than 100 nm, and are mainly due to the errors associated to the film thickness measurement, which for thick films cannot be directly measured and is therefore estimated from WDS measurements.

We have to notice that the conductivity of the substrate is several orders of magnitude smaller than that of our layers: for STO $\approx 10^{-3}$ S/cm and for NGO $\approx 10^{-6}$ S/cm at 700 °C. So, even for the thinner films, the conductance of the substrate (0.5 mm thick) is negligible, confirming that we are measuring the layer conductivity, without influence of the substrate.

In Figure 4.26 the total conductivity for $La_2NiO_{4+\delta}$ films deposited on both samples is plotted vs the inverse of the temperature, together with the measurements reported in the literature for $La_2NiO_{4+\delta}$ single crystals and polycrystal bulk ceramics. The total conductivity increases with temperature following a thermally activated behavior. At high temperatures all the $La_2NiO_{4+\delta}$ measured films have conductivity values higher than the bulk polycrystalline sample measured by Amow

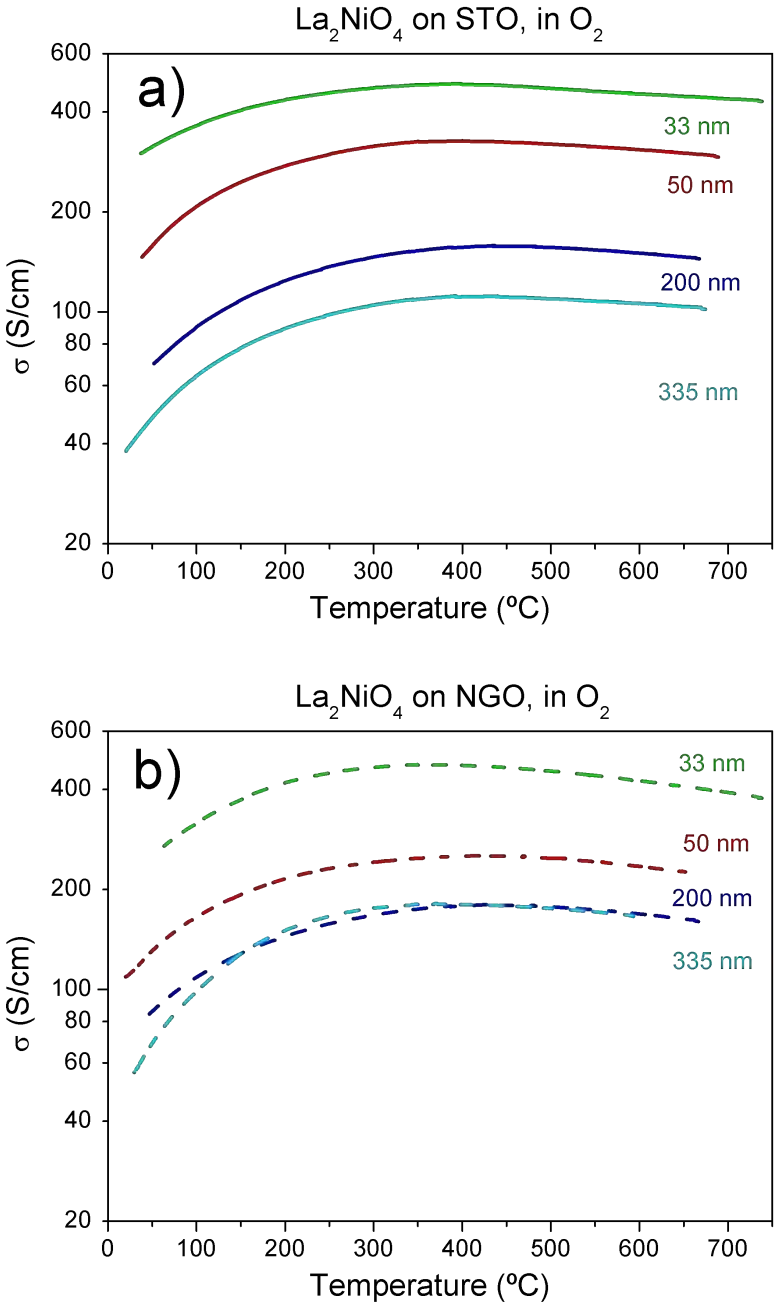

Figure 4.25: Total conductivity of $La_2NiO_{4+\delta}$ epitaxial films as a function of temperature for films of different thickness deposited a) onto STO b) onto NGO in oxygen atmosphere.

and Skinner [62]. Only the thickest film (335 nm) deposited on STO had, at room temperature, a similar conductivity to the bulk. Samples thinner than 200 nm grown on both substrates have a larger conductivity values than $La_2NiO_{4+\delta}$ single crystals reported by Dembinski et al. [64]. The maximum conductivity, obtained for 33 nm samples deposited onto STO and NGO in oxygen is close to 475 S/cm, above the reported values to date for polycrystalline bulk ceramics and films (maximum ≈ 80 S/cm) [26, 57, 58, 61–63, 85], and even on single crystal samples along the *a*-*b* plane (maximum ≈ 200 S/cm) [59, 64]. This fact seems to confirm the high quality of our samples.

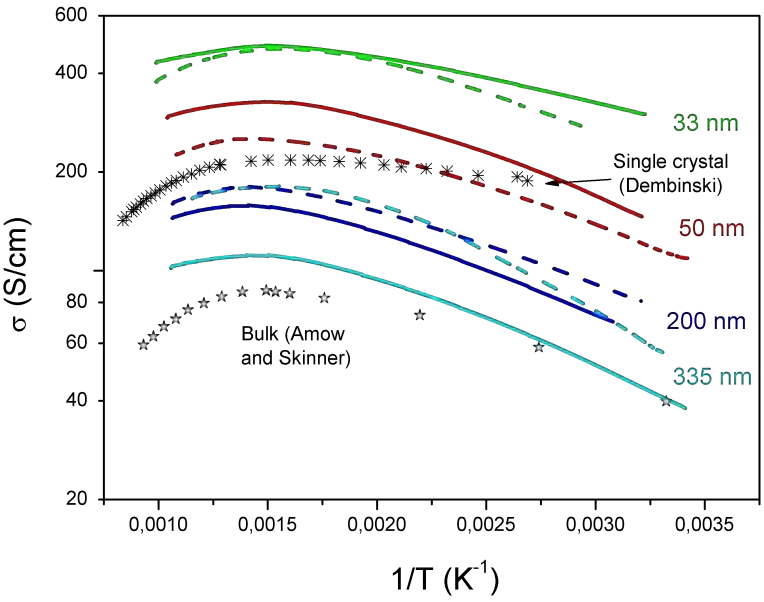

Figure 4.26: Total conductivity of $La_2NiO_{4+\delta}$ epitaxial films as a function of the inverse of the temperature for films of different thickness deposited onto STO and NGO in oxygen atmosphere and comparison with literature data for single crystals and bulk ceramics in air.

The in-plane conductivity of our samples was measured in different atmospheres, to observe the influence of oxygen partial pressure. In Figure 4.27 the Arrhenius

representation of the total conductivity in pure oxygen, in air and in nitrogen is plotted for 33 nm thick $La_2NiO_{4+\delta}$ films deposited on both substrates. The conductivity shows a linear dependence with temperature from room temperature to 400 °C, corresponding to a semiconducting-type behavior. As already mentioned, at higher temperatures, the material looses oxygen, leading to a Ni^{3+} content decrease along with the reduction of the carrier density [25, 110–112]. These phenomena result in a decrease of the conductivity slope as the temperature increases. For the film deposited on STO it is observed that in nitrogen atmosphere and at intermediate temperatures the conductivity value varies during the plateaux at constant temperature. This variation seems to be associated to a slow kinetic process, which has also been observed, as will be shown subsequently, for larger thickness films deposited on STO (Figure 4.28.c). A variation of the conductivity with time, although less pronounced, also appears for films grown on NGO, as will be observed in Figure 4.31 and explained subsequently. In addition this phenomenon has also been observed during the electrical conductivity relaxation measurements, detailed in Section 5.3.

Furthermore, the conductivity in oxygen shows slightly higher values than in air and considerably higher than in nitrogen. The dependence with temperature and oxygen partial pressure confirms that the conductivity is predominantly p-type electronic and occurs via small-polaron mechanism, indicated by temperature-activated hole mobility and $p(O_2)$ dependencies of electrical properties [58, 111]. The corresponding values of activation energy (E_a) have been calculated by the adiabatic small polaron hopping model:

$$\sigma = \frac{A_o}{T} exp(-\frac{E_a}{RT}) \tag{4.8}$$

from the representation of σT vs 1/T, as is shown in Figure 4.28. The results are shown in Table 4.3. The small activation energy of the total conductivity measured for our samples is characterized for $La_2NiO_{4+\delta}$, and is in all cases in the typical range (50-100 meV) found by other authors below 600 K [57–60].

The activation energy increases with thickness for films deposited on both substrates, but we do not observe a clear variation with the substrate or the gas atmosphere. The variation with thickness could be related to a strain effect produced by the lattice mismatch, as reported by Chen et al. for $La_{0.9}Sr_{0.1}MnO_3$ thin films

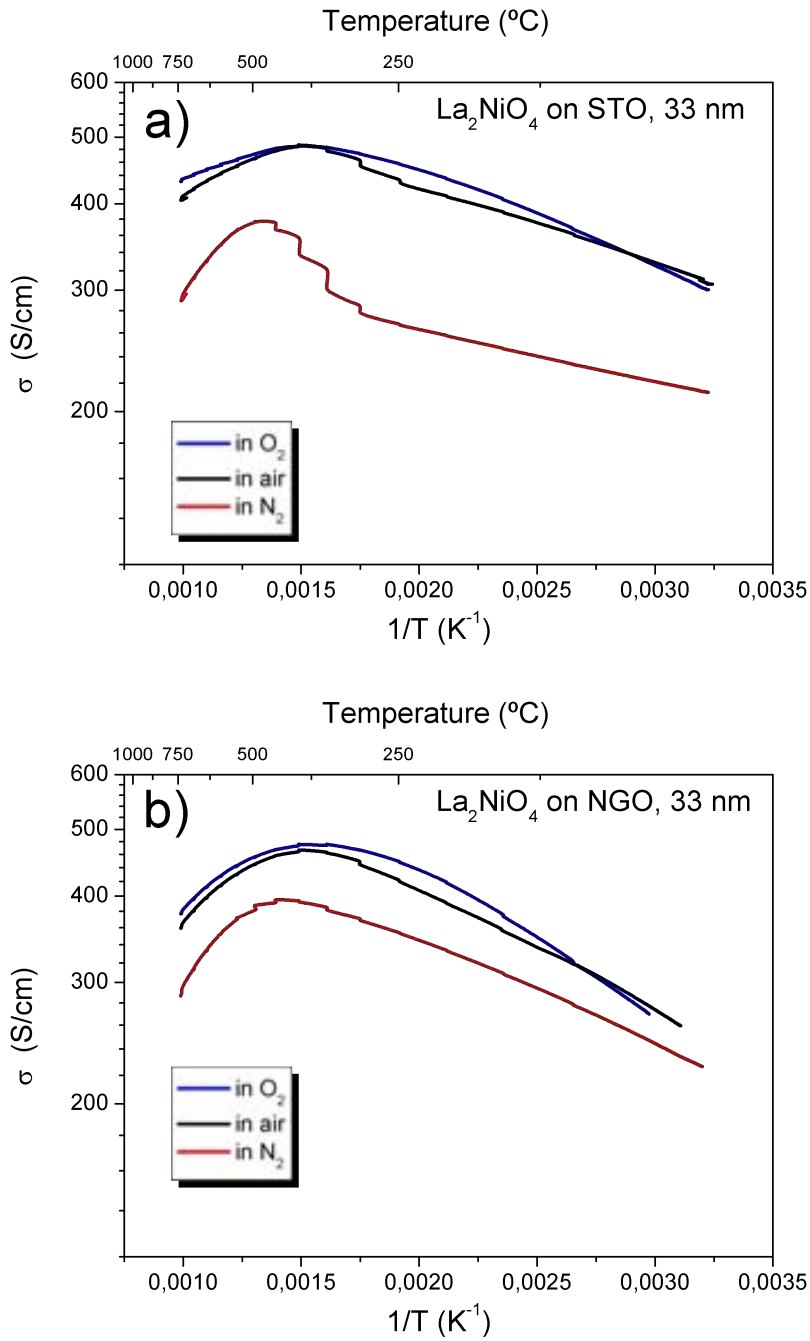

Figure 4.27: Total conductivity of $La_2NiO_{4+\delta}$ epitaxial films as a function of the gas atmosphere for a 33 nm thick film deposited a) onto STO, b) onto NGO.

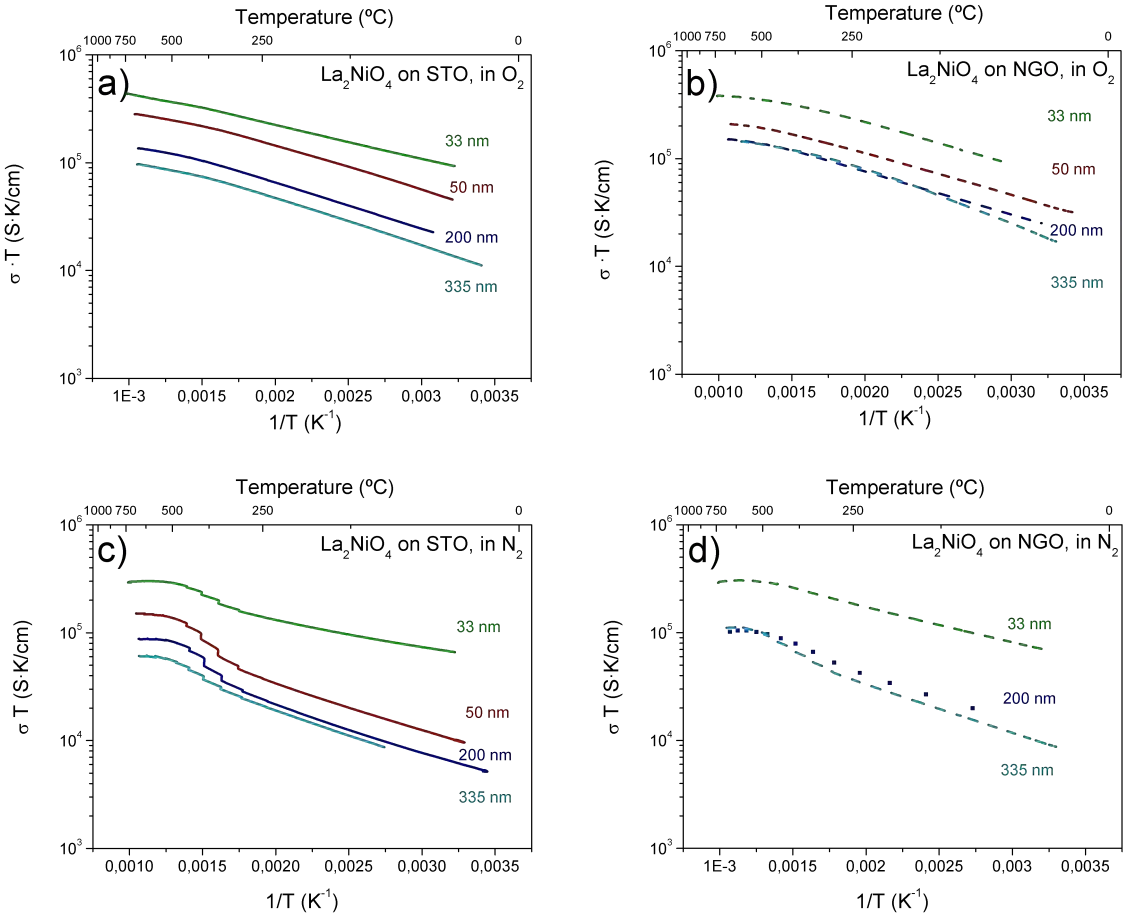

Figure 4.28: Total conductivity of $La_2NiO_{4+\delta}$ epitaxial films as a function of the temperature a) under oxygen for films deposited onto STO, b) under oxygen for films deposited onto NGO, c) under nitrogen for films deposited onto STO and d) under nitrogen for films deposited onto NGO. Activation energies are shown in the figure corresponding the for the thermally activated temperature range.

Table 4.3: Conductivity activation energies for the different thickness films deposited on STO and NGO in oxygen and nitrogen atmosphere

Thickness	STO		NGO	
	Oxygen	Nitrogen	Oxygen	Nitrogen
33 nm	62 meV	48 meV	75 meV	66 meV
50 nm	81 meV	84 meV	76 meV	66 meV
200 nm	84 meV	84 meV	79 meV	87 meV
335 nm	87 meV	94 meV	106 meV	91 meV

deposited on STO at low temperatures [113]. The oxygen content probably also plays a role, as observed for the perovskite related mixed conductor $Sr_3Fe_2O_{6+\delta}$ [114]. In our case, as we cannot measure the oxygen content of the films by the conventional methods, we do not have enough information to discuss the variation of the activation with thickness as a function of δ.

We have to notice that, independently of the substrate used, the total conductivity of the samples increases considerably as the film thickness decreases. The effect of thickness is more clearly seen if we plot the maximum conductivity reached as a function of film thickness, which for the measurements in O_2 corresponds to the value extracted around 450 °C. In Figure 4.29 it is observed that for the thinnest films and at a fixed atmosphere, the maximum conductivity does not depend on the substrate used. For films deposited on NGO the conductivity reaches a minimum of approximately 180 S/cm at 200 nm, while for films deposited on STO the conductivity continued decreasing up to the highest thickness measured films.

Many parameters can simultaneously affect the total transport properties of the $La_2NiO_{4+\delta}$ thin films. The films on different substrates and of different thickness will undergo an epitaxial strain with different value and sign, as already discussed in Section 4.4. In Figure 4.30 the maximum conductivity in oxygen atmosphere is plotted as a function of the absolute value of the in-plane strain (without the sign) at room temperature for films grown on both substrates. It is observed that the conductivity value increases with strain for films deposited on both substrates.

Another aspect to be taken into account is the oxygen content. The conductivity

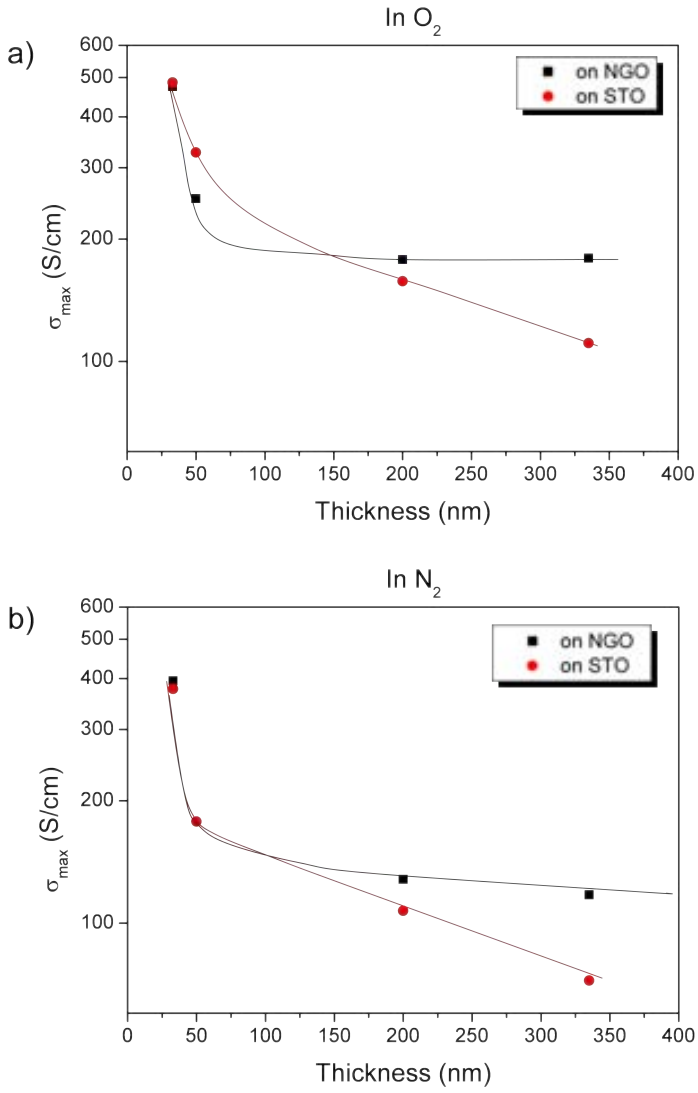

Figure 4.29: Maximum conductivity (at 450 °C) of $La_2NiO_{4+\delta}$ epitaxial films a) in oxygen and b) in nitrogen atmosphere as a function of the thickness for films deposited onto STO and NGO.

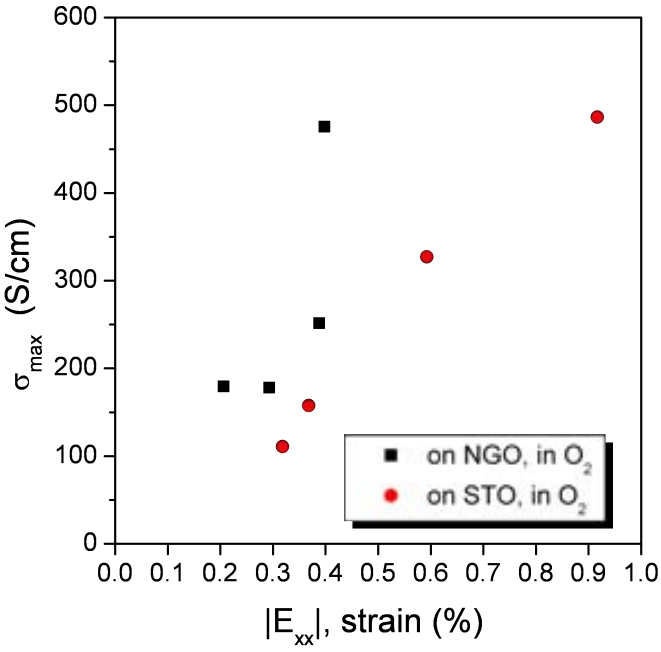

Figure 4.30: Maximum conductivity of $La_2NiO_{4+\delta}$ epitaxial films in oxygen atmosphere as a function of the in-plane strain for films deposited onto STO and NGO.

is expected to increase by increasing δ, which for bulk samples corresponds to an increase in the c parameter. In our case, the different strain sign induces different c values for different thicknesses and substrates, but unfortunately we cannot measure the oxygen content variation of our films, as we have previously mentioned, and thus the contribution of δ to the conductivity cannot be evaluated.

At the same time, the microstructure of the films can affect their transport behavior. Even though the density of antiphase boundaries and the possible existence of a buffer layer is different between films grown on NGO and on STO, we have measured quite similar conductivity values for the thinnest films deposited on the different substrates. Therefore the different microstructural defects between the films do not seem to have a direct effect in the transport properties of the same.

Finally, the electronic transport may not be occuring uniformly through the whole film thickness, as there could be a surface effect, zone in which the conductivity could be enhanced. This is particularly difficult to prove and goes beyond the scope of this work.

In summary, several parametes can affect the conductivity in a competing or cooperative way. Thus, it is difficult to separate and quantify each contribution affecting the total conductivity increase. As a general trend, we can only conclude that the conductivity increases with reducing thickness.

We have also performed a study on the conductivity stability at high temperature. We have measured the conductivity of a 200 nm thick $La_2NiO_{4+\delta}$ film deposited on NGO as a function of time at a temperature of 847 K (574 °C) varying the gas atmosphere from oxygen to nitrogen as shown in Figure 4.31. Initially the sample was heated up in oxygen and, once the conductivity had reached a stable value, the atmosphere was switched to pure nitrogen, process which was accompanied by a large decrease in conductivity. After 80 min, the atmosphere was switched again to pure oxygen, and this procedure was repeated 3 times before stabilizing the sample in pure oxygen. At this point a slight reduction of the conductivity from its initial value was observed. The procedure was repeated again, stabilising the sample in nitrogen, atmosphere in which we observed the expected initial drop in conductivity, and a further slow decrease which continued with time during the 15 hours measured. After a new gas change cycle and its subsequent stabilization in oxygen, we

observed a loss of conductivity of 18% from the initial value. It is clearly observed that the measured value of the conductivity is more stable in oxygen than in nitrogen atmosphere, in which its value decreases gradually. This change with time is an irreversible process, as after a new gas change to air the conductivity value does not recover its previous value. This irreversibility may be associated to the change of the *c*-parameter of the $La_2NiO_{4+\delta}$ films observed at high temperature in nitrogen atmosphere, described in Section 4.5.2 in page 87, or to the influence of the silver contacts in reducing atmosphere, which could evolve with time or interact with the film. The X-ray diffractogram of the thin film after this conductivity stability study showed the appearance of peaks corresponding to the La_2O_3 phase, similar to those observed after an anneal in air at high temperature during several weeks (Figure 4.24).

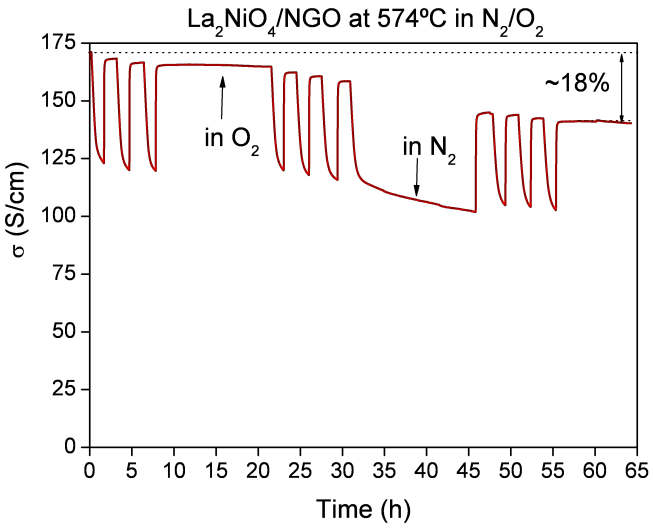

Figure 4.31: Variation of the conductivity with time at 847 K by changing the gas atmosphere from air to nitrogen, for a 200 nm $La_2NiO_{4+\delta}$ films deposited on NGO.

4.7 Conclusions

In this Chapter we have determined the optimal experimental parameters to prepare epitaxial thin films of $La_2NiO_{4+\delta}$ on different substrates using the Pulsed Injection Metal Organic CVD technique.

By using XRD we have characterized the variation of the in- and out-of plane cell parameters with thickness at room temperature from thin strained to thick more relaxed films. The evolution of the *c*-parameter as a function of temperature has also been measured for different thickness films deposited on both substrates. From the evolution of the *c*-parameter as a function of temperature, we have been able to appreciate the oxygen loss at high temperatures in air atmosphere and a slower oxygen exchange kinetics in nitrogen, compared to air atmosphere. This kinetic limitation in nitrogen atmosphere is emphasized in the case of thin, more stressed films grown on both substrates and is in agreement with observations in the conductivity and ECR measurements.

Transport measurement of the films allowed us to determine the conductivity along the *a*-*b* plane of $La_2NiO_{4+\delta}$ as a function of temperature and oxygen partial pressure. As expected the conductivity has shown a thermally activated behavior typical for p-type polaron hopping mechanism for temperatures up to 425 °C and the activation energy of the thermally activated process has been found to increase with thickness.

The conductivity has been found to increase with reducing thickness showing a maximum conductivity of 475 S/cm around 425 °C in 33 nm thick films, corresponding to the highest value reported to date for this compound to our knowledge. The physical mechanism explaining the higher conductivity values measured for the thinner films is still unclear as no real evidence of the effect of lattice parameters or oxygen stoichiometry has been found or measured, respectively. The factors which seem to play a role in the total conductivity increase are the thickness and the absolute strain value.

We can also conclude that our samples easily fulfill the requirement of about 100 S/cm to be used as cathodes in SOFC.

Chapter 5

Oxygen Exchange and Transport Properties of $La_2NiO_{4+\delta}$ Thin Films

5.1 Relevant Exchange and Transport Parameters of Solid Oxides

Knowledge of the relevant transport parameters of solid oxides is of fundamental importance in the development of high temperature solid state electrochemical devices. A variety of techniques has been developed, by which it is possible to determine, in addition to bulk transport coefficients, surface exchange constants.

There are three fundamental experimental techniques usually applied to obtain transport coefficients (Figure 5.1): the electrical experiment (a), the tracer experiment (b), in which the tracer distribution is changed ($M^{18}O_x{}^{16}O_{1+\delta-x} \rightarrow M^{18}O_{x+\Delta x}{}^{16}O_{1+\delta-x-\Delta x}$) and the chemical experiment (c), in which the stoichiometry is changed ($MO_\delta \rightarrow MO_{\delta'}$) [115]. In the first one (a), the electrical measurement, an outer electrical potential gradient is applied as a driving force. In the case of an ionic conductor, the internal ionic current is balanced by an outer electronic current, that is measured. In the second one (b) a tracer composition (c^*: tracer concentration) gradient, i.e., a gradient in the tracer chemical potential is applied, the ionic

flux of the tracer being counterbalanced by the ionic flux of the counter-isotope. In the last experiment (c) an outer chemical composition gradient is applied and an internal one is induced in the sample. So, in contrast to the first two experiments, true chemical potential gradients are involved, and in the case of a mixed ionic-electronic conductor, the ionic flux is necessarily counterbalanced by an internal electronic current. Hence, both ions and electrons are necessarily involved in the effective kinetic parameters evaluated.

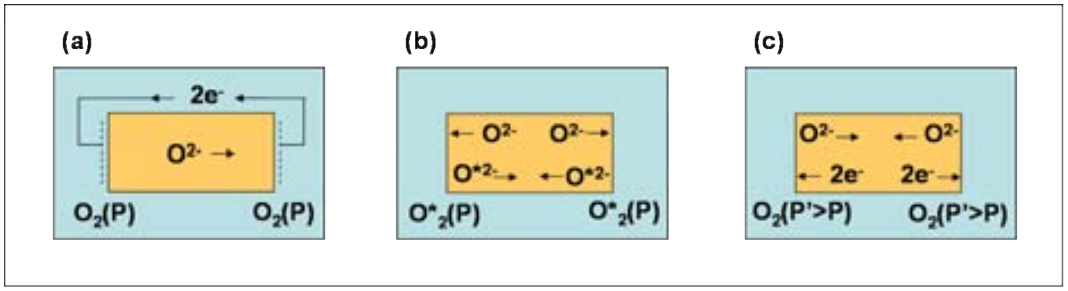

Figure 5.1: The three basic experiments to measure transport coefficients [115].

The information obtained from the experiments a, b and c can be converted into three different diffusion coefficients: D_Q , D^* and D_{Chem} and three rate constants: k_Q, k^* and k_{Ex}, respectively. The experimental rate constants derived from electrical experiments (e.g. impedance spectroscopy), tracer experiments and chemical experiments (e.g. electrical conductivity relaxation) under small excitations and dilute conditions are not only different, since they may refer to different materials combinations (e.g. electrodes necessary in electrical experiments), but also for mechanistic and conceptional reasons. The mechanistic reasons are due to the fact that even if referring to the same materials, the rate limiting step can be different. Since in a chemical diffusion experiment involving a mixed ionic-electronic conductor, a reduction or an oxidation takes place, the electron's role may be different from a tracer experiment (in which electrons appear only as an intermediate) as well as from electrical experiments in which electron transfer involves an electrode. 'Electron-rich', in contrast to 'electron-poor' materials, are materials for which the electron carrier concentration (i.e. electrons or holes) is great enough to be taken as a constant in

the kinetic equations; in addition, it is assumed that purely electronic steps (e.g. surface diffusion of electronic carriers) are fast. For electron-rich compounds the rate limiting step is expected to be the same for the different experiments and the rate constants are then shown to the related in an analogous way to the bulk diffusion coefficients: k_{Ex} (chemical experiment)$/w_o = k^*$ (tracer experiment), D_{Chem} (chemical experiment)$/w_o = D^*$ (tracer experiment), where w_o is a thermodynamic factor and k^* (tracer experiment) $\approx k_Q$ (conductivity experiment), D^* (tracer experiment) $\approx D_Q$ (conductivity experiment), provided that the experimental conditions are comparable. The "chemical k" (k_{Ex}) can be orders of magnitudes higher than the "tracer k" (k^*) due to the difference between the concentrations of regular and defective constituents [115, 116].

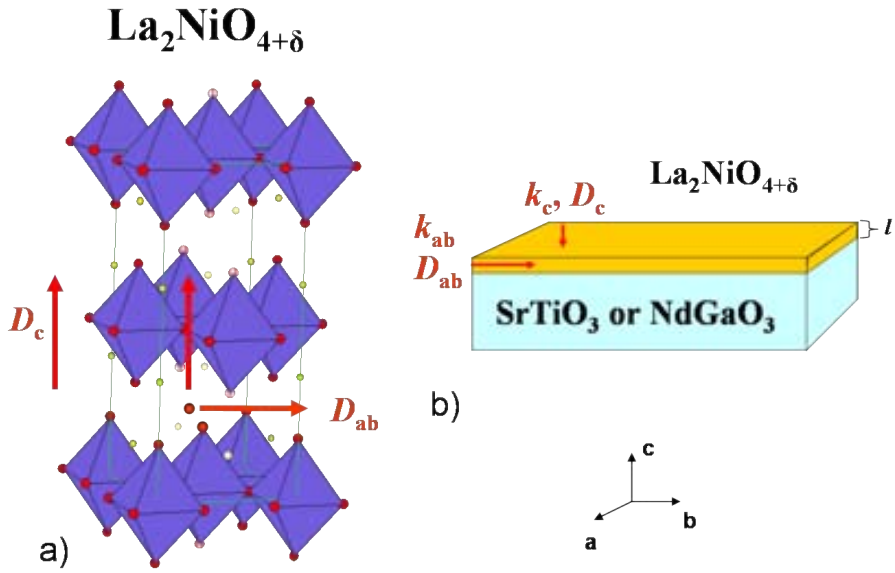

Figure 5.2: a) Representation of the La_2NiO_4 structure with interstitial defect site. The direction of two anisotropic oxygen diffusion coefficients are marked; b) Representation of a $La_2NiO_{4+\delta}$ film of thickness l grown on a STO or NGO substrate. The two anisotropic surface exchange and oxygen diffusion coefficients are shown.

In $La_2NiO_{4+\delta}$ the oxygen diffusion is expected to be highly anisotropic independently of the mechanism considered [24, 50], with two different surface exchange and diffusion coefficients for the two perpendicular directions considered: a-b plane

and c-axis. Figure 5.2 represents a scheme of the La_2NiO_4 structure with interstitial defect site together with the direction of two anisotropic oxygen diffusion coefficients. In addition a $La_2NiO_{4+\delta}$ film of thickness l grown on a STO/NGO substrate is shown with the two anisotropic surface exchange and oxygen diffusion coefficients. In ceramic materials with polycrystalline structure and thus randomly oriented grains, the anisotropy is averaged and the diffusivity value depends mainly on the connectivity between grains. To extract any information about the intrinsic anisotropy of the oxygen diffusion it is then necessary to analyze samples of materials with a high degree of crystal orientation and a low density of grain boundaries and defects. This is accomplished either by using single crystals, or highly textured polycrystalline samples. Furthermore, in the case of epitaxial thin films the ionic transport properties could be modified by varying the film strain or the thickness, as has already been seen.

In this work we have used two of the previously described experimental techniques to characterize the $La_2NiO_{4+\delta}$ thin films and determine the correspondent diffusion and surface exchange coefficients: the tracer experiment (oxygen isotope exchange), described in Section 5.2, and the chemical diffusion experiment (electrical conductivity relaxation experiment), described in Section 5.3. As it is clear from the scheme, measurements of k^*_{ab} and D^*_c have been complicated due to the small film thicknesses.

5.2 Oxygen Isotope Exchange on $La_2NiO_{4+\delta}$ Thin Films

5.2.1 Oxygen Isotope Exchange Principles

The oxygen isotope exchange technique is commonly applied to measure the tracer diffusion coefficient and surface exchange coefficient of a specimen, and consists of exchanging the ambient oxygen surrounding an oxide, which is usually an isotope mixture primarily made up of ^{16}O, with a gas enriched with ^{18}O (or ^{17}O). The specimen is usually pre-treated in the oxygen partial pressure and temperature of the exchange measurement itself in order to establish thermodynamic equilibrium and prevent effects of chemical diffusion within the sample bulk. The consequence of a difference between the tracer content of the gas and that of the solid phase is a

tracer exchange in the solid, which for the $La_2NiO_{4+\delta}$ oxide would be:

$$La_2Ni^{18}O_x{}^{16}O_{4+\delta-x} \rightarrow La_2Ni^{18}O_{x+\Delta x}{}^{16}O_{4+\delta-x-\Delta x} \tag{5.1}$$

The total oxygen content ($^{16}O + {}^{18}O$) of the $La_2NiO_{4+\delta}$ oxide remains constant during the exchange process, that is, the chemical composition is not altered. And so, this tracer diffusion is in fact a counterdiffusion of the two oxygen isotopes [117].

Data on these coefficients can be obtained from isotope exchange depth profiling by Secondary Ion Mass Spectroscopy after partial isotope exchange has taken place at the desired temperature and oxygen pressure. The tracer diffusion coefficient and the surface exchange coefficient are obtained by curve fitting of the measured profile to the appropriate equation, which is deduced from the solution to Fick's second law:

$$\frac{\partial c^*(x,y,z,t)}{\partial t} = D^*\nabla^2 c^*(x,y,z,t) \tag{5.2}$$

with the appropiate initial and boundary conditions. c*(x,y,z,t) is the isotopic concentration at the point (x,y,z) at time = t. In the derivation of the model equations, it is assumed that a stepwise change in the ^{18}O partial pressure is supplied to the system at time t = 0. To take into account the exposure to the gas phase during the heating and cooling periods, a correction to the anneal time is made using the method described by Killoran [106]. The exchange process is assumed to occur uniformly over the sample surface, whereas diffusion in the solid oxide is assumed to be fast.

For the determination of the surface exchange and diffusion coefficients along the *c*-axis direction (traverse oxygen transport measurements) we assume for our $La_2NiO_{4+\delta}$ thin film the model of an infinite solid slab extending over the region of thickness $2l$. The symmetrical solutions given by this plane sheet model, the plane sheet occupying the region $-l<z<l$, apply also to the sheet $0<z<l$ when the face z = 0 is non-permeable [105] (see Figure 5.3). In our case the impermeable surface corresponds to the film-substrate interface, through which no oxygen diffusion occurs.

The boundary conditions are related to the rate of transfer of the diffusing species across the surface. The assumption made is that the rate of exchange is proportional

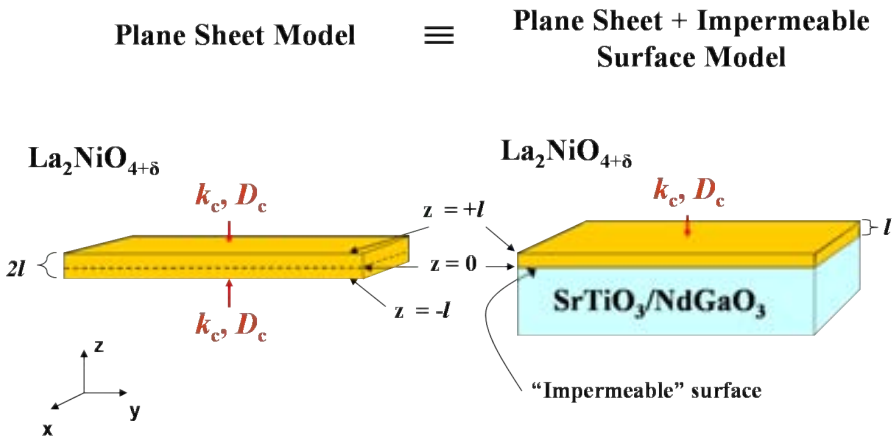

Figure 5.3: Representation of a La_2NiO_4 film of thickness l grown on a STO/NGO substrate and its plane sheet model equivalent of a La_2NiO_4 film of thickness $2l$.

to the difference between the concentration in the gas and the concentration in the surface at any time. This boundary condition is expressed by:

$$-D^* \frac{\partial c^*(l,t)}{\partial z} = k^* \left[c_g^* - c^*(l,t)\right] \tag{5.3}$$

The initial and the second boundary conditions are:

$$c^*(z,0) = c_{bg}^* \tag{5.4}$$

$$\frac{\partial c^*(0,t)}{\partial z} = 0 \tag{5.5}$$

where c^* is the isotopic concentration at depth z, c_{bg}^* is the background isotopic concentration, c_g^* is the concentration of ^{18}O in the gas phase, k^* is the tracer surface exchange coefficient and D^* is the self-diffusion coefficient.

The solution to the diffusion equation given by Crank [105] for a plane sheet is as follows:

$$\frac{c^* - c_{bg}^*}{c_g^* - c_{bg}^*} = 1 - \sum_{n=1}^{\infty} \frac{2Lcos(\beta_n z/l)exp(-\beta_n^2 D^* t/l^2)}{cos\beta_n(\beta_n^2 + L^2 + L)} \tag{5.6}$$

where β_n (n=1, 2, ...) are the nonnegative roots of $\beta \tan \beta = L$, $L = lk^*/D^*$.

The sample configuration and an outline of the ^{18}O diffusion profiles for the traverse and longitudinal oxygen tracer transport measurements are shown in Figure 5.4.

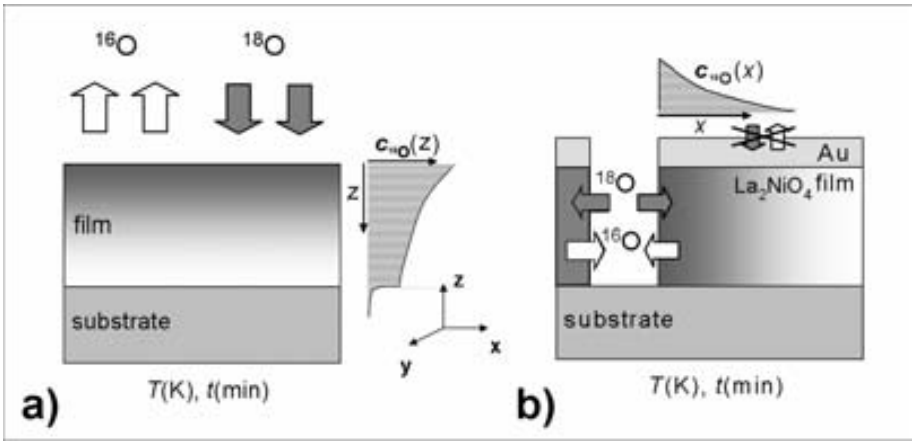

Figure 5.4: Sample configuration for a) traverse and b) longitudinal oxygen tracer transport measurements.

In Figure 5.5 we can observe the shape of the ^{18}O concentration profile which results from the exposure of the surface of a 400 nm film to a ^{18}O gas concentration of 24.9% during different time periods up to 30 min (1800 s). For the diffusion simulation we have used the COMSOL Multiphysics modeling package and defined the dimensions and boundary conditions of our thin films. The profiles shown in Figure 5.5 have been obtained for a surface exchange coefficient of $k_c^* = 1.34 \text{ x } 10^{-9}$, a c-axis diffusion coefficient of $D_c^* = 1.69 \text{ x } 10^{-12}$ and an initial ^{18}O isotopic fraction of 0.002. These simulations allow us to predict the length and shape of the diffusion profiles for estimated values of k^* and D^* and to prove the validity of the solutions of the diffusion equations used for our sample configuration.

As previously explained in Section 3.4.3 in page 54, for the determination of the surface exchange and diffusion coefficients along the a-b plane in the tracer experiment (longitudinal oxygen transport measurements), a dense and uniform Au thin film with a 1 to 2 nm grain size was sputtered to cover the $La_2NiO_{4+\delta}$ film surface (see Figure 5.4.b). This film prevented oxygen exchange from the substrate surface. A trench was defined through the gold and through the $La_2NiO_{4+\delta}$ film, so

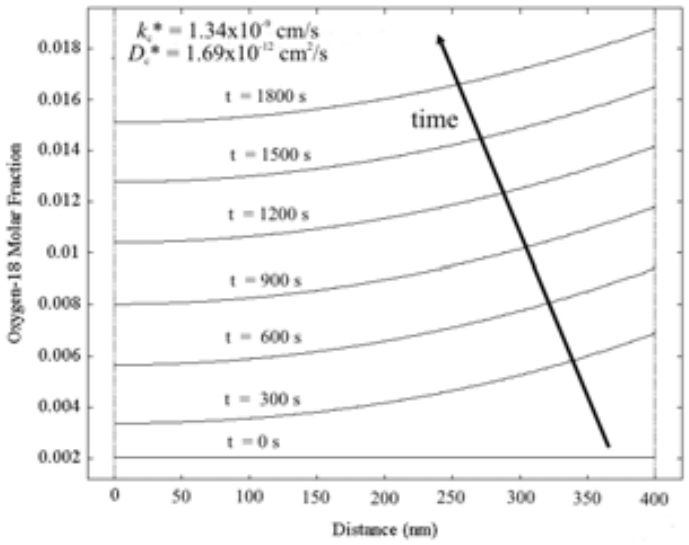

Figure 5.5: c- axis ^{18}O concentration profile for a 400 nm film exposed to a ^{18}O gas concentration of 24.9% during 1800 s with $k_c^* = 1.34 \times 10^{-9}$ cm/s and $D_c^* = 1.69 \times 10^{-9}$ cm^2/s.

that the lateral edge of the studied thin film was exposed to the surrounding gas to allow the exchange with the ^{18}O enriched exchange gas phase and thus ensuring the diffusion of the ^{18}O species only along the a-b planes of the $La_2NiO_{4+\delta}$ film. In this case the model of a semi-infinite plane along the a-b plane (x direction) was applied for solving the diffusion equation, in which x = 0 is the surface of the opened lateral edge. For the exchange and diffusion along the a-b plane, the initial and boundary conditions are:

$$- D^*\left(\frac{\partial c^*(0,t)}{\partial x}\right) = k^*\left[c_g^* - c^*(0,t)\right] \tag{5.7}$$

$$c^*(x,0) = c_{bg}^* \tag{5.8}$$

The full solution to the diffusion equation for one-dimensional diffusion into a semi-infinite medium has been given by Crank [105]:

$$c'(x) = \frac{c^*(x) - c_{bg}^*}{c_g^* - c_{bg}^*} \tag{5.9}$$

$$c'(x) = erfc\frac{x}{2\sqrt{D^*t}} - exp(hx + h^2D^*t)erfc(\frac{x}{2\sqrt{D^*t} + h\sqrt{D^*t}}) \quad (5.10)$$

The parameter h is given by $h = k^*/D^*$ and c'(x) is the normalized oxygen isotopic fraction.

In Figure 5.6 we can observe the shape of the ^{18}O concentration profile which results from the exposure of a lateral open surface of a 400 nm film to a ^{18}O gas concentration of 24.9% during different time periods up to 30 min (1800 s) while the top surface is insulating. The COMSOL Multiphysics diffusion simulation was done for k^*_{ab} = 9.05 x 10^{-8} cm/s, D^*_{ab} = 2.32 x 10^{-9} cm^2/s and an initial ^{18}O isotopic fraction of 0.002.

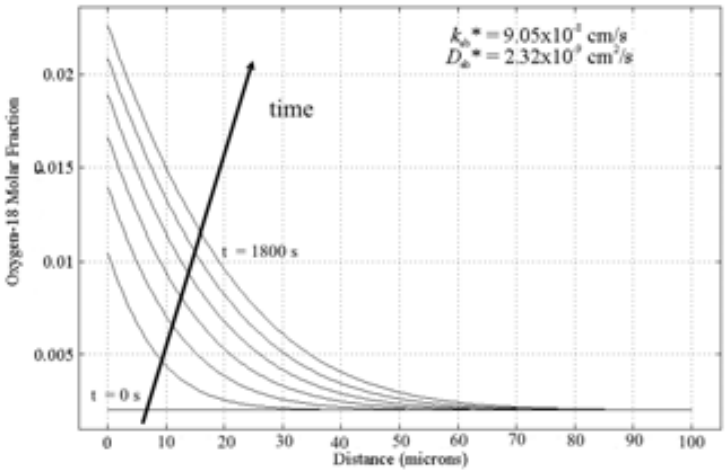

Figure 5.6: *a-b* plane ^{18}O concentration profile for a 400 nm film exposed to a ^{18}O gas concentration of 24.9% during 1800 s with k^*_{ab} = 9.05 x 10^{-8} cm/s and D^*_{ab} = 2.32 x 10^{-9} cm^2/s.

5.2.2 Results of the Isotope Exchange Measurements

Oxygen isotope exchange experiments were performed at different temperatures (approximately 340, 380, 430, 510 and 600 °C) on *c*-axis oriented epitaxial $La_2NiO_{4+\delta}$

thin films deposited on 5x5 mm^2 (110) NGO and (001) STO substrates. The deposition parameters and the structural, microstructural and morphological characterization of the $La_2NiO_{4+\delta}$ thin films have been previously described in Chapter 4. In order to study the effect of the strain induced by the mismatch between the film and the substrate on the oxygen diffusion, films of different thickness deposited on the two substrates (which induce strain in opposite directions) have been measured. The experimental isotope exchange depth profile (IEDP) equipment and the measurement procedure have been described in Section 3.4.3 in page 54.

The in- and out-of-plane cell parameters have been measured for the $La_2NiO_{4+\delta}$ films from XRD reciprocal space maps before and after the oxygen exchange in order to detect possible variations, following the methodology described in Section 4.4. The *a*, *b* and *c* cell parameters for as-deposited films with different thickness and for films after the IEDP (isotope exchange depth profile) measurements are shown in Figures 5.7 and 5.8.

The variation of the $La_2NiO_{4+\delta}$ unit cell parameters with thickness after the IEDP measurements is quite similar to that before the measurements and is related to the strain effect induced by the film/substrate mismatch. On NGO, the $La_2NiO_{4+\delta}$ *a* and *b* parameters increase, Figure 5.7, and the $La_2NiO_{4+\delta}$ *c*-parameter value decreases with thickness, Figure 5.8, due to the compressive stress in the *a*-*b* plane induced by the film/substrate mismatch, while the opposite behavior is observed for the $La_2NiO_{4+\delta}$ cell parameters on STO due to the tensile stress. Thin films are strained and thicker films tend to a relaxed state. The *c*-parameters are lower after the IEDP measurements for all the films of different thickness, and specially for those deposited on NGO. This decrease is a result of the oxygen loss, occurred to reach equilibrium during the anneal time at each temperature. For the films deposited on NGO the decrease in the out-of-plane cell parameter, *c*, is accompanied by a slight increase of the in-plane cell parameters, *a* and *b*. For the films deposited on STO the change in-plane parameter value is not as clear.

Transversal (*c*-axis) IEDP measurements

In Figure 5.9 an ^{18}O normalized isotopic fraction depth profile from a 370 nm thick $La_2NiO_{4+\delta}$ film deposited on NGO is shown. The ^{18}O concentration was measured

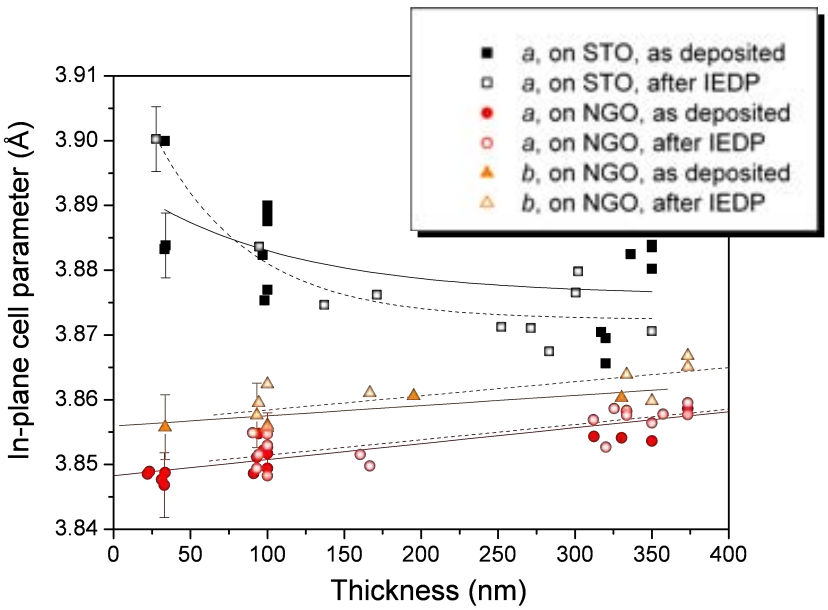

Figure 5.7: Variation of the $La_2NiO_{4+\delta}$ in-plane cell parameters (a for films on STO: black; a for films on NGO: red; and b for films on NGO: orange) with thickness before (closed squares, solid lines) and after (open squares, dashed lines) IEDP measurements.

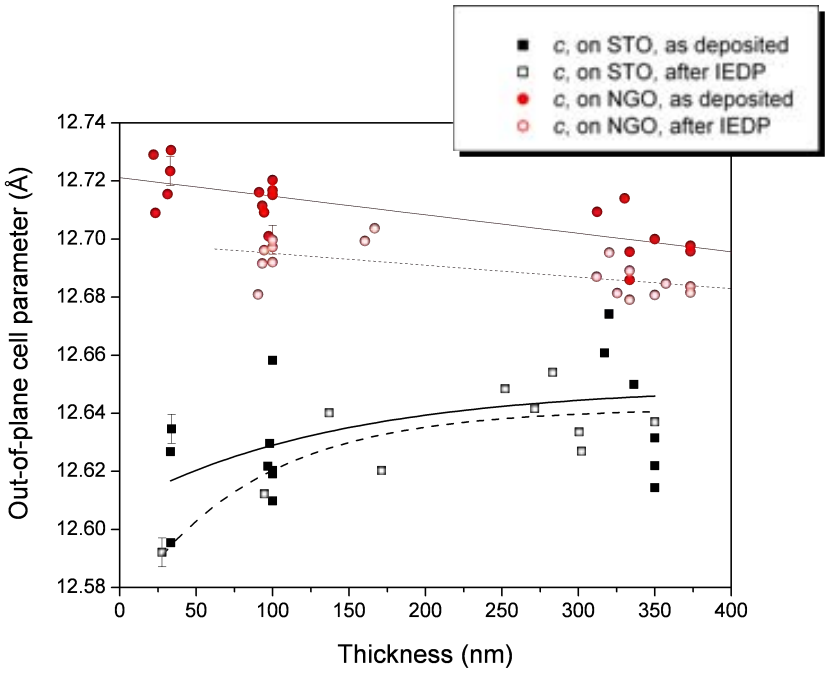

Figure 5.8: Variation of the $La_2NiO_{4+\delta}$ out-of-plane cell parameter (for films on STO: black and for films on NGO: red) with thickness before (closed squares, solid lines) and after (open squares, dashed lines) IEDP measurements.

in a region near the centre of a 5x5 mm sample using the Atomika SIMS equipment with a nitrogen 1.25 keV primary ion sputtering. The film had been exchanged in enriched ^{18}O for 30 minutes at a temperature of approximately 380 °C. It is observed that the ^{18}O enrichment remains almost constant through the thickness of the film but decays abruptly when reaching the non-oxygen-permeable substrate interface. We have to mention that in the substrate the ^{18}O fraction corresponds to the isotopic background values or natural abundance of ^{18}O. From the abrupt decay and the background values measured in the substrate, we can assess that there is no ^{18}O diffusion from the film into the substrate and that in such case the concentration data in the film can be fitted with the plane sheet model. To select the values to be fitted, first we discard the concentrations corresponding to the first nanometres of the profile, which, as can be seen in Figure 5.9, are lower than through the rest of the film. This phenomenon could be due to surface contaminants, to the adsorption of oxygen (as O_2, H_2O or CO_2) on the surface or, less likely, to outward diffusion at room temperature during the time lapse from the ^{18}O exchange to the SIMS measurement.

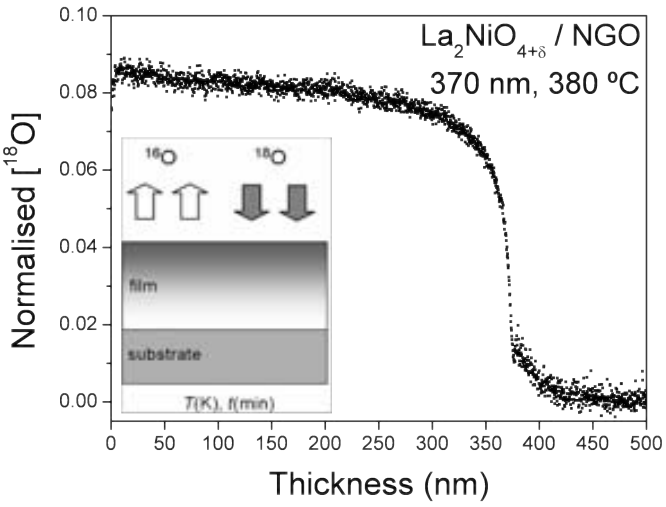

Figure 5.9: Normalized isotope fraction along the c-axis direction of a $La_2NiO_{4+\delta}$ film of 370 nm thickness deposited on NGO and exchanged at 380 °C during 30 min.

The interface between the film and the substrate was defined as the inflexion point of the total oxygen secondary ion intensity curve. The width of the interfacial zone is affected by the roughening of the crater base due to the sputtering produced by the nitrogen beam and by the intrinsic roughness of the surface of the $La_2NiO_{4+\delta}$ film. As the penetration of the N_2^+ ion beam reaches several nanometres, a mixture of oxygen ions from the film and from the substrate will be measured when reaching this interfacial zone. The penetration depth of the incident primary ion beam, with an impact energy of 625 eV per N atom, calculated with the SRIM modelling program [118], is about 4 nm for $La_2NiO_{4+\delta}$, NGO and STO. The films surface was quite flat for thin films (RMS = 3-6 nm) but RMS values increase up to 35-55 nm for thick films (approximately 350 nm). Therefore, the ^{18}O isotopic fraction values in the region very close to the interface (some nanometres for the thin films and approximately 25 nm for the thicker films) was discarded for the fitting (see Figure 5.10).

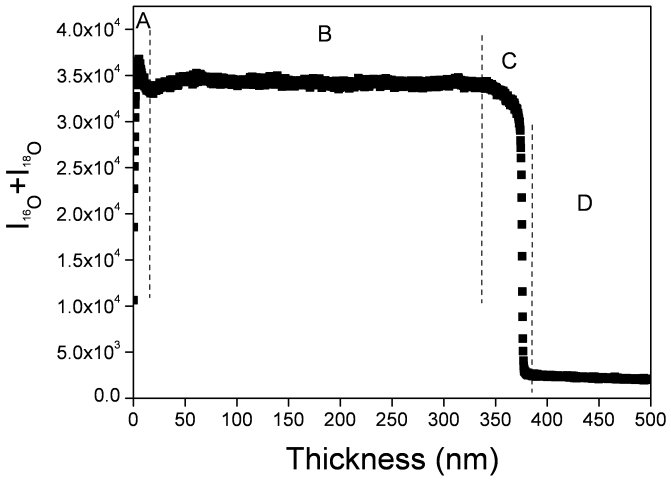

Figure 5.10: Total oxygen secondary ion intensity of a $La_2NiO_{4+\delta}$ film of 370 nm thickness analyzed by SIMS depth profile: A) Pre-equilibrium region; B) Steady state sputtering in the $La_2NiO_{4+\delta}$ film; C) Interface region; D) Steady state sputtering in the STO or NGO film.

The oxygen concentration profiles were determined using the analytical solutions to the diffusion equation for a plane sheet model (Equation 5.6) and fitting by least squares numerical fit. The thinnest films measured transversely were of approximately 100 nm, to ensure the possible observation of a diffusion profile through the thickness. As a first approximation, D_c^* is assumed to be constant along the depth. The analysis takes into account the time that the sample has been exposed to the gas phase during heating and cooling steps [106]. In the case of these *c*-axis profiles, the activation energy corresponding to the surface exchange reaction was used for the exchanged time correction, since this is the rate-limiting step for oxygen transport in these thin films. In Figure 5.11 we show the same concentration profile from Figure 5.9, for the 370 nm thick film, but in this case we have defined the interface with the substrate at z = 0, in order to use the appropiate fitting equations. As can be seen, the measured ^{18}O isotopic fraction values in a region of approximately 100 nm from the substrate interface do not fit the tendency of a normal diffusion profile (red line). For this first fitting, the values in this region were not taken into account, and the D_c^* (constant through the whole film thickness) and k_c^* values were obtained as $D_c^* = 2.10 \text{ x } 10^{-12}$ cm^2/s and $k^* = 1.40 \text{ x } 10^{-9}$ cm/s . The possibility that this curvature comes exclusively from the oxygen mixing at the interface region has been discarded because the ^{18}O isotopic fraction decrease starts considerably before the (^{18}O+ ^{16}O) secondary ion intensity decrease at the interface (see Figure 5.10).

For a better approximation to the real diffusion data a new model was developed, in which the film was divided into two regions with different D_c^* values. In the region close to the film surface we assume a constant D_c^* ($D_{c_1}^*$), while near the substrate we assume D_c^* to vary linearly with depth from $D_{c_1}^*$ to $D_{c_2}^*$. $D_{c_2}^*$ corresponds to the diffusivity value of film material in close proximity to the substrate. The ^{18}O concentration in this region is clearly influenced by the mixing due to sputtering and roughness, as previously explained, so this value has no real physical meaning and is a fictitious parameter which helps to fit the concentration curves. Starting from the previously derived D_c^* and k_c^* values (from the model assuming D_c^* to be constant), new k_c^*, $D_{c_1}^*$, $D_{c_2}^*$ and F (fraction of the film thickness with D_c^* variable) values are obtained from the best fit to the experimental data: $k_c^* = 1.40 \text{ x } 10^{-9}$ cm/s , $D_{c_1}^* = 2.10 \text{ x } 10^{-12}$ cm^2/s , $D_{c_2}^* = 1.10 \text{ x } 10^{-13}$ cm^2/s and F = 0.35. We estimate the

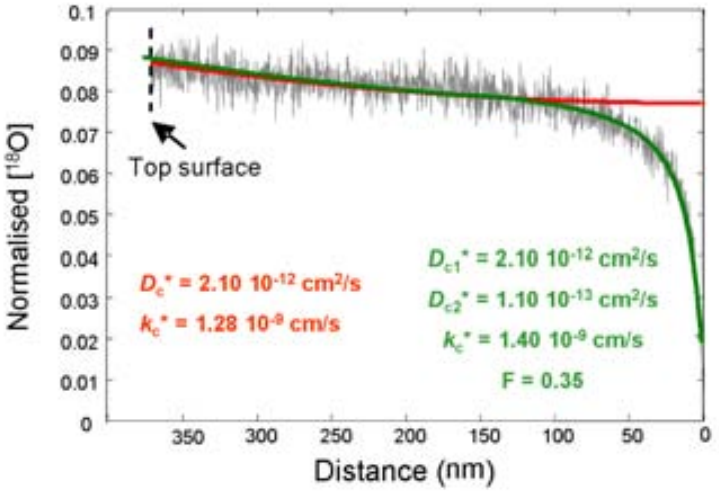

Figure 5.11: Normalized isotope fraction of a $La_2NiO_{4+\delta}$ film of 370 nm thickness analyzed by IEDP with the fitted concentration profile for Crank's diffusion equation with constant D_c^* (red) and with variable D_c^* (green) after exposure at 380 °C during 30 min.

uncertainty on the k_c^* data to be 20% and on the $D_{c_1}^*$ data to be approximately 15% by using this two-zone model. In summary, the model considers the existence of two different regions in the $La_2NiO_{4+\delta}$ film: a region in which the film is more relaxed (constant D_c^*) and a region in which the film is "stressed" (D^* variable) due to the mismatch of the cell parameters between the substrate and the film. We have seen from the fitting that this new two-zone model does not affect the value of D_c^* of the zone closer to the film surface, while the value of k_c^* decreases slightly in all cases. In Figure 5.12 the variation of D_c^* along the film thickness for these fitting values is shown, and the resulting ^{18}O isotopic fraction profile is shown as a curved line (green) in Figure 5.11. It is clear that this new model with two different regions provides a better fit for the whole thickness. We have chosen this model as being the simplest one that successfully fits the experimental data, although another model, in which the diffusivity values vary through the whole thickness of the $La_2NiO_{4+\delta}$ film, would probably be more realistic. In this case the diffusivity curve should closely follow the shape of the two-region-diffusivity of Figure 5.12.

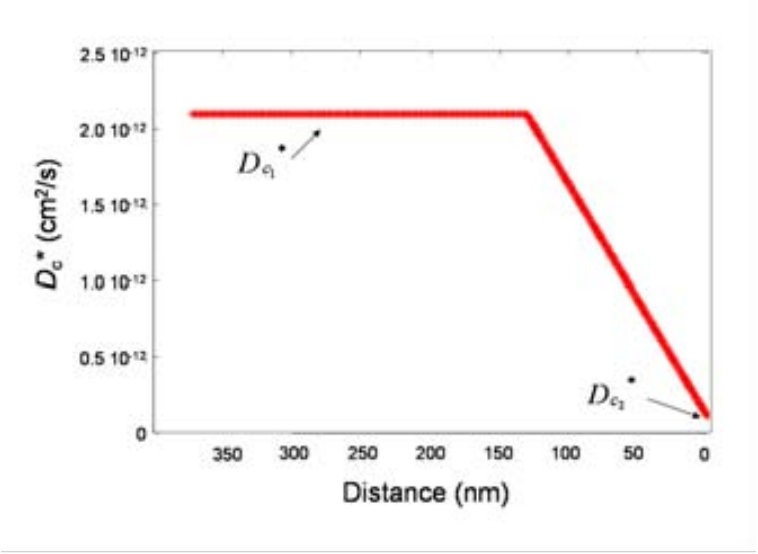

Figure 5.12: Diffusivity change through the $La_2NiO_{4+\delta}$ film of 370 nm thickness calculated by fitting Crank's diffusion equation with variable D_c^*.

The obtained D_c^* and k_c^* values will be discussed and compared with the longitudinal D_{ab}^* and k_{ab}^*, after the explanation of the longitudinal (a-b plane) IEDP measurements.

Longitudinal (a-b plane) IEDP measurements

In the longitudinal transport experiments several lithographic techniques were used to define the open windows for the gas phase exposure. First, we used a shadow mask (vinyls in a solvent mixture containing xilene) to cover half of the surface of the sample. Then, the sample was sputtered with Au at room temperature. Finally the mask was carefully lifted off with acetone. But the removal of the mask left some holes in the Au protecting layer in the regions where there was poorer adhesion to the film and produced undesired paths for oxygen in-diffusion. An alternative way to produce an open window was to cover the full film surface by a thin sputtered Au layer and remove a part of it to open controlled window surfaces. When using ion etching by FIB to open a 5 μm wide trench through the gold and film layer no longitudinal ^{18}O penetration was observed after gas exposure. This was thought to

be caused by the surface modification of the $La_2NiO_{4+\delta}$ film material in the open surface near the trench due to the Ga^+ bombardment, which could have hindered any oxygen exchange. The most reproducible results were obtained by a simple line scratch through the film with a scalpel, which defined a clean break in the gold diffusion barrier of about 10 μm wide and penetrating down into the substrate. In Figure 5.13 pictures taken with the FIB-SIMS instrument show a focused-ion-beam defined and a scalpel defined trench in $La_2NiO_{4+\delta}$ thin films.

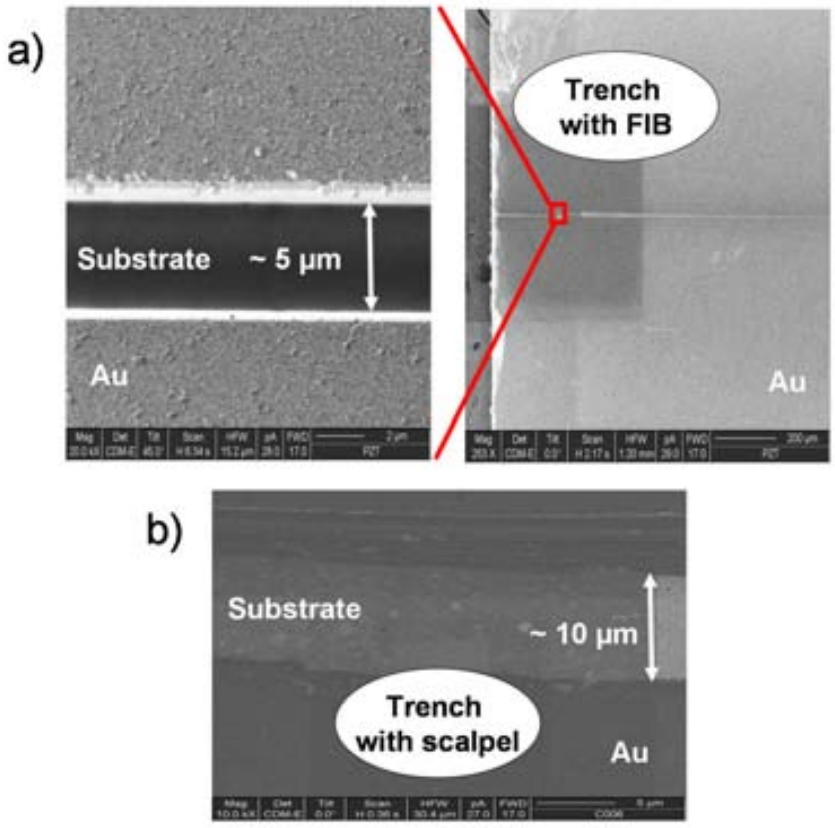

Figure 5.13: a) FIB defined and b) Scalpel defined trench in $La_2NiO_{4+\delta}$ thin films for the longitudinal transport experiments.

Figure 5.14 shows a concentration profile obtained by the Atomika SIMS instrument in the linescan mode when the nitrogen milling had etched the Au cap layer

down into the film as a function of the distance from the opened trench in the direction perpendicular to the same. The profile corresponds to a 170 nm $La_2NiO_{4+\delta}$ thin film deposited on STO, which had been exchanged for 30 min at a temperature of 420 °C. In this case, to calculate the exact duration of the anneal time by Killoran's method [106], the activation energy corresponding to the diffusion process was used. The longitudinal concentration profiles were analyzed using a semi-infinite plane solution of the diffusion equation (Equation 5.10) and the values of $D^*_{ab} = 4.56 \text{ x } 10^{-9}$ cm^2/s and $k^*_{ab} = 1.60 \text{ x } 10^{-7}$ cm^2/s were extracted for the best fit. We estimate the uncertainty on the k^*_{ab} and on the D^*_{ab} data to be approximately 10%.

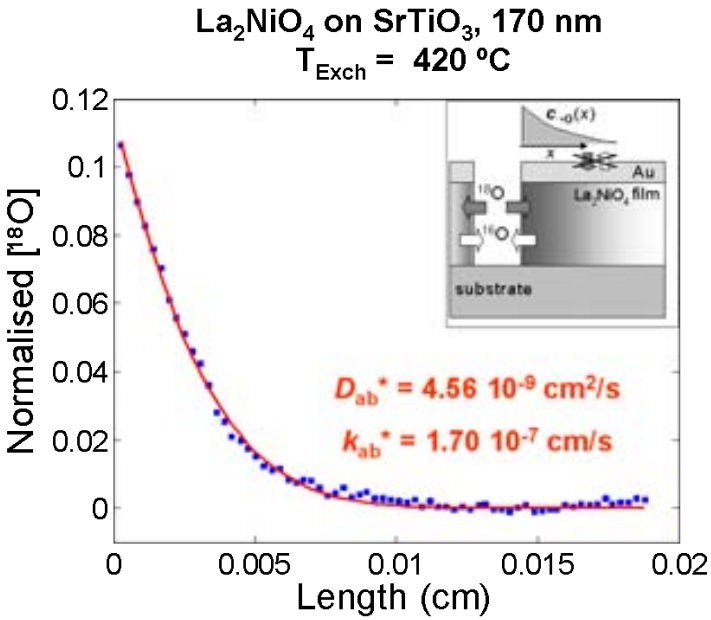

Figure 5.14: Normalized isotopic fraction profile along the *a*-*b* plane of a 170 nm $La_2NiO_{4+\delta}$ thin film deposited on STO, exchanged at 420 °C.

Diffusion Coefficients

Thickness dependence of the diffusion coefficients In Figure 5.15 the variation of the D^*_c values through the depth for films of different thickness deposited on both substrates and ^{18}O exchanged at approximately 430 °C are plotted. We can

observe that, for the thin films measured in the transversal direction (100-150 nm), the thickness with variable D_c^* is small enough to be considered associated with the interfacial mixing of oxygen from the $La_2NiO_{4+\delta}$ film and the substrate. In contrast, for the thick films (300-400 nm) we can clearly distinguish two regions with D_c^* constant and D_c^* variable, respectively. This behavior could be related to the existence of a certain thickness up to which the film is totally strained, which would induce a constant and low value of diffusivity. Generally, as the film grows, a stress relief mechanism appears (possibly by the formation of dislocations) giving rise to a more stressed zone with D_c^* variable close to the substrate and a more relaxed zone (with a higher and constant value of diffusivity) close to the film surface. The difference in the value of D_c^* from one sample to another could be related to the difference in the cell parameters, in the strain and in the δ value of the $La_2NiO_{4+\delta}$ films. Firstly, the oxygen atoms of the stressed cell possibly have a lower mobility than those of a relaxed cell. Secondly, even if we are not able to measure it, the hyperstoichiometric oxygen in this structure is expected to vary with the value of the $La_2NiO_{4+\delta}$ cell parameters, as occurs in $La_2NiO_{4+\delta}$ bulk samples. Due to the effect of strain, the incorporation of the excess oxygen could be hindered, especially for the thinnest films and for the region closest to the substrate for the thick films. The decrease in δ (oxygen hyperstoichiometry) in the $La_2NiO_{4+\delta}$ films could lead to a decrease of the oxygen mobility and, therefore, in the diffusion coefficient, as the ionic oxygen mobility increases with δ [32].

As the D_c^* varies through the zone close to the substrate, it is quite difficult to compare the values in that region and we have limited our comparison of the $D_{c_1}^*$ values. In Figure 5.16 the *c*-axis diffusivity in the zone close to the film surface ($D_{c_1}^*$) and the *a*-*b* plane diffusivity (D_{ab}^*) extracted from the longitudinal measurements are plotted versus the film thickness for $La_2NiO_{4+\delta}$ epitaxial films on STO and NGO substrates ^{18}O exchanged at approximately 430 °C. As expected, the diffusion is anisotropic, with values along the *c*-axis three orders of magnitude lower than that along the *a*-*b* plane. It is observed that for both substrates the $D_{c_1}^*$ and D_{ab}^* values increase with film thickness. The *a*-*b* diffusion coefficient was measured, in all cases, at the top part of the film, so this result also corresponds to the zone of the film close to the surface. For $La_2NiO_{4+\delta}$ films deposited on STO the *a*-*b* plane diffusion seems

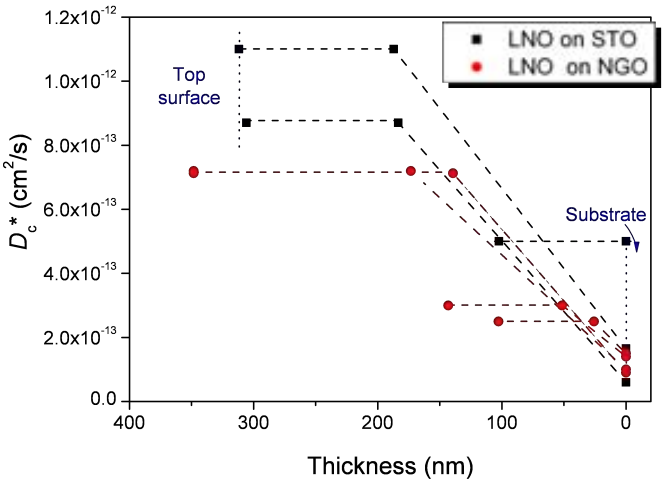

Figure 5.15: *c*-axis diffusivity values through the depth for different thickness $La_2NiO_{4+\delta}$ films on STO and on NGO exchanged at approximately 430 °C.

to increase with thickness up to 200 nm, and then remains approximately constant with a value of 1.5 x 10^{-9} cm^2/s, behavior which is similar to that of the $La_2NiO_{4+\delta}$ cell parameters for the films deposited on this substrate, which do not vary much in the high thickness range. It seems that both compressive and tensile strain lead to a decrease in the oxygen mobility and/or the number of mobile species, which leads to a decrease in the diffusivity.

Temperature dependence of the diffusion coefficients In Figure 5.17 we can observe the Arrhenius representation of the diffusion coefficients in the *c*-axis direction (from the zone closer to the film surface) and in the *a*-*b* plane for $La_2NiO_{4+\delta}$ epitaxial films on STO and NGO substrates. For the films deposited on STO at 600 °C and on both substrates at 510 °C it was not possible to extract a diffusivity value for the *c*-axis, as the diffusion was so fast that the resulting diffusion profile was flat. This means that, even if we do not know the exact value of the diffusivity at high temperatures, its value is certainly higher than 6 x 10^{-12} cm^2/s, as for lower D_c^* values we would observe a curved concentration profile instead of the observed flat

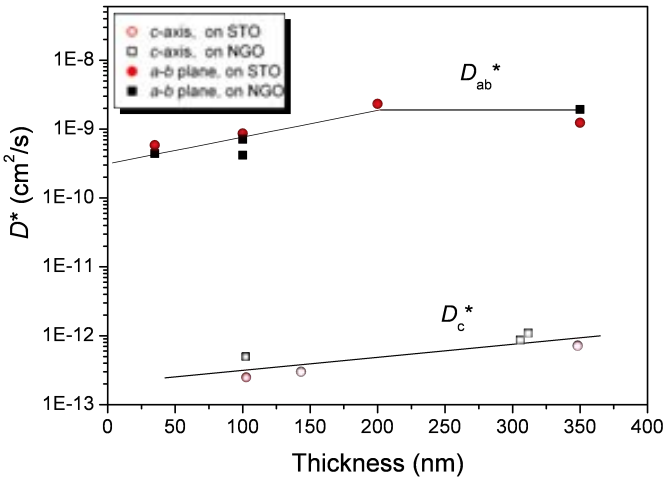

Figure 5.16: Variation of the *c*-axis diffusivity in the zone close to the film surface ($D^*_{c_1}$) and of the *a*-*b* plane diffusivity (D^*_{ab}) with thickness for $La_2NiO_{4+\delta}$ films deposited on STO and on NGO and exchanged at approximately 430 °C.

one.

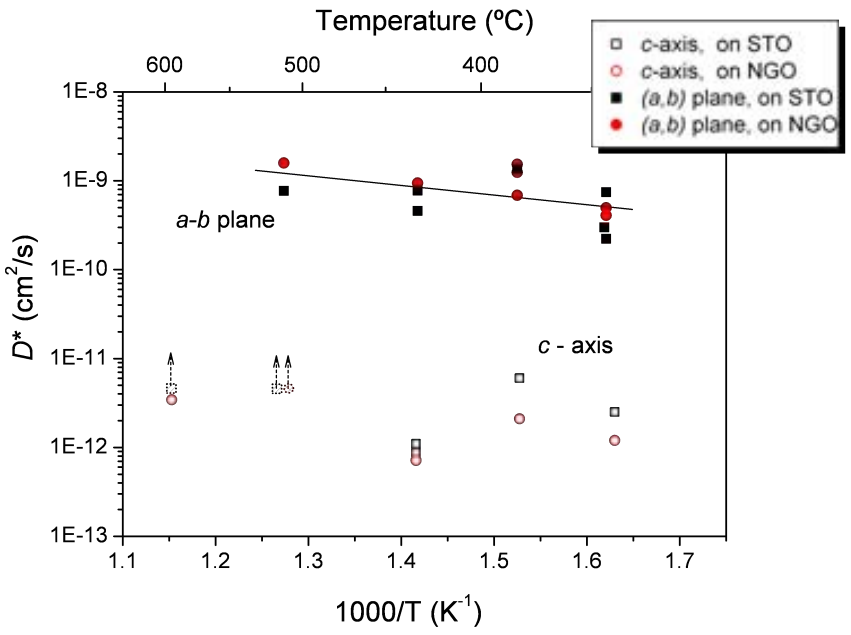

Figure 5.17: Arrhenius plot of the c-axis diffusivity in the "relaxed" zone ($D^*_{c_1}$) and of the a-b plane diffusivity (D^*_{ab}) for $La_2NiO_{4+\delta}$ films deposited on STO and on NGO.

As expected, the diffusion along the c-axis is two orders of magnitude lower than that along the a-b plane, and, as a general trend, D^*_c and D^*_{ab} obtained from thin $La_2NiO_{4+\delta}$ films slightly increase with temperature. The extracted value for the activation energy in the a-b plane is 0.19 eV.

In order to evaluate our experimental results, we plot in Figure 5.18 along with the measured values, data from the literature corresponding to $La_2NiO_{4+\delta}$ single crystals and dense ceramics [24]. It is worth mentioning here that, due to the thinness of our layers, a low exchange temperature is required to obtain tracer oxygen diffusion profiles. Thus the exchange temperature range in which we have measured our epitaxial thin films is low compared with the temperature range of measurement for single crystals carried out by Bassat et al. [24]. The D^*_{ab} values measured by Bassat et al. [24] are higher (approximately 1.5 x 10^{-8} cm^2/s at 460 °C) than those

of the thin films (approximately 1.5 x 10^{-9} cm^2/s at 510 °C), while the activation energy value of the process is higher (0.88 eV for single crystals and 0.19 eV for thin films). We have measured D_c^* values 3 orders of magnitude lower (approximately 3.5 x 10^{-12} cm^2/s at 600 °C) than the values observed in single crystals (approximately 3.5 x 10^{-9} cm^2/s at 600 °C). The D_{ab}^* value in single crystal at 460 °C (approximately 1.5 x 10^{-9} cm^2/s) does not line up with the data from the high temperature range. Bassat et al. suggested a possible change in the activation energy around 500 °C giving rise to a similar activation energy in the *a*-*b* plane and along the [001] axis at low temperature. They proposed a mechanism involving the migration of O'_i species via oxygen vacancies to occur, which contribution to the *a*-*b* plane diffusion becomes only important at low temperatures. For our measurements we have extracted an activation energy of 0.19 eV for the diffusion along the *a*-*b* plane, very close to that measured by Bassat et al. (0.22 eV) for the *c*-axis diffusion. This supports the hypothesis that at low temperatures a mechanism involving the diffusion of O'_i species via oxygen vacancies might occur in this direction. The concentration of O'_i species (much smaller than δ) leads to a low D^* value, but with a high mobility thanks to its small size and weak charge. Therefore the activation energy for this mechanism should be smaller than that in which the ionic conductivity involves mainly O^{2-} species.

Kharton et al. [27, 28] have already reported a different oxygen transport mechanism as a function of temperature on $La_2NiO_{4+\delta}$ based ceramics. The two different behaviors were qualitatively interpreted in terms of the existence of two contributions to the total ionic conductivity of the nickelates: ionic conduction by a vacancy mechanism through the perovskite layers along with a mechanism based on the interstitial oxygen migration. The activation energy of this last mechanism is assumed to be higher than that based on transport through vacancies. The relative importance of one or other mechanism will thus be determined by analyzing the global activation energy measured. The relative role of oxygen interstitial migration increases with increasing temperature, while the role of oxygen vacancy diffusion in the perovskite layers increases when temperature decreases [27, 28]. At the same time we cannot discard the influence of the stress or of the oxygen content intrinsic to the differences in structure of the $La_2NiO_{4+\delta}$ thin films in comparison to $La_2NiO_{4+\delta}$ single crystals

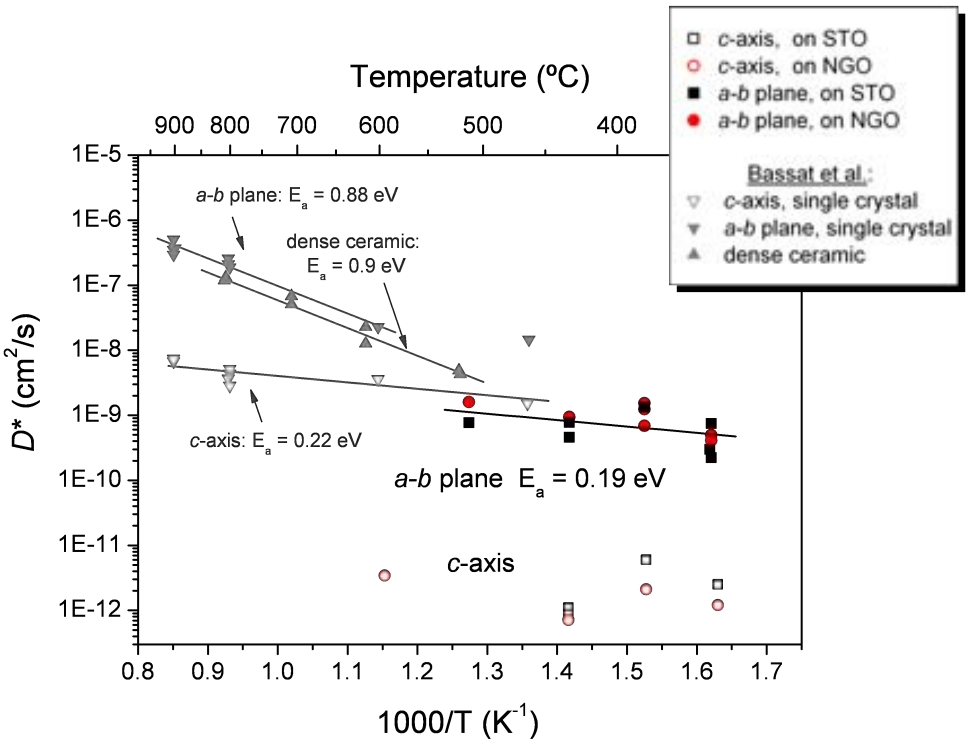

Figure 5.18: Arrhenius plot of the c-axis diffusivity in the "relaxed" zone ($D^*_{c_1}$) and of the a-b plane diffusivity (D^*_{ab}) for $La_2NiO_{4+\delta}$ films deposited on STO and on NGO and comparison with literature data for single crystals and dense ceramic [24].

or bulk material.

Surface Exchange Coefficients

Thickness dependence of the surface exchange coefficients In Figure 5.19 the k_c^* and k_{ab}^* coefficients are plotted as a function of film thickness at 430 °C. No clear dependence of k_c^* and k_{ab}^* with the thickness is observed. k_{ab}^* (1 x 10^{-7} cm/s for films deposited on NGO and 2.5 x 10^{-7} cm/s for films deposited on STO) is two orders of magnitude higher than k_c^* (6.5 x 10^{-10} for films deposited on NGO and 1.1 x 10^{-9} cm/s for films deposited on STO) and values obtained for films deposited on STO were higher that those measured on NGO. The difference in the surface exchange coefficients in the two perpendicular directions can be explained by the theoretical calculations carried out by Read et al. [119] for $La_2NiO_{4.00}$. They have shown that the 001 suraface is terminated by Ni and O ions and, since no interstitial sites exist on this termination, the oxygen exchange reaction k_c^* is not favored on this surface. On the other hand, the interstitial oxygen sites between the LaO layers are exposed in both 100 and 110 surfaces providing active sites for the surface reaction (k_{ab}^*). The surface exchange coefficients measured for films grown on STO are generally higher than those measure on NGO. Our knowledge about the surface composition, as well as its variation with temperature, δ and strain is not deep enough to explain this difference.

Temperature dependence of the surface exchange coefficients In Figure 5.20 the tracer surface exchange coefficient along the c-axis is plotted together with the a-b plane tracer surface exchange coefficient and compared with those reported in the literature for $La_2NiO_{4+\delta}$ single crystals and dense ceramics [24]. It is worth noting that in both Figures 5.19 and 5.20 the surface exchange data have a certain degree of scatter, which is likely to be a result of uncertainties in the determination of surface concentration from the SIMS data and other error sources such as thermal history or contamination of the sample. Scatter in the surface exchange coefficients determined by SIMS has been previously found by other authors [120].

We can observe that k_c^* and k_{ab}^* increase with temperature from 5.9 x 10^{-10} cm/s at 340 °C to 5.3 x 10^{-9} cm/s at 600 °C and 1.9 x 10^{-8} cm/s at 340 °C to

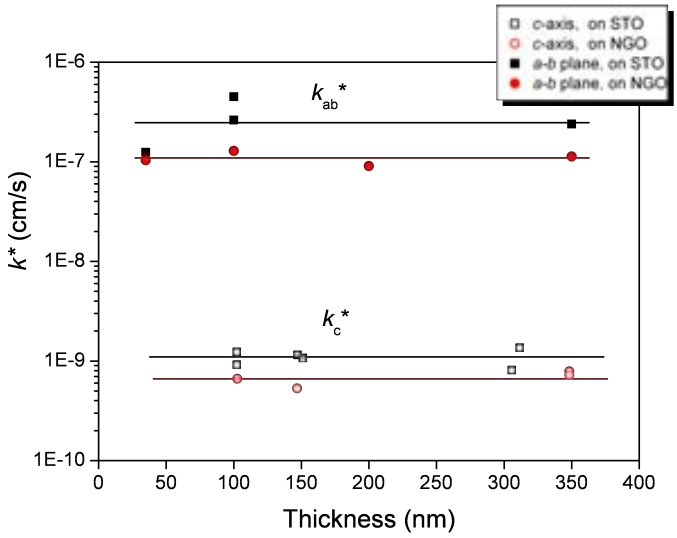

Figure 5.19: Variation of the *c*-axis and of the *a*-*b* surface exchange coefficient with thickness for $La_2NiO_{4+\delta}$ films deposited on STO and on NGO and exchanged at approximately 430 °C.

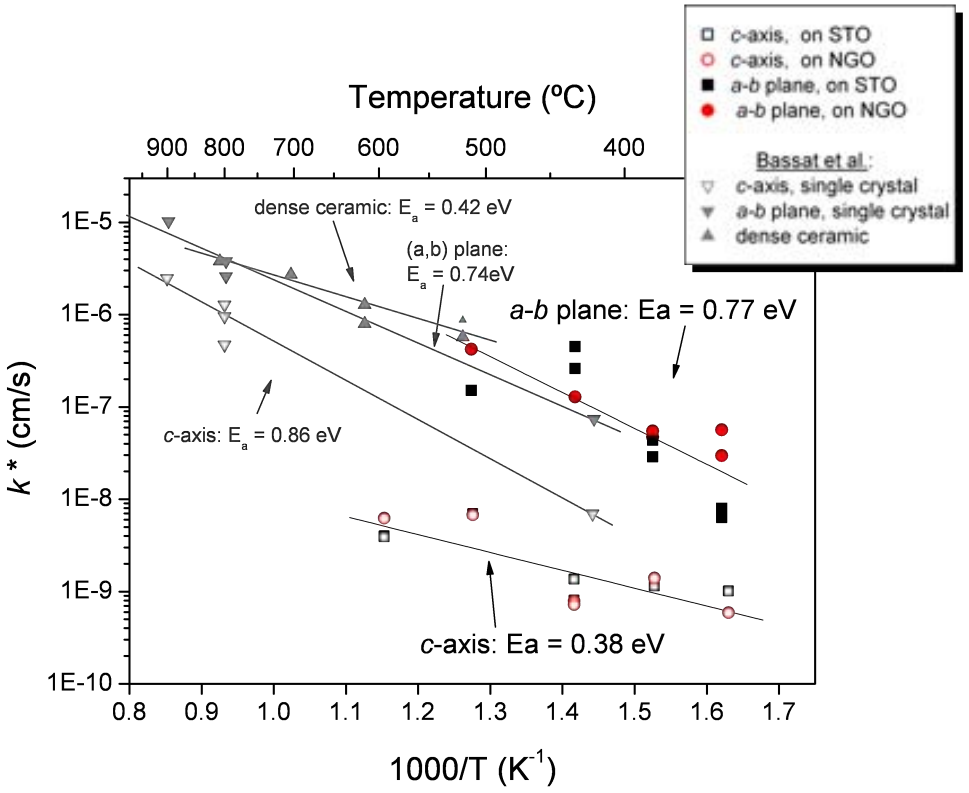

Figure 5.20: Arrhenius plot of the *c*-axis and the *a*-*b* plane tracer surface exchange coefficients for $La_2NiO_{4+\delta}$ films deposited on STO and on NGO and comparison with literature data for single crystals and dense ceramic [24].

4.6 x 10^{-7} cm/s at 510 °C, respectively. The activation energies are quite different and higher in the *a*-*b* plane (0.77 eV) than along the *c*-axis (0.38 eV). We can see that the k^*_{ab} values measured for films (5.1 x 10^{-8}-1.3 x 10^{-7} cm/s in the range 380-430 °C) are similar to those of single crystals in the same temperature range (7.5 x 10^{-8} at 420 °C), while the activation energies are almost identical (0.74 eV). However, in comparison with the literature data, the values obtained for k^* along the *c*-axis in the thin films (10^{-9}-10^{-8} cm/s) are quite smaller from that of the single crystals, although only one experimental point is given for single crystals at low temperatures. This difference does not only come from the net k^*_c value, which is between one and two orders of magnitude lower in epitaxial films, but also from the activation energy. The activation energy for k^*_c in single crystals (0.86 eV) is significantly larger than that measured from thin films (0.38 eV). As the surface exchange coefficient depends strongly on the surface state of the measured specimen it is not surprising to find differences between the single crystal and the thin films. In the same way it is possible to find differences in the activation energy of k^*_c at low and high temperatures. This difference between surface exchange coefficients and activation energies of thin films and single crystals has been previously observed by Kim et al. for $La_2NiO_{4+\delta}$ [93] and LSCO thin films [113, 121] measured by the electrical conductivity relaxation mehtod. A change in the activation energy of the surface exchange coefficient has been previously reported for oxide electrolytes having the fluorite structure (zirconia and ceria) and for LSGM ($LaGaO_3$ doped with Sr and Mg) at approximately 700 °C by Manning et al. [122] and Ishihara et al. [123], respectively, and were associated to the changes in the rate limiting step for surface oxygen exchange/incorporation.

5.3 Electrical Conductivity Relaxation Measurements

5.3.1 Electrical Conductivity Relaxation Principles

A very important diffusion coefficient for chemistry and materials science is the chemical diffusion coefficient, which characterizes the diffusion kinetics of composition changes. The change in stoichiometry of the $La_2NiO_{4+\delta}$ oxide under the driving force of a gradient of the partial pressure of oxygen would be:

$$La_2NiO_{4+\delta} + \frac{\Delta\delta}{2}O_2 \rightleftharpoons La_2NiO_{4+\delta+\Delta\delta} \tag{5.11}$$

Oxygen diffusion takes place as a result of coupled transport of O^{2-} and $2e^-$ in opposite directions due to internal gradients in the chemical potential. In contrast to the oxygen isotope experiment (Section 5.2 in page 104), this situation involves a complex interrelationship between ionic and electronic transport properties [117].

The electrical conductivity relaxation technique (ECR) offers a useful tool for determining the oxygen chemical diffusion and surface transfer coefficients in mixed ionic and electronic conductors. This method is based on the principle that a change of the nonstoichiometry δ of a specimen will be accompanied by a change of the macroscopic conductivity σ. The relaxation process follows after an abrupt change of the oxygen partial pressure and causes a change in stoichiometry of the oxide. By measuring the related change in electrical conductivity, it is possible to monitor the change in oxygen stoichiometry and thus the estimation of D_{Chem} and k_{Ex} can be obtained.

The diffusion equations for this chemical experiment are analogous to those for the tracer experiment for the c-axis (plane sheet solution). The $La_2NiO_{4+\delta}$ film is initially in chemical and thermal equilibrium with the surrounding atmosphere having a uniform bulk concentration of oxygen c(z,t) equal to c_0. At t = 0, the oxygen activity in the ambient atmosphere is changed stepwise to a value corresponding to a new equilibrium concentration c_∞ in the solid. Chemical diffusion allows the sample to adapt its stoichiometry to c_∞. The concentration at any point in the bulk at time t > 0 can be calculated from the solution of Fick's second law for diffusion in one dimension:

$$\frac{\partial c(z,t)}{\partial t} = D_{Chem}\frac{\partial^2 c(z,t)}{\partial z^2} \tag{5.12}$$

being D_{Chem} the chemical diffusion coefficient.

Conductivity relaxation models usually assume small departures from thermal equilibrium and a simple linear model for the surface exchange kinetics [124, 125]. When the change of oxygen chemical potential is small, the oxygen flux across the

solid-gas interface can be assumed linear in the difference between the initial and final oxygen concentrations at the surface [121] following Eq. 5.15.

Taking into account the surface reaction of first order, the initial and boundary conditions are:

$$c(z,0) = c_0 \tag{5.13}$$

$$\frac{\partial c(0,t)}{\partial z} = 0 \tag{5.14}$$

$$D_{Chem}\frac{\partial c(a,t)}{\partial z} = -k_{Ex}\left[c_\infty - c(l,t)\right] \tag{5.15}$$

The solution to Fick's law was solved by Crank [105]:

$$\frac{c - c_0}{c_\infty - c_0} = 1 - \sum_{n=1}^{\infty} \frac{2Lcos(\beta_n z/l)exp(-\beta_n^2 D_{Chem}t/l^2)}{cos\beta_n(\beta_n^2 + L^2 + L)} \tag{5.16}$$

where β_n $(n = 1, 2, \dots)$ are the nonnegative roots of $\beta \tan\beta = L$, $L = lk_{Ex}/D_{Chem}$.

The value D_{Chem}/k_{Ex} is a characteristic length of a material, l_d, where D_{Chem} and k_{Ex} are the bulk diffusion coefficient and surface exchange coefficient, respectively. When the thickness of the sample $l >> l_d$, the ECR process is controlled by the oxygen diffusion in the bulk. When $l << l_d$, the ECR process is controlled by the oxygen exchange reaction at the surface and Eq. 5.16 takes the simple form:

$$\frac{c - c_0}{c_\infty - c_0} = 1 - exp(-\frac{k_{Ex}t}{l}) \tag{5.17}$$

When $l \sim l_d$, the ECR process is a combination of both the bulk diffusion and the oxygen surface exchange. The characteristic length l_d for a bulk sample of $La_2NiO_{4+\delta}$ of around 0.05-0.08 cm was measured by Kim et al. [93] between 664 and 767 °C, far larger than the thickness of our films (< 350 nm = 3.5x10^{-5} cm). Therefore, the mass transport through the film is expected to be controlled by the surface exchange reaction and thus following Eq. 5.17.

In $La_2NiO_{4+\delta}$ the major defect is the interstitial oxygen $[O_i'']$ while oxygen vacancies $[V_{\ddot{O}}]$ can exist in the perovskite layer as a minor defect [28]. The local charge neutrality is expressed by:

$$[h] = 2\frac{\delta}{V_m} \tag{5.18}$$

where $[h]$ is the electron hole concentration and V_m is the molar volume of $La_2NiO_{4+\delta}$.

Since the concentration of oxygen ions is

$$c(t) = \frac{4+\delta(t)}{V_m} \tag{5.19}$$

Combining Eqs. 5.18 and 5.19 we get

$$[h] = 2[c(t) - \frac{4}{V_m}] \tag{5.20}$$

And the electronic conductivity σ_e as a function of the hole concentration can be expressed as:

$$\sigma_e = [h]\mu F \tag{5.21}$$

were μ is the hole mobility and F is the Faraday constant. Assuming μ is constant during ECR (for which small chemical potential changes are applied), from Eqs. 5.20 and 5.21 we find that the normalized conductivity $g(\mathrm{t})$ is equal to the normalized oxygen ion concentration:

$$g(t) = \frac{\sigma(t) - \sigma(0)}{\sigma(\infty) - \sigma(0)} = \frac{c(t) - c(0)}{c(\infty) - c(0)} \tag{5.22}$$

By analyzing the time response of the electrical conductivity relaxation, the surface exchange coefficient of the $La_2NiO_{4+\delta}$ thin films can be extracted.

The diffusion equation for this technique is solved assuming an instantaneous change in the oxygen partial pressure surrounding the specimen. If the time for the step change in p_{O_2} is not negligible in comparison to the conductivity change in the sample, then the relaxation profile will tend to be longer than expected [126]. The flushing behavior of the reactor volume may significantly influence the early

stage of the relaxation process. Large errors are obtained from fitting the relaxation data to the theoretical equations if this phenomenon is not properly recognized. A correction must be applied if the relaxation time approaches the flush time of the reactor volume. Den Otter et al. [127] presented the equation which describes the transient conductivity taking into account the finite flush time (τ_f) of the reactor:

$$g(t) = 1 - exp(-\frac{t}{\tau_f}) - \sum_{n=1}^{\infty} A_n \frac{\tau_n}{\tau_n - \tau_f}[exp(-\frac{t}{\tau_n}) - exp(-\frac{t}{\tau_n})] \tag{5.23}$$

where

$$A_n = \frac{2Lcos(\beta_n z/l)}{cos\beta_n(\beta_n^2 + L^2 + L)} \tag{5.24}$$

and

$$\tau_n = \frac{l^2}{\beta_n^2 D_{Chem}} \tag{5.25}$$

In the case of thin films, in which the relaxation is rate limited by the surface reaction, Eq. 5.23 can be simplified as:

$$g(t) = 1 - exp(-\frac{t}{\tau_f}) - \frac{\tau}{\tau - \tau_f}[exp(-\frac{t}{\tau}) - exp(-\frac{t}{\tau_f})] \tag{5.26}$$

5.3.2 Results of the ECR Measurements

Electrical conductivity relaxation experiments were performed on two *c*-axis oriented epitaxial $La_2NiO_{4+\delta}$ thin films, 50 and 335 nm thick, deposited on a 5x5 mm^2 (110) NGO and (001) STO substrates, respectively. The deposition parameters and the structural, microstructural and morphological characterization of the $La_2NiO_{4+\delta}$ thin films have been previously described in Chapter 4.

The details about the ECR measurement equipment have been given in Sections 3.4.1 and 3.4.2. In order to measure the flushing characteristics of the reactor volume, the oxygen pressure before and after the exchange furnace was monitored by using oxygen sensors. The oxygen pressure changes were measured and fitted to an exponential equation, from which τ_f was extracted. The extracted τ_f had a value between 60 and 80 s, depending on the temperature. Another oxygen sensor was

placed before the exchanged furnace and its response to the oxygen pressure changes was also measured, to make sure that the stabilization period was effectively due to the flush time and not to the intrinsic response time of the zirconia sensor.

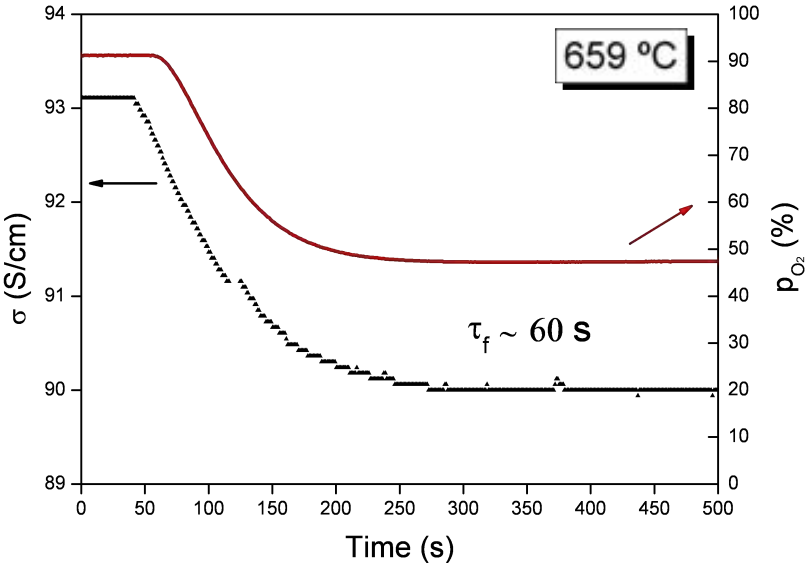

Figure 5.21: Oxygen pressure and conductivity data for a gas switch from 100 to 50% O_2 at 659 °C for the 335 nm $La_2NiO_{4+\delta}$ film grown on STO.

Both reduction (from 100 to 50%, from 50 to 25% and from 25 to 12.5% O_2) and oxidation (from 12.5 to 25%, from 25 to 50% and from 50 to 100% O_2) were performed with a sudden gas switch at 387, 477, 577 and 659 °C for both samples. We started at the lowest temperature, 288 °C, at which, due to the slow kinetics of the oxygen uptake/loss process, only some p_{O_2} were performed. Then, the temperature was increased by a controlled ramp up to 387 °C. Once the temperature was stabilized the three reducing pressure changes were done, followed by the three oxidation partial pressure changes. Then the next temperature was reached, and so on. At 659 °C, since the exchange process is fast, the relaxation time approaches the flush time of the reactor volume, as can be seen in Figure 5.21 in which the oxygen partial pressure variation is plotted together with the conductivity variation for a

change from 100 to 50% O_2 for the 335 nm $La_2NiO_{4+\delta}$ film grown on STO. The oxygen pressure curve (red line) nearly follows the conductivity curve (black triangles) with a short time elapse, as the oxygen sensor is placed after the exchange chamber. Therefore, it has not been possible to extract accurate surface exchange coefficients at this temperature. For the rest of temperatures the reactor flush time correction [127] was taken into account for the evaluation of the surface exchange coefficient. At 288 and 387 °C the flushing behavior of the reactor volume had no influence in the relaxation process, as the same surface exchange constants were obtained with and without the correction. But, as the temperature increases (477 and 577 °C), higher values of the surface exchange constants were obtained in comparison to the fitting without applying the flush time correction.

In Figure 5.22 we can see the gas partial pressure changes from approximately 25 to 12.5%, 12.5 to 25%, 25 to 50% and 50 to 100% O_2 at 477 °C, and the three reduction plus the three oxidation steps at 577 °C for the 335 nm $La_2NiO_{4+\delta}$ film deposited on STO. In the same graph the measured conductivity changes for each pressure change are shown. It is clearly observed that some of the conductivity curves do not have a simple exponential behavior. The presence of a slower kinetic process could be the cause for the apparent anomalies observed at certain temperatures which induce non reproducibility in the conductivity values depending on the sample history, as it is cleary observed in Figure 5.22.b.

Normalized ECR data at 577 °C with gas atmosphere switched from 25 to 50% O_2 for the 335 nm $La_2NiO_{4+\delta}$ film are shown in Figure 5.23. The red and blue lines correspond to the calculated values using the simple fit (Eq. 5.17) and the flush time correction fit (Eq. 5.26), respectively. The zone corresponding to short relaxation times has been enlarged and in it it can be observed that for the first 250 s of the ECR experiment the simple Eq. 5.17 does not fit accurately the experimental data. With the flush time correction curve higher more accurate values of the surface exchange coefficient are obtained: k_{Ex}(simple fit) = 1.10 x 10^{-7} cm/s and k_{Ex}(flush-time correction) = 1.14 x 10^{-7} cm/s.

Figure 5.24 shows the normalized ECR data at 577 °C with gas atmosphere switched from 100 to 50% O_2 for the 335 nm $La_2NiO_{4+\delta}$ film deposited on STO. The inset represents the simple exponential function fit (Eq. 5.17; red line), showing

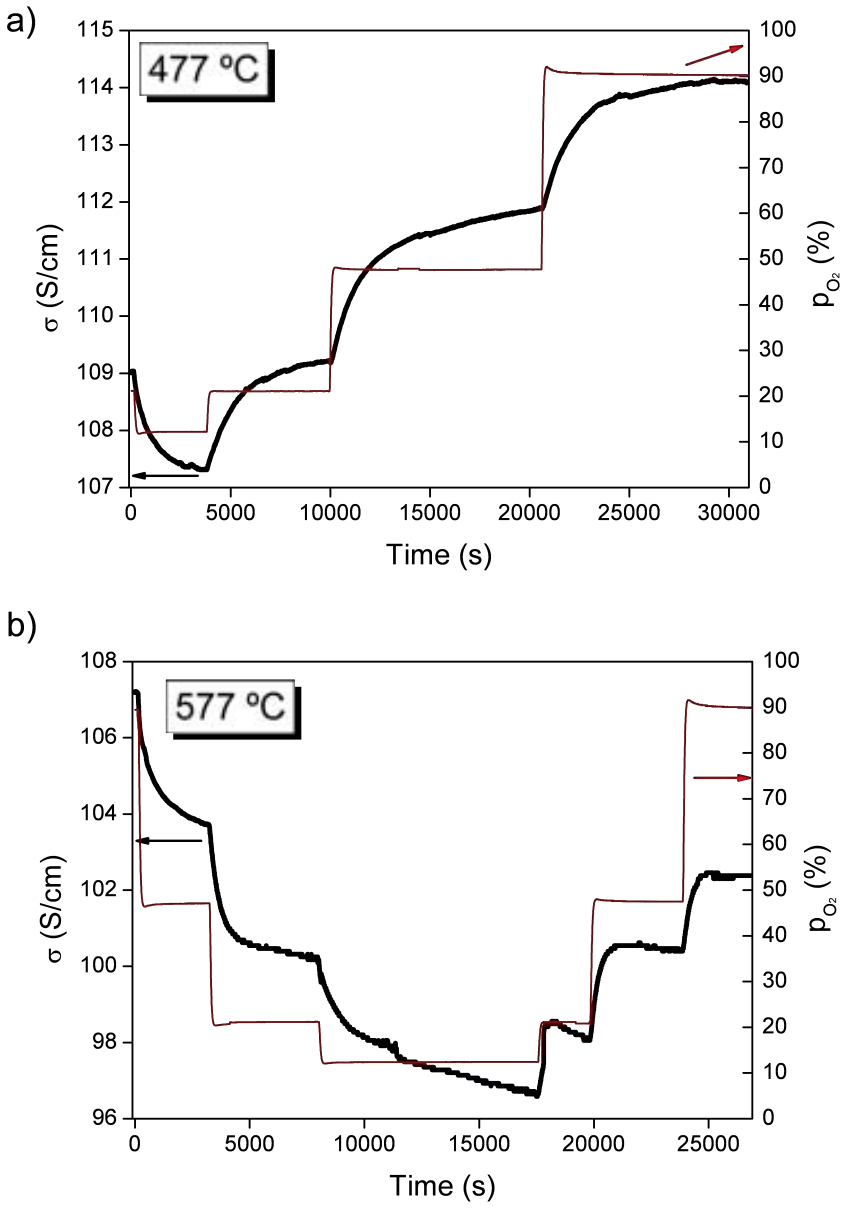

Figure 5.22: Oxygen pressure and conductivity data for a gas switches from approximately 25 to 12.5%, 12.5 to 25%, 25 to 50% and 50 to 100% O_2 at 477 °C, and the three reduction plus the three oxidation steps at 577 °C for the 335 nm $La_2NiO_{4+\delta}$ film grown on STO.

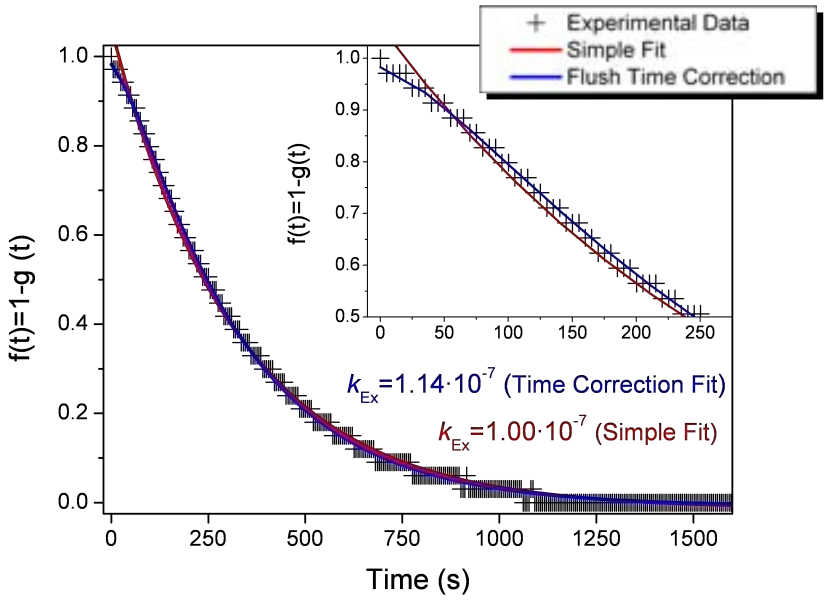

Figure 5.23: A set of ECR data with a gas switch from 25 to 50% O_2 at 577 °C for the 335 nm $La_2NiO_{4+\delta}$ film. The solid curves are the best fits for Eq. 5.17 (red) and Eq. 5.26 (blue).

a large deviation from the experimental data at the beginning and at the end of the ECR experiment. An adjustment to the flush-time correction equation does not improve the fitting. In some cases, as in this example, the fitting to one exponential function is not satisfactory enough and therefore correct values of the oxygen incorporation kinetics are not obtained using this model.

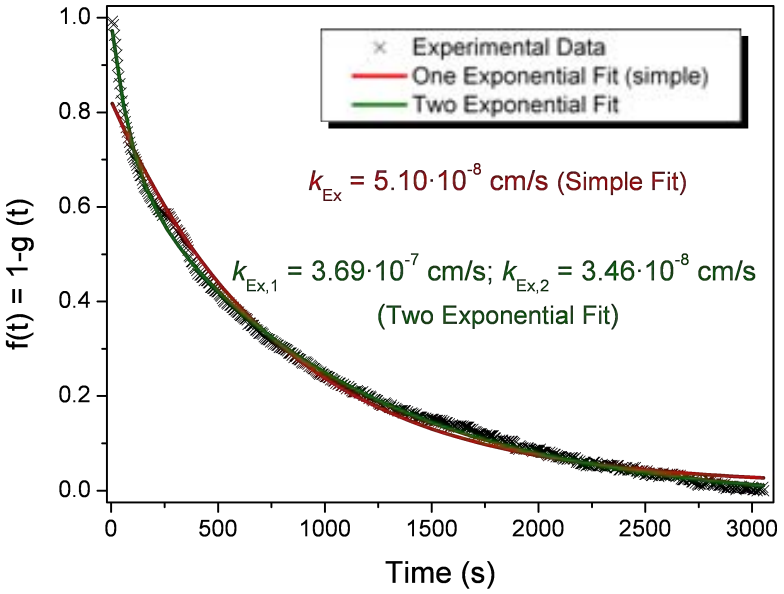

Figure 5.24: A set of ECR data with a gas switch from 100 to 50% O_2 at 577 °C for the 335 nm $La_2NiO_{4+\delta}$ film deposited on STO. The solid curves are the best fits for Eq. 5.17 (red) and Eq. 5.27 (green).

When using one exponential function it is assumed that only one process (oxygen removal or incorporation) contributes to the relaxation process. In order to accurately describe the measured relaxations curves, we have assumed that an additional process takes place at the same time, which we have described with one more exponential function according to the equation

$$g(t) = 1 - A_1 exp(-\frac{t}{\tau_1}) - A_2 exp(-\frac{t}{\tau_2}) \tag{5.27}$$

with

$$A_1 + A_2 = 1 \tag{5.28}$$

where

$$\tau_1 = \frac{l}{k_{Ex1}} \tag{5.29}$$

$$\tau_2 = \frac{l}{k_{Ex2}} \tag{5.30}$$

The fitting with the two exponential functions (Eq. 5.27) (green line) is more satisfactory, as can be seen in Figure 5.24. Two surface exchange coefficients are obtained, being, in this case, k_{Ex1} one order of magnitude higher than k_{Ex2}.

The surface exchange coefficients, k_{Ex1} and k_{Ex2}, calculated from Eqs 5.29 and 5.30, are shown in Figure 5.25 as a function of the temperature for the 100 to 50% step, and for the 335 nm thick film deposited on STO. The value of k_{Ex1} is two orders of magnitude higher than the value of k_{Ex2} at low temperatures and one order of magnitude higher at high temperatures, and the activation energy of k_{Ex1} is lower than that of k_{Ex2}.

Other authors have also used the double exponential model to obtain a better fitting to the ECR data for thin films of $(La_{0.6}Sr_{0.4})_{0.99}FeO_{3-\delta}$ on MgO [128], of the double perovskite $PrBaCo_2O_{5+\delta}$ on $SrTiO_3$ [129] and of $La_2NiO_{4+\delta}$ on $LaAlO_3$ [93]. For Soegaard [128] the most realistic interpretation is that the time constant were attributed to a chemical diffusion process. Besides, for the $(La_{0.6}Sr_{0.4})_{0.99}FeO_{3-\delta}$ thin films some of the relaxations curves could not be fitted with two exponential function but with three exponential functions. On the other hand, Kim et al. [129] attribute the double kinetic model to the existence of two independent regions in the $PrBaCo_2O_{5+\delta}$ film with different exchange rates that could correspond to two different film microstructures or two different reactions on the highly epitaxial film. In the case of the $La_2NiO_{4+\delta}$ [93], Kim et al. considered that the film is formed by two independent regions of different microstructure giving rise to different exchange rates. The faster surface exchange kinetics k_{Ex1} was assigned to (110) and (100) surfaces and the slower surface exchange kinetics k_{Ex2} to the (001) surface. In those

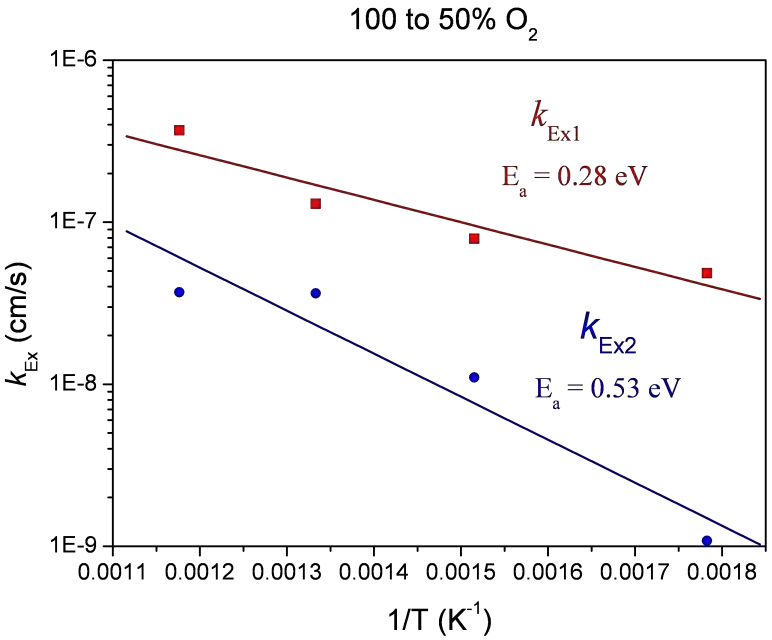

Figure 5.25: Surface exchange coefficients, k_{Ex1} and k_{Ex2}, as a function of temperature for a gas switch from 100 to 50% O_2 for the 335 nm $La_2NiO_{4+\delta}$ film.

experiments, the as-deposited film was (001) oriented, but the film was found to experience microstructure reconstruction during the ECR and two new reflections 200 and 220 appeared in the XRD patterns after the ECR.

In our case, we have not observed the appearence of different orientations of the $La_2NiO_{4+\delta}$ phase after the ECR experiments, although we cannot totally rule out the possibility of the existence of the (220) orientation, as the corresponding XRD peaks would be overlapped with those of the NGO or STO substrates. We have indeed observed the appearence of small peaks corresponding to the La_2O_3 phase, which could correspond to a different microstructure to which the second surface exchange coefficient k_{Ex2} could be associated. Other possibilities rather difficult to detect are also feasible, such as the existence of different facets or surface chemical bonds of the $La_2NiO_{4+\delta}$ structure exposed to the gas atmosphere, with different k_{Ex} associated, micro-structural changes in the film or even the influence of the Ag contacts.

In Figure 5.26 we have plotted the k_{Ex1} values in both oxidation and reduction kinetics as a function of the temperature for the two $La_2NiO_{4+\delta}$ films of different thickness and deposited on different substrate. We estimate the uncertainty on k_{Ex1} to be 30%, originating from the uncertainty in the fitting procedure and in the film thickness measurement. The four graphs correspond to the four different final pressures reached in the reaction chamber after the gas switch. It is observed that there is not much difference neither in k_{Ex1} surface value nor in the activation energy value between the oxidation process (blue squares for the 335 nm film deposited on STO and blue triangles for the 50 nm film deposited on NGO) and the reduction processes (red squares for the 335 nm film deposited on STO and red triangles for the 50 nm film deposited on NGO). Higher k_{Ex1} values are observed for the thicker film deposited on STO (squares), with small differences between films at high oxygen partial pressures ($p_f = 100\%$ O_2) and large differences at low oxygen partial pressures (1.5 orders of magnitude of difference for $p_f = 100\%$ O_2). The difference in the value of k_{Ex1} could be an effect of the surface roughness, larger in this film, or an effect of the different substrate on which the films have been grown, which induces different strain, cell parameters and oxygen content. The large roughness could enhance the exchange rate by a direct geometrical effect of increasing the effective surface area,

along with the possible enhancement of the surface activity through the formation of kinks or by the direct exposure of the exchange gas to different faces of the $La_2NiO_{4+\delta}$ structure. The activation energy of the process has values ranging from 0.25 to 0.40 eV for the 335 nm film, and slightly higher for the thinner film.

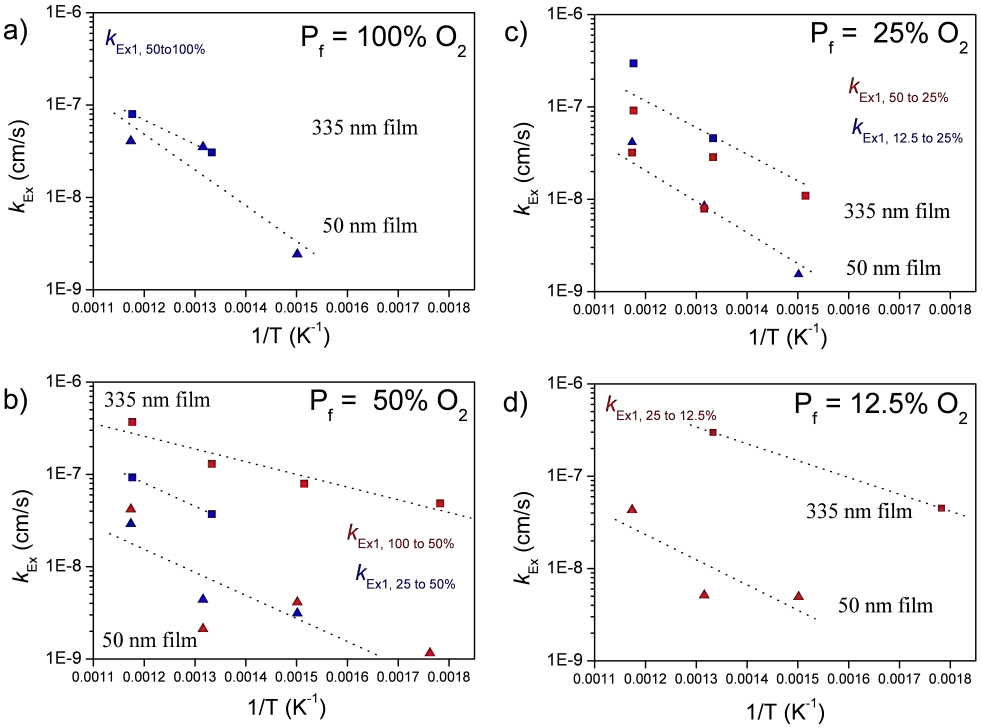

Figure 5.26: k_{Ex1} surface exchange coefficient as a function of temperature for gas switches a) with final oxygen pressure of 100%: from 50 to 100% (blue) b) with final oxygen pressure of 50%: from 100 to 50% (red) and from 25 to 50% O_2 (blue) c) with final oxygen pressure of 25%: from 50 to 25% (red) and from 12.5 to 25% O_2 (blue) and d) with final oxygen pressure of 12.5%: from 25to 12.5% (red). The data of the 335 nm $La_2NiO_{4+\delta}$ film on STO are plotted as squares and of the 50 nm $La_2NiO_{4+\delta}$ film on NGO as triangles. The dotted lines serve as eye guidelines for the data corresponding to each $La_2NiO_{4+\delta}$ film.

Figure 5.27 shows the surface exchange coefficient, k_{Ex1}, as a function of p_{O_2} (both in logarithmic scale) at the temperatures of 393 and 579 °C. Due to the possi-

ble errors inherent to the fitting process and to the small pressure range measured, it has not been possible to determine the pressure dependence of the surface exchange coefficient.

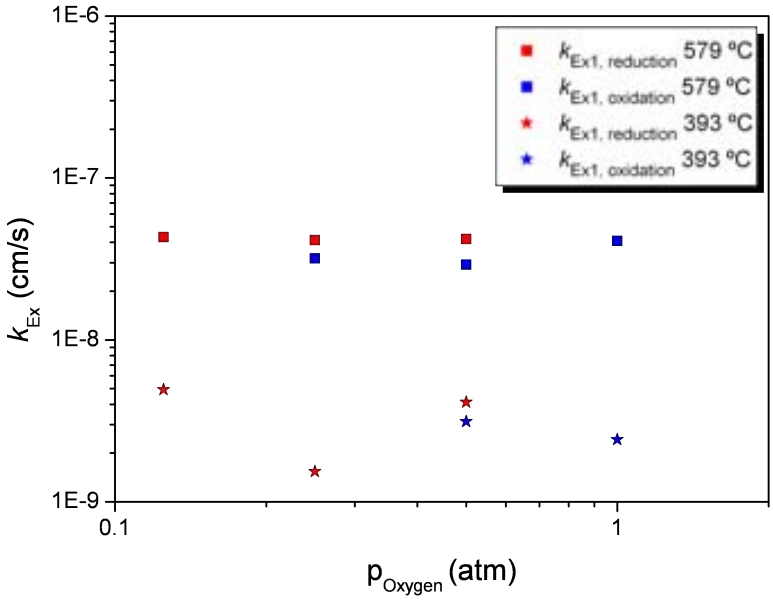

Figure 5.27: k_{Ex1} surface exchange coefficient as a function of oxygen partial pressure for oxidizing (blue) and reducing (red) gas switches for the 50 nm (triangles) $La_2NiO_{4+\delta}$ films at 393 (stars) and 579 °C (squares).

To our knowledge, the pressure dependence of the chemical surface exchange coefficients has not yet been measured for the $La_2NiO_{4+\delta}$ material. Its variation with pressure will depend on the surface reaction involved and on the mechanism control. For example, for a master case studied by Maier [115], assuming the reaction taking place in the surface is:

$$\frac{1}{2}O_2 + V_O^{\cdot\cdot} + 2e^- \longleftrightarrow O_O \tag{5.31}$$

the pressure dependence will vary from $\partial lnk_{Ex}/\partial lnp \approx 0$ for the thin layer control, to $\partial lnk_{Ex}/\partial lnp \approx \frac{1}{2}$ for the charge transfer control, and to $\partial lnk_{Ex}/\partial lnp \approx 1$

for the adsorption control case.

The ECR measurements on a 300 nm $La_2NiO_{4+\delta}$ thin film by Kim et al. [93] were carried out in a higher temperature range (from 592 to 723 °C), but by comparing their extracted values at 592 °C ($k_{Ex1} \approx 5.5$ x 10^{-6} cm/s, $k_{Ex2} \approx 2.3$ x 10^{-7} cm/s) it seems that the "fast" surface exchange coefficient (k_{Ex1}) observed in our films is close to their "slow" surface exchange coefficient (k_{Ex2}). This would be in agreement to their theory associating the "slow" k_{Ex2} to the (001) orientation (corresponding to the orientation of the surface of our films), which has proven to be the major orientation in our $La_2NiO_{4+\delta}$ films found by XRD performed after the ECR measurements.

5.4 Conclusions

We have developed and validated a methodology for the determination of anisotropic tracer diffusion and surface exchange coefficients, D^* and k^*, in two perpendicular directions for high quality epitaxial thin films by the isotopic exchange technique.

We have studied the tracer oxygen exchange and transport in *c*-axis oriented $La_2NiO_{4+\delta}$ epitaxial films grown on STO (100) and NGO (110) by PI-MOCVD, and compared the results with those reported in the literature [24] for single crystals. The effect that the strain induced by the mismatch between the film and the substrate has on the oxygen diffusion through the film has been evaluated by measuring films with different thickness ranging from 33 to 370 nm (from 100 to 370 nm for the transversal experiment).

The oxygen transport along the *c*-axis and along the *a*-*b* plane was found to increase with film thickness, i.e., as the stress of the film decreases. It is worth pointing out that the opposite behavior was found in the case of the total conductivity measured along the *a*-*b* plane (Chapter 4), which decreased with film thickness. Conversely, the thickness seems to have no effect in the tracer surface exchange coefficient.

The thickest films have been found to consist of two regions with different *c*-axis tracer diffusion coefficient values, a higher and constant one close to the film surface and a lower and variable one close to the substrate. The differences in D_c^* could be

associated to differences in strain along the film thickness.

As expected, the tracer diffusion and surface exchange coefficients are thermally activated and are approximately two orders of magnitude lower along the c-axis than along the a-b plane. The D^*_{ab} and k^*_{ab} values for thin films are close to those previously measured for single crystals for the a-b plane, while the D^*_c and k^*_c values along the c-axis direction are lower, which could be an effect of the induced strains in our $La_2NiO_{4+\delta}$ thin films. The low activation energies of D^* for both directions confirm the contribution of a vacancy mechanism to the ionic conduction at low temperatures.

Chemical surface exchange coefficients have been measured by electrical conductivity relaxation experiments performed on two c-axis oriented epitaxial $La_2NiO_{4+\delta}$ thin films, 50 and 335 nm thick, deposited on a 5x5 mm^2 (110) NGO and (001) STO substrates, respectively.

The flush time correction was found not to be necessary at low temperatures (288 and 387 °C), while it was proven to be valid and to successfully fit the experimental data at intermediate temperatures (477 and 577 °C).

It was found that some ECR data could not be fitted with one single exponential function but by a double-exponential model, which has been previously used by several authors for thin film ECR measurements. The physical meaning of this second exponential process is difficult to identify. Different hypothesis, mainly related to the chemical surface state, have been proposed to explain its origin.

The c-axis chemical surface exchange coefficient is thermally activated, but it has not been possible to determine its pressure dependence.

The 335 nm $La_2NiO_{4+\delta}$ film deposited on NGO presented higher k_{Ex} values than the 50 nm one deposited on STO. This could either be an effect of the surface roughness or could be associated to the differences in cell parameters, strain and δ associated to the different substrates.

Our "fast" surface exchange coefficient (k_{Ex1}) is close to the "slow" surface exchange coefficient (k_{Ex2}) measured by Kim et al. [93], which would be in agreement to their theory associating their "slow" k_{Ex2} to the (001) orientation (corresponding to the orientation of the surface of our films).

Comparing the ECR and the isotope c-axis surface exchange data we observed

that, as expected, the k_{Ex} values are much larger (two orders of magnitude) than the k^* values. The activation energy of the isotope exchange k_c^* was 0.38 eV, similar to the obtained values for the ECR measurement, which seems to confirm the validity of the data obtained from both experiments.

Chapter 6

Preparation and Characterization of $La_{n+1}Ni_nO_{3n+1}$ Thin Films

Very recently there has been a renewed interest in the study of $La_{n+1}Ni_nO_{3n+1}$ compounds in view of their potential application as cathodes for SOFCs [62]. It is expected that the higher-ordered RP phases, $La_{n+1}Ni_nO_{3n+1}$ (n = 2 and 3) would be superior candidates from a stability point of view for intermediate temperature SOFCs than $La_2NiO_{4+\delta}$ [62]. In addition, different studies on the n = 1, 2, 3, or ∞ phases in the literature evidence that the electronic transport in $La_{n+1}Ni_nO_{3n+1}$ depends to a large extent on the number of perovskite blocks, n, gradually varying from an insulating to a metallic behavior upon increasing n [68–71]. These changes are mainly associated with variations in the Ni valence state from Ni^{2+} for n = 1 member ($La_2NiO_{4+\delta}$) to Ni^{3+} for the n = ∞ member ($LaNiO_3$), along with the oxygen content [73]. In these compounds, and because of their layered structure, the transport properties are highly anisotropic, being both the electronic and ionic transport maximum along the *a*-*b* plane of the structure [24, 50, 59, 64]. Therefore, for an accurate analysis of their transport properties it is necessary to use single crystal samples or thin epitaxial films.

6.1 Deposition of $La_{n+1}Ni_nO_{3n+1}$ Thin Films

$La_{n+1}Ni_nO_{3n+1}$ thin films have also been grown by PI-MOCVD using $La(thd)_3$ and $Ni(thd)_2$ metalorganic precursors dissolved in 1,2-dimethoxyethane. The molar ratio of La/Ni in the precursor solution was varied from 1 to 4 while the experimental conditions employed were the same as selected for the $La_2NiO_{4+\delta}$ film growth, namely:

- Deposition temperature: 750 °C
- Reactor pressure: 10 Torr
- Injector aperture time: 2 ms
- Pulse frequency: 1 Hz
- Total concentration of the solution: 0.02 M
- Total gas flow of 1 l/h
- Ratio of oxygen to argon: 1:1

The same two types of single crystal substrates with perovskite structure have been used to grow the films: NGO (110) and STO (100). The mean mismatch at the interphase for all the members of the $La_{n+1}Ni_nO_{3n+1}$ series, for each substrate, has been calculated as an average between the difference in the cell parameters for two in-plane directions and is shown in Table 6.1.

Table 6.1: Mean mismatch at the interphase for all the $La_{n+1}Ni_nO_{3n+1}$ members

Phase	*n*	Crystal System	Cell parameters (Å)			ICSD Coll. Code	Ref.	Mismatch	
			a	*b*	*c*			STO	NGO
$La_2NiO_{4.18}$	1	orthorh.	5.4652	5.4687	12.678	44121	[107]	+1.02%	-0.19%
$La_3Ni_2O_7$	2	orthorh.	5.3928	5.4486	20.5185	91141	[72]	+1.88%	+0.67%
$La_4Ni_3O_{10}$	3	orthorh.	5.415	5.465	27.959	80279	[75]	+1.52%	+0.31%
$LaNiO_3$	∞	orthorh.	5.4535	5.4535	13.014	67715	[130]	+1.27%	+0.06%

All the members of the Ruddlesden-Popper family have larger mismatch values for the STO substrates, while those for the NGO substrate are quite low in all cases. For both substrates the highest mismatch value among all the $La_{n+1}Ni_nO_{3n+1}$ members is found for the $La_3Ni_2O_7$ phase.

In order to control the La/Ni ratio in the deposited film it was necessary to perform a calibration under the employed experimental conditions. Figure 6.1 shows the relationship between the La/Ni ratio measured in films deposited at 750 °C on STO substrates as a function of the La/Ni ratio in the precursor solution. A linear correlation is clearly observed. The slope of the curve is about 0.7, making the La/Ni ratio in the film lower than in the solution for the whole composition range. This deviation in the composition transfer is typical for the MOCVD processes and occurs because each precursor has a different decomposition and deposition yield, as has been previously explained. The deposited $La_{n+1}Ni_nO_{3n+1}$ is nickel-rich compared with the injected precursor mix, which has previously been observed by Lane et al. in $La_{n+1}Ni_nO_{3n+1}$ layers prepared by MOCVD [108] and by Faucheux et al. in $La_2NiO_{4+\delta}$ layers prepared by PI-MOCVD [90].

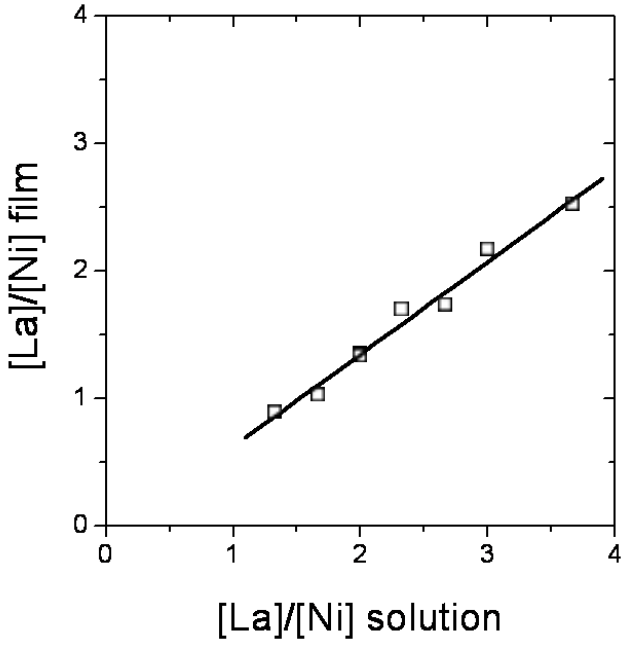

Figure 6.1: Correlation between measured La/Ni composition ratio in the La-Ni-O films deposited on STO substrates at 750 °C and the one used in the organometallic precursor solution.

6.2 Structural and Morphological Characterization of $La_{n+1}Ni_nO_{3n+1}$ Thin Films

The XRD patterns of the films deposited on NGO substrates varying the La/Ni molar ratio are shown in Figure 6.2. Along with substrate reflections (indicated by * in the figure) intense reflections are observed, which match very well those of the main 00l reflections of different phases in the RP series. This observation confirmed the high degree of *c*-axis orientation of the layers. From the position of the X-ray diffraction peaks, the films with a La/Ni ratio close to 2 (Figure 6.2.a), close to 1.5 (Figure 6.2.c) and close to 1.34 (Figure 6.2.d), were apparently composed by pure phase Ruddlesden-Popper structures $La_2NiO_{4+\delta}$ ($n = 1$), $La_3Ni_2O_7$ ($n = 2$) and $La_4Ni_3O_{10}$ ($n = 3$), respectively. For those samples the *c*-axis parameters were measured to be 12.715 Å, 20.310 Å, and 27.962 Å, respectively, in agreement with the corresponding RP phases (ICSD Collection Codes 44121, 91141 and 80279) [72, 75, 107]. However, in the films with $n = 2$ and $n = 3$ there is a slight broadening of the diffraction peaks, along with a low relative intensity of the weaker peaks (indicated with grey arrows in the figure) that did not reach the expected values of the pure phases. These observations could be an indication of the presence of defects in the structure.

In the films with an intermediate value of La/Ni =1.7 (Figure 6.2.b), between the La/Ni composition of $n = 1$ and $n = 2$ phases, the diffraction patterns did not show any evidence of the presence of extended regions of either $n = 1$ or $n = 2$ phases. Instead, the diffraction pattern shows a single set of peaks in average positions, corresponding to a combination of different RP phases (Figure 6.2.b) as it would correspond to an intergrowth structure with domain thickness below the coherence length of the X-rays. For La/Ni close to 1 (Figure 6.2.e), the films present the perovskite $LaNiO_3$ structure ($n = \infty$) with a very small peak at 62.9 degrees corresponding to the 400 reflection of the NiO phase. The *c*-axis parameter measured for the $LaNiO_3$ structure was 3.84 Å, consistent with the pseudocubic cell parameters found in the literature ($a_{pseudocubic}$ = 3.86 Å; ICSD Collection Code 67715) [130].

The XRD patterns of the films with varying La/Ni molar ratio for the films deposited on STO substrates are shown in Figure 6.3. Along with substrate reflections

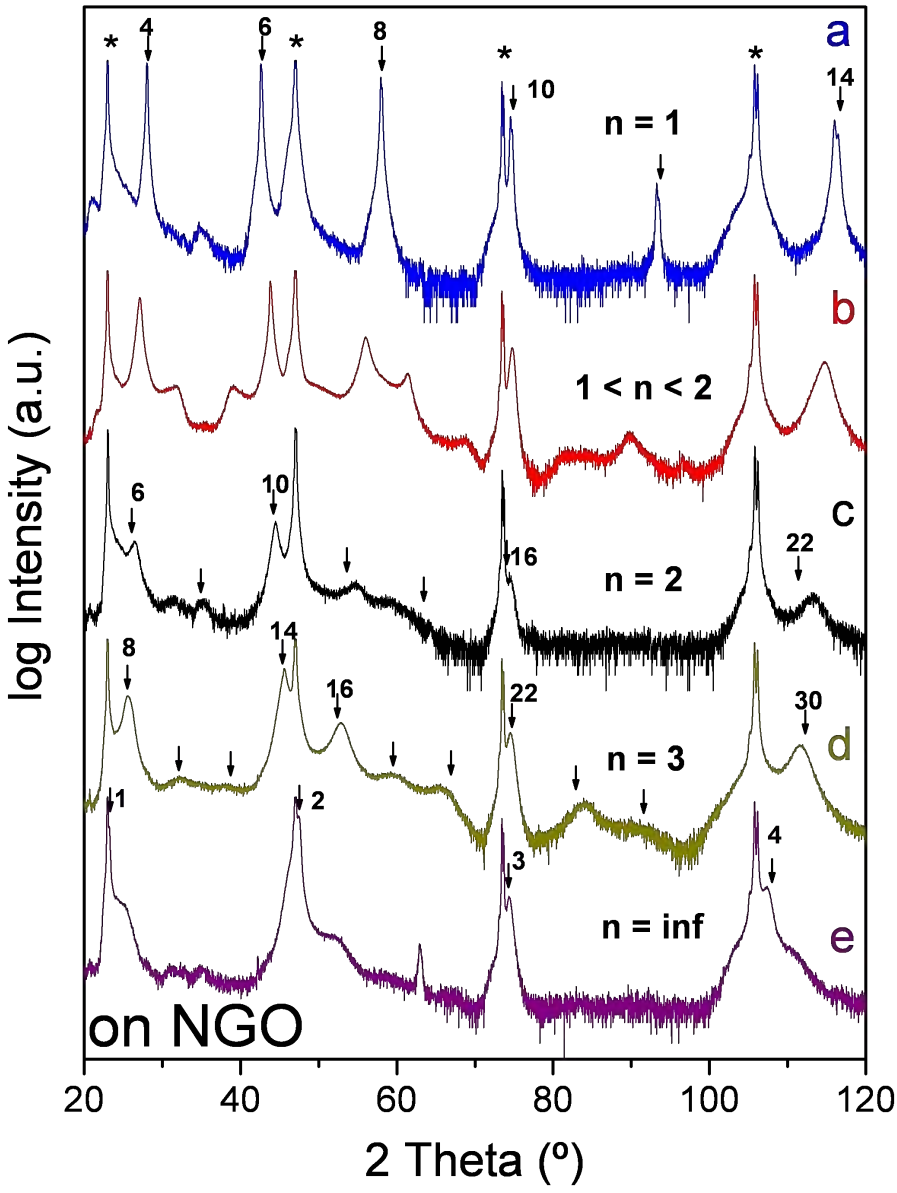

Figure 6.2: XRD patterns of films deposited on NGO with different La/Ni ratio values of 2.0 (a), 1.7 (b), 1.5 (c), 1.34 (d), and 1.0 (e). The arrows indicate the expected positions for the (00l) peaks corresponding to c-axis oriented samples of the different $La_{n+1}Ni_nO_{3n+1}$ phases of the R-P series: $La_2NiO_{4+\delta}$ ($n = 1$), $La_3Ni_2O_7$ ($n = 2$), $La_4Ni_3O_{10}$ ($n = 3$) and $LaNiO_3$ ($n = \infty$).

(indicated by * in the figure), we observed other reflections, corresponding to the $La_{n+1}Ni_nO_{3n+1}$ phases, which decreased in intensity as the La/Ni molar ratio decreases. For a La/Ni ratio close to 2 (Figure 6.3.a) the observed narrow peaks match very well those of the main 00l reflections of the $La_2NiO_{4+\delta}$ phase, confirming the high orientation of the film. The *c*-axis parameter was measured to be 12.635 Å. In the films with La/Ni ratio values of La/Ni = 1.7 (Figure 6.3.b), La/Ni close to 1.5 (Figure 6.3.c), La/Ni close to 1.34 (Figure 6.3.d) and La/Ni close to 1 (Figure 6.3.e) the diffraction patterns show a set of peaks in average positions, in the same way as on NGO. In this case, it is not possible to associate the set of peaks to one unique phase, a more complex intermixing of different RP phases is observed in comparison with films deposited on NGO under the same conditions. The peaks are not as intense and their width is larger, corresponding to a more defective structure. Other minor peaks corresponding to different orientations of $La_{n+1}Ni_nO_{3n+1}$ also appear in the XRD patterns.

For films deposited on both substrates and La/Ni concentrations above 2 in addition to the peaks corresponding to the $La_2NiO_{4+\delta}$, extra peaks corresponding to the La_2O_3 phase were obtained. In the case of La/Ni concentration ratios in the film below 1, in addition to the $LaNiO_3$ phase peaks, other peaks corresponding to the NiO phase also appeared.

The *c*-axis parameter in the $La_{n+1}Ni_nO_{3n+1}$ compounds can vary substantially depending on the oxygen content, and in particular for thin films, it might be affected by the strain induced as a result of the substrate mismatch. This fact makes difficult any comparison between the structure of the films only based in cell parameters differences. Instead, we can examine the relative peak positions. Regardless the *c*-axis parameter, and in a perfectly periodical structure along [001], the relative peak positions of two 00l and 00l' reflections should verify:

$$\frac{sin\theta_{l'}}{sin\theta_l} = \frac{l'}{l} \tag{6.1}$$

which derives simply from Bragg's law.

In the case of the $La_{n+1}Ni_nO_{3n+1}$ RP series we can derive an empirical relationship between the relative angular positions and the La/Ni composition. If we take

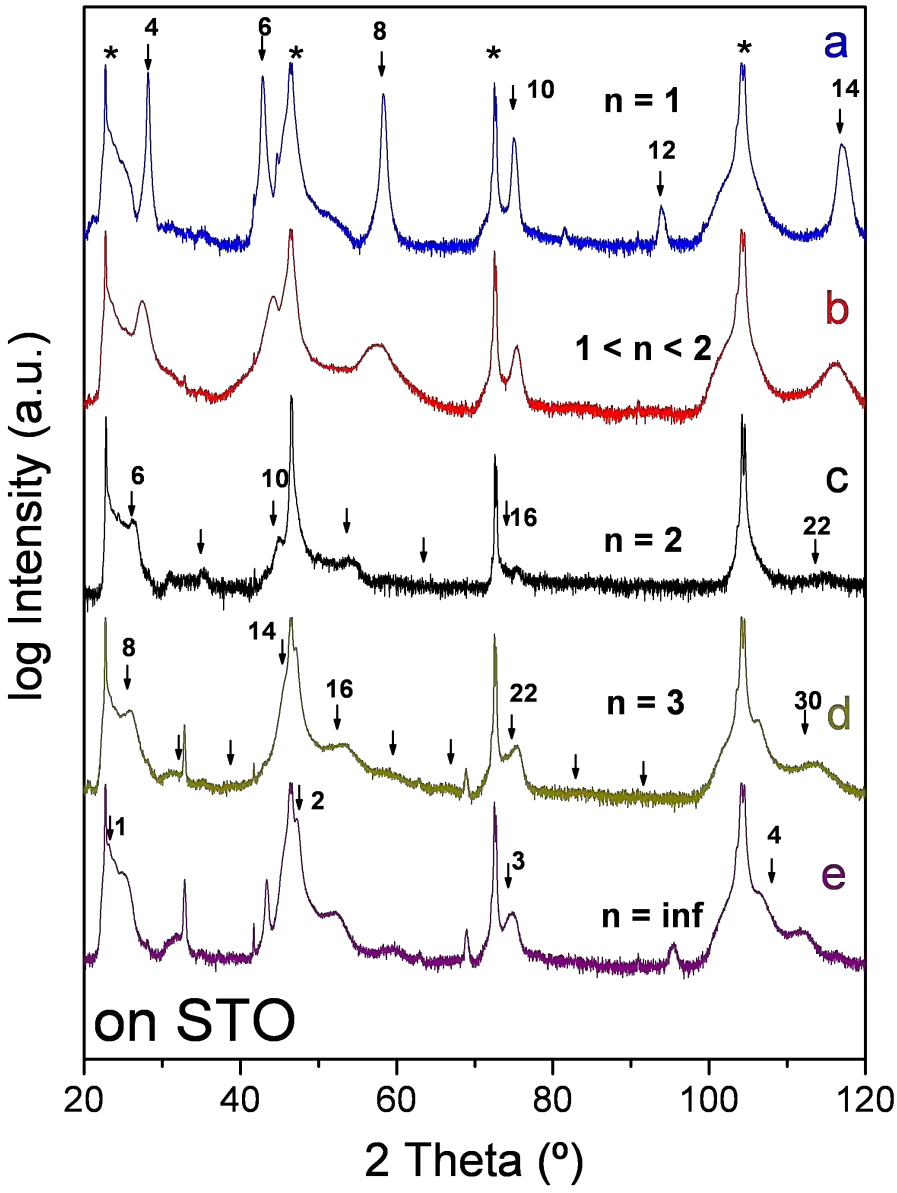

Figure 6.3: XRD patterns of films deposited on STO with different La/Ni ratio values of 2.0 (a), 1.7 (b), 1.5 (c), 1.34 (d), and 1.0 (e). The arrows indicate the expected positions for the (00l) peaks corresponding to c-axis oriented samples of the different $La_{n+1}Ni_nO_{3n+1}$ phases of the R-P series: $La_2NiO_{4+\delta}$ ($n = 1$), $La_3Ni_2O_7$ ($n = 2$), $La_4Ni_3O_{10}$ ($n = 3$) and $LaNiO_3$ ($n = \infty$).

only into consideration the two main peaks 00l and 00l' in the 2θ range between 20 and 50 degrees, they correspond to l'/l = 6/4 for $n = 1$; 10/6 for $n = 2$; 14/8 for $n = 3$, and 2/1 for $n = \infty$, which can be expressed as l'/l = $(2n+1)/(n+1)$ for the different n values.

In Figure 6.4 this region of the XRD patterns for the $La_{n+1}Ni_nO_{3n+1}$ films deposited on NGO has been enlarged. It is clearly observed that the two main peaks tend to separate as the n value increases, while other small peaks appear in the intermediate region. Since La/Ni composition ratio in $La_{n+1}Ni_nO_{3n+1}$ is $(n+1)/n$, we can derive a general expression for the RP pure phases:

$$\frac{sin\theta_{l'}}{sin\theta_l} = \frac{l'}{l} = \frac{2n+1}{n+1} = 1 + \left[\frac{[La]}{[Ni]}\right]^{-1} \tag{6.2}$$

Figure 6.5 shows the measured angular position ratio from the XRD pattern against the experimental La/Ni composition ratio for the set of films in our experiment, along with the expected dependence for pure RP phases with different n value (dashed curve in the figure). All the films follow very closely the expected dependence, particularly for those on NGO substrates. The films with La/Ni ratio close to 2, 1.5, 1.34, and 1.0 lay in the positions as if they corresponded to $n = 1$, $n = 2$, $n = 3$ and $n = \infty$ pure phases, respectively. The peak position ratio for the film with La/Ni = 1.7 lies along the same curve between $n = 1$ and $n = 2$. This means that all La and Ni in the films are exclusively forming RP phases, since any La or Ni excess participating of a secondary phase would cause a deviation from the above mentioned dependence. For films with La/Ni composition ratio above 2, the peak position ratio remains equal to 1.5, as it corresponds to $La_2NiO_{4+\delta}$, and La excess forms other secondary phases, such as La_2O_3. In the same way for La/Ni composition ratio below La/Ni = 1, the films consist of $LaNiO_3$ perovskite, with peak position ratio 2.0, and Ni in excess is forming some secondary phases, as NiO, which can be observed in the diffraction pattern for some films.

Due to the larger mismatch between the film and the substrate it has not been possible to obtain high quality $La_{n+1}Ni_nO_{3n+1}$ films with $n > 1$ on STO substrates. In addition, the value of the conductivity for NGO is several orders of magnitud smaller than the value for STO. Therefore, by using a NGO substrate we ensure a neglegible influence of the substrate in the conductivity measurements. Therefore,

for a better understanding of the fundamental phenomena, we have focused our research in the $La_{n+1}Ni_nO_{3n+1}$ films obtained on the NGO substrates.

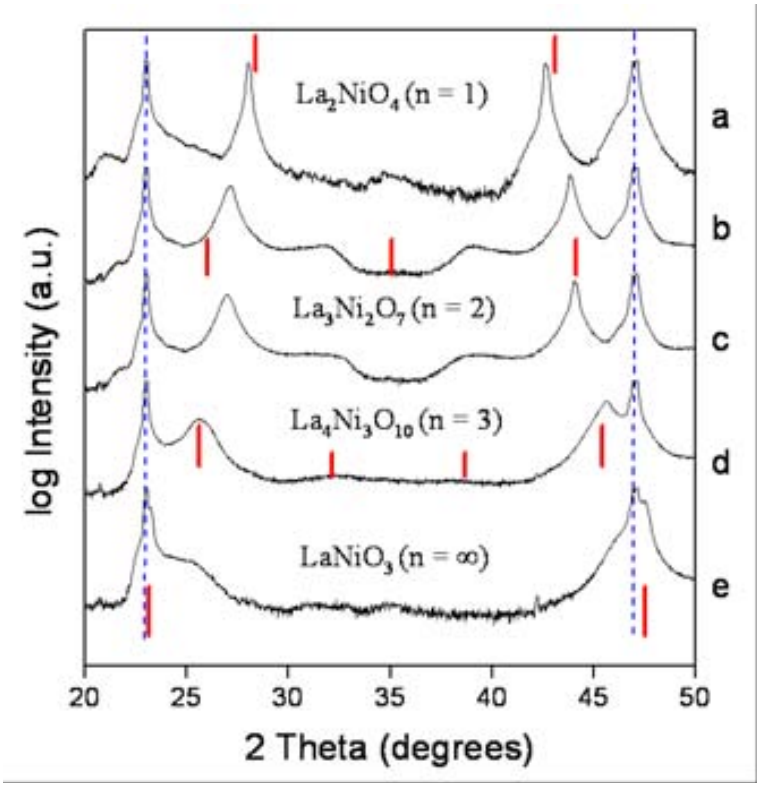

Figure 6.4: XRD patterns of films deposited on NGO with different La/Ni ratio values of 2.0 (a), 1.7 (b), 1.5 (c), 1.34 (d), and 1.0 (e). The red lines indicate the expected positions for the (00l) peaks corresponding to *c*-axis oriented samples of the different $LaNiO_3$ phases of the R-P series: $La_2NiO_{4+\delta}$ ($n = 1$), $La_3Ni_2O_7$ ($n = 2$), $La_4Ni_3O_{10}$ ($n = 3$) and $LaNiO_3$ ($n = \infty$).

6.3 Microstructural Characterization of $La_{n+1}Ni_nO_{3n+1}$ Thin Films

In order to assess the high quality and epitaxial growth of the films as well as to determine the real microstructure, transmission electron microscopy (TEM) was performed for the films with La/Ni = 2.0, 1.7, 1.5 and 1.34 on NGO substrates.

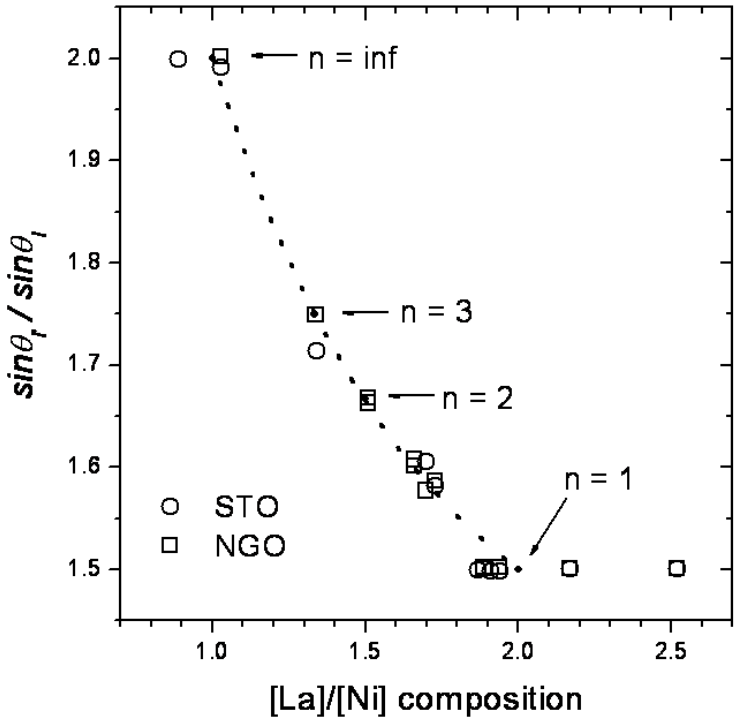

Figure 6.5: Dependence of the relative angular positions (expressed as sinθ) for the two main reflections (00l) and (00l') in the 2θ range between 20° and 50° for the deposited films with different La/Ni composition on NGO and STO substrates. The dashed curve corresponds to the expected dependence for pure Ruddlesden-Popper $La_{n+1}Ni_nO_{3n+1}$ phases, as discussed in the text. The arrows indicate the positions for pure $n = 1$, 2, 3, and ∞ phases. (The corresponding set of reflections are: l' = 6 and l = 4 for $n =$ 1, 10 and 6 for $n = 2$, 14 and 8 for $n = 3$, and 2 and 1 for $n = \infty$).

The high-resolution (HREM) image of the cross-section of the film with La/Ni = 2, along with the corresponding ED pattern has been shown and explained in detail in Section 4.3, Figure 4.11, page 73.

A careful examination using HREM revealed a more complex situation in films with lower La/Ni composition values, as already suspected from the XRD patterns. Figure 6.6 shows the HREM cross-section image of the La/Ni = 1.7 film. A very defective intergrowth structure parallel to the substrate surface is observed, evidenced by the streaking of the intensity distribution along $\mathbf{c}^*$ in the ED pattern from the film. A more detailed observation shows that the films consist of a random intergrowth of regions with different stacking sequences. The number of consecutive perovskite layers separated by rock salt layers are indicated in the figures. Generally, we found regions with a non periodical sequence of single and double perovskite layers (such as region B in Figure 6.6), where the bright dots represent columns of heavy atoms of two somehow different intensities: dark layers correspond to the rock-salt slabs and bright layers to the perovskite-type slabs. In those regions the average La/Ni composition lays clearly between 2 and 1.5, which would correspond to $La_2NiO_{4+\delta}$ (n = 1, stacking sequence of single perovskite layers) and $La_3Ni_2O_7$ (n = 2, double perovskite layers), respectively. Locally, we could observe regions with a periodic sequence of one single perovskite layer and one double perovskite layer (such as region A in Figure 6.6), which would correspond to La/Ni = 1.67 very close to the nominal value 1.7 of the film. The average n value calculated from the different regions in the image is about 1.45.

The cross-section of the films with La/Ni = 1.5, (in Figure 6.7), which seemed to correspond to $n = 2$ phase from the X-ray diffraction patterns, also shows a very defective stacking sequence composed basically by a random intergrowth of regions of $n = 1$, 2 and 3 stacks. As in the case before, the ED patterns show the streaking of the film peaks along $\mathbf{c}^*$ induced by the high density of planar defects. However, the average n value taken from the image remains very close to 2 as it corresponds to La/Ni = 1.5.

The same occurs in the cross-section of the films with La/Ni = 1.34 (in Figure 6.8), that also shows a very defective stacking sequence, evidenced by the streaking in the ED patterns. Despite the diffraction pattern, that suggested that the structure

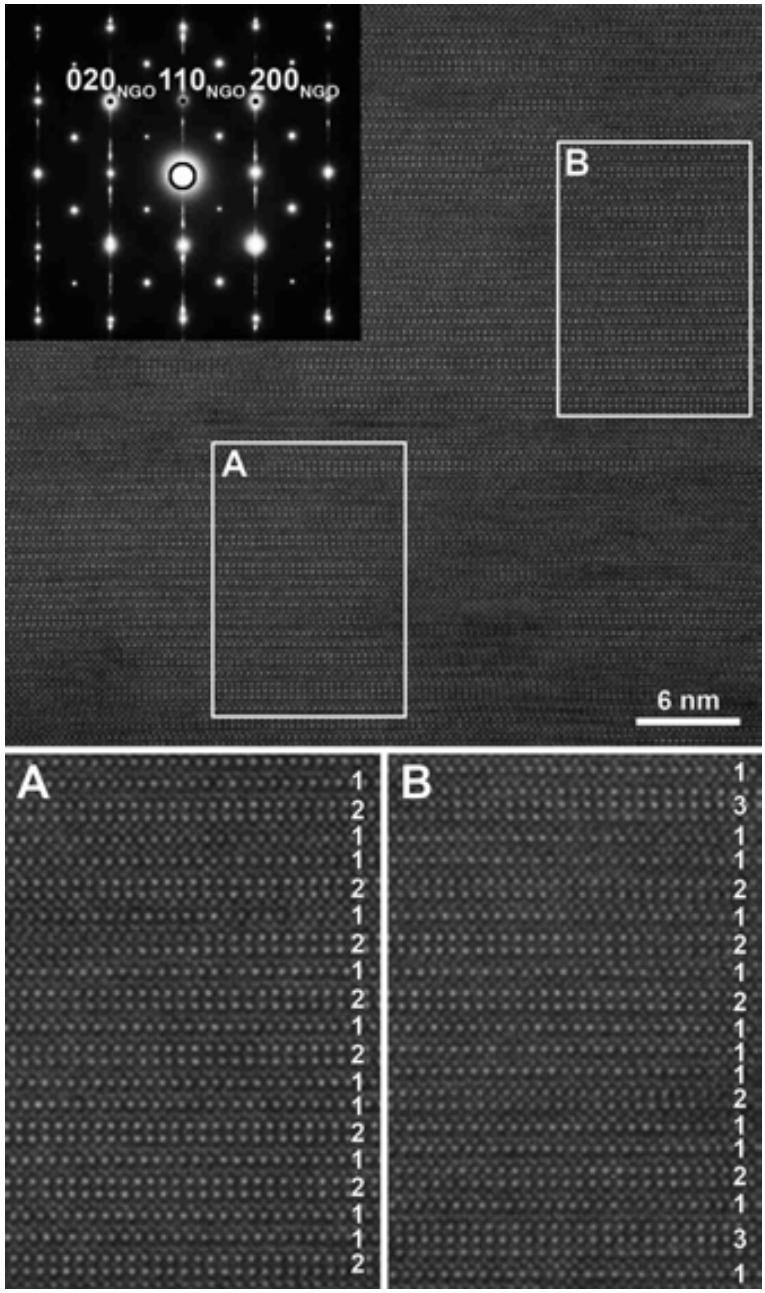

Figure 6.6: Cross-section HREM image and corresponding ED pattern of the film with La/Ni = 1.7 deposited on NGO. The image shows a highly defective stacking sequence of single and double perovskite-type layers). The insets are magnified images of of two different regions with (A) an apparent higher degree of a local periodic arrangement consisting of one double and single perovskite layer sequence, and (B) a lower degree of order. The average n value calculated from the image is 1.45.

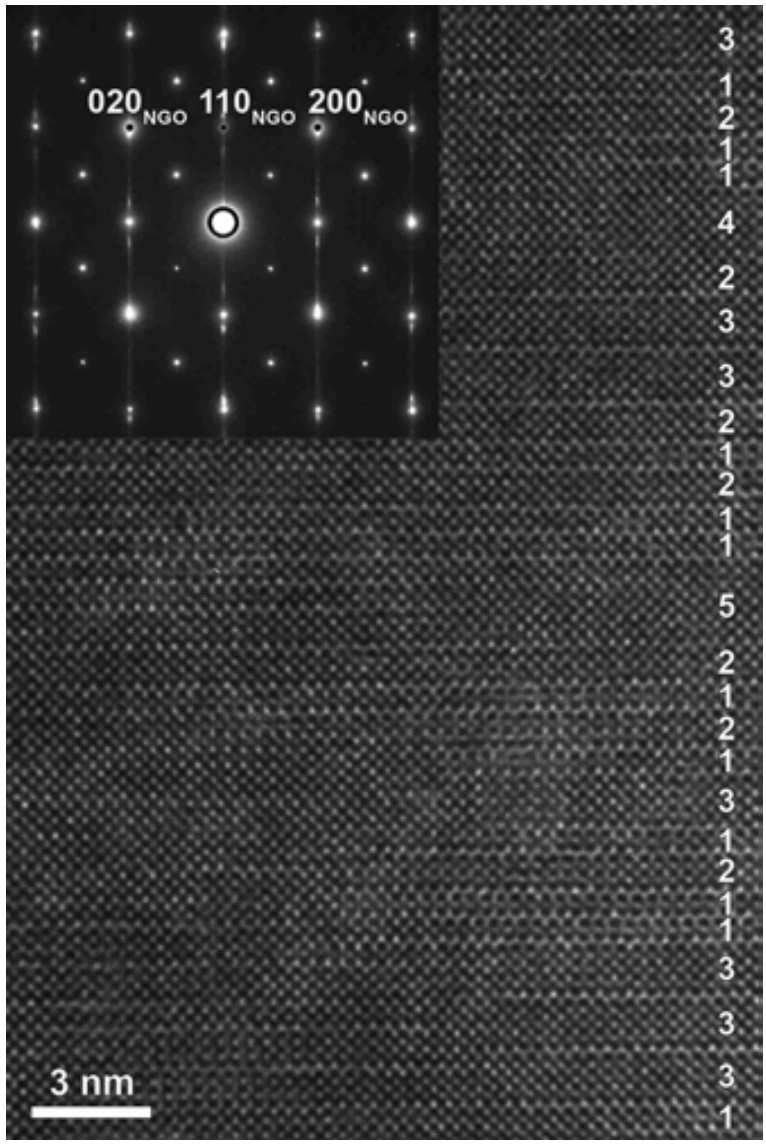

Figure 6.7: Cross-section HREM image and corresponding ED pattern of the film with La/Ni = 1.50 deposited on NGO. The film consists mainly of intermixed regions of $n = 1$, 2 and 3. The average n value calculated from the image is 2.0.

corresponded to pure $n = 3$ phase, the film is composed mainly by the random intergrowth of regions of $n = 2$, 3 and 4 domains. Small areas of higher n sequence were also observed. The average n value estimated from the image was about 3.4, slightly higher than the expected $n = 3$ for La/Ni = 1.33.

The HREM cross-section and the ED pattern of the films with La/Ni = 1.0 (shown in Figure 6.9), evidenced the formation of $LaNiO_3$ perovskite with epitaxial cube-on-cube arrangement on the NGO substrate, if one considers the pseudocubic cells of $LaNiO_3$ and NGO. According to the ED pattern, that has been indexed for $LaNiO_3$ in the trigonal R3c group, the (012) $LaNiO_3$ plane is parallel to the NGO (110) plane. The arrows in the figure indicate the presence of planar defects perpendicular to the interface, which correspond to twinned $LaNiO_3$ domains of about 3 to 10 nm thickness.

In general, for the films with La/Ni composition ratio between 1 and 2, we observed intermixed phases, and the extent of the periodicity along the c-axis never exceeds the 10 nm length, so the X-ray diffraction gives peaks corresponding to average interplanar spacing with a peak broadening that reflects the very small coherence length of the crystal domains.

Our observation confirmed the difficulties to obtain pure phases of higher members ($n = 2, 3, \ldots$) of the RP series in the La-Ni-O system, induced by kinetic limitations. This difficulty is enhanced when growing c-axis oriented thin films from the vapor phase, because any small fluctuation of the La/Ni composition during growth will locally turn into defects in the stacking sequence, giving rise to the intergrowth of different $La_{n+1}Ni_nO_{3n+1}$ domains.

6.4 Total Conductivity Properties of $La_{n+1}Ni_nO_{3n+1}$ Thin Films

We performed conductivity measurements for the films with La/Ni = 2.0, 1.7, 1.5 and 1.34 on NGO substrates as a function of temperature under different oxygen partial pressure atmospheres by flowing pure oxygen and pure nitrogen in the measurement chamber.

The film with La/Ni = 2.0, corresponding to $La_2NiO_{4+\delta}$ ($n = 1$), showed a

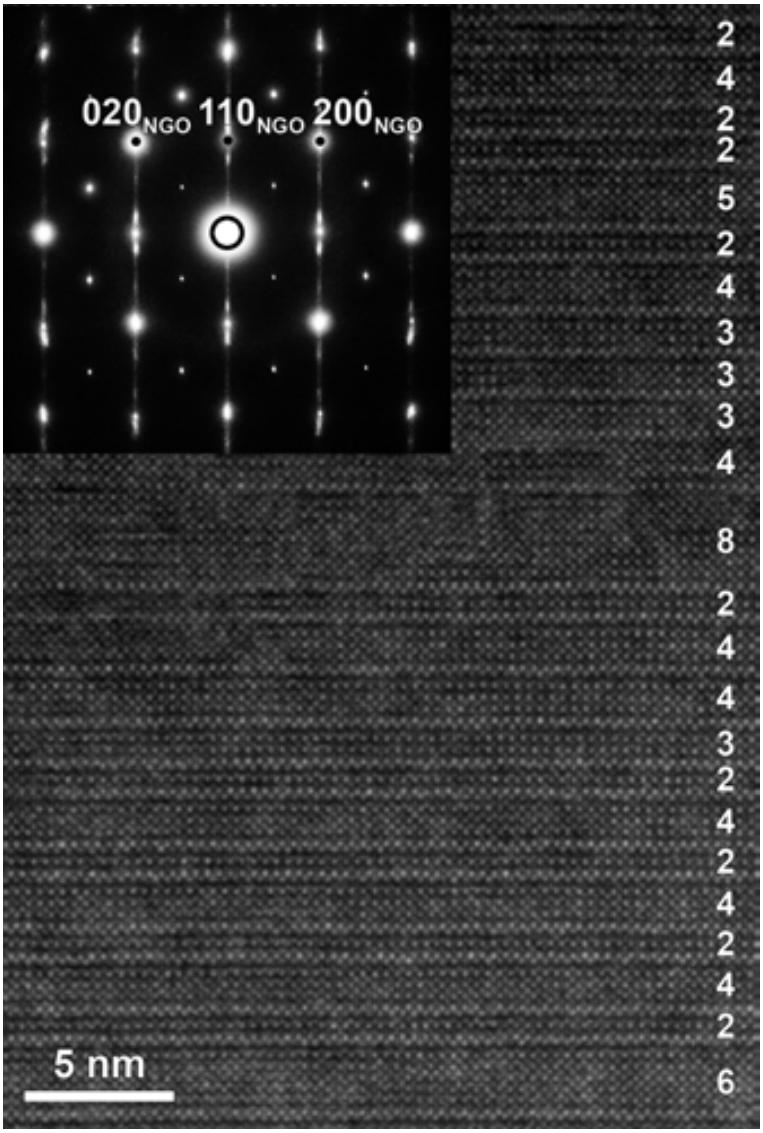

Figure 6.8: Cross-section HREM image and corresponding ED pattern of the film with La/Ni = 1.34 deposited on NGO. The film consists mainly of intermixed regions of $n = 2$, 3 and $n = 4$. The average n value calculated from the image is 3.4.

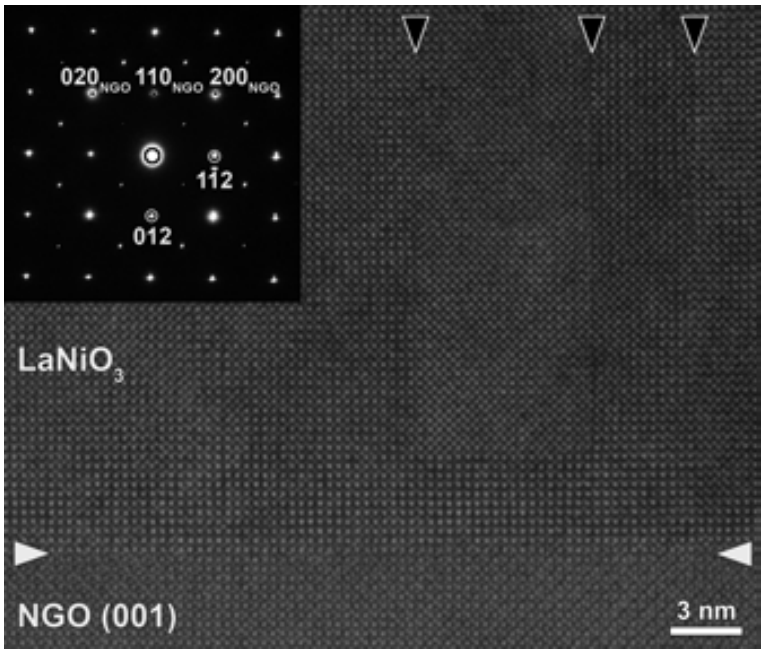

Figure 6.9: Cross-section HREM image and corresponding ED pattern of the film with La/Ni = 1.0 deposited on NGO. The film consists purely of perovskite $LaNiO_3$ regions. The arrows indicate vertical planar defects separating twinned domains.

resistivity of about 12 mΩ·cm at 300 K in O_2 atmosphere (shown in Figure 6.10). At temperatures below 700 K, the $La_2NiO_{4+\delta}$ exhibits the expected semiconductor-type electronic conductivity, which occurs via hopping of p-type charge carriers between mixed-valence nickel cations. A more detailed discussion about the total transport of the $La_2NiO_{4+\delta}$ thin films is found in Section 4.6.

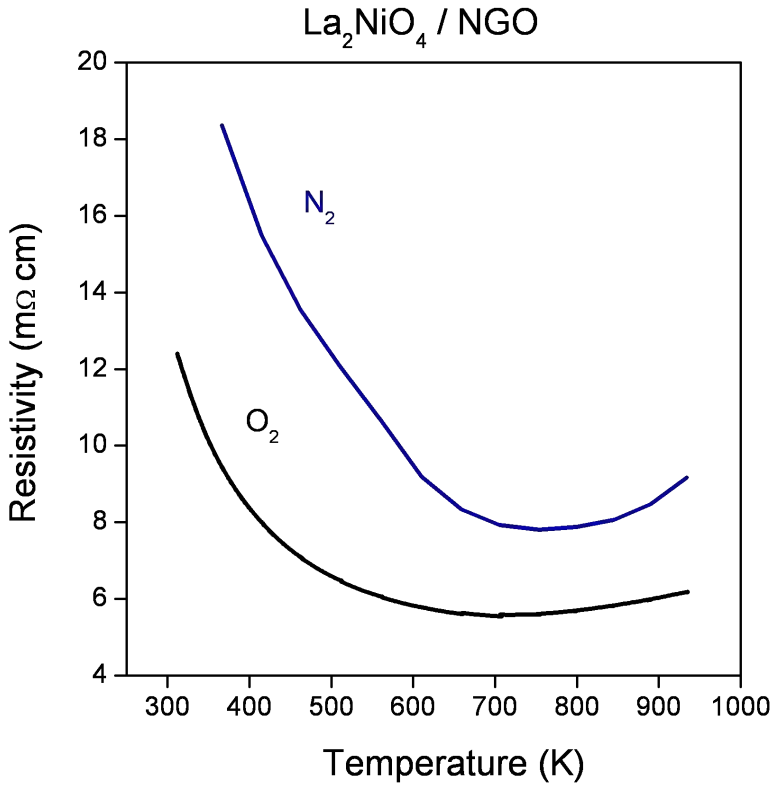

Figure 6.10: High temperature planar resistivity of the epitaxial film with La/Ni composition = 2 deposited on NGO substrate under oxygen and nitrogen atmosphere.

Figure 6.11 shows the variation of the planar resistivity in pure oxygen and pure nitrogen atmosphere as a function of temperature for the film with composition close to La/Ni = 1.7, which consisted of intermixed $n = 1$ and $n = 2$ phases. The resistivity showed a broad semiconducting-to-metallic transition when increasing the

temperature above 500 K in O_2 atmosphere. In a more reducing atmosphere (N_2), the transition is shifted towards higher temperatures, up to approximately 750 K. The room temperature resistivity was about 2.30 mΩ·cm in O_2 and quite higher (7.00 mΩ·cm) in N_2. The difference in the resistivity values in both atmospheres is lower at higher temperatures.

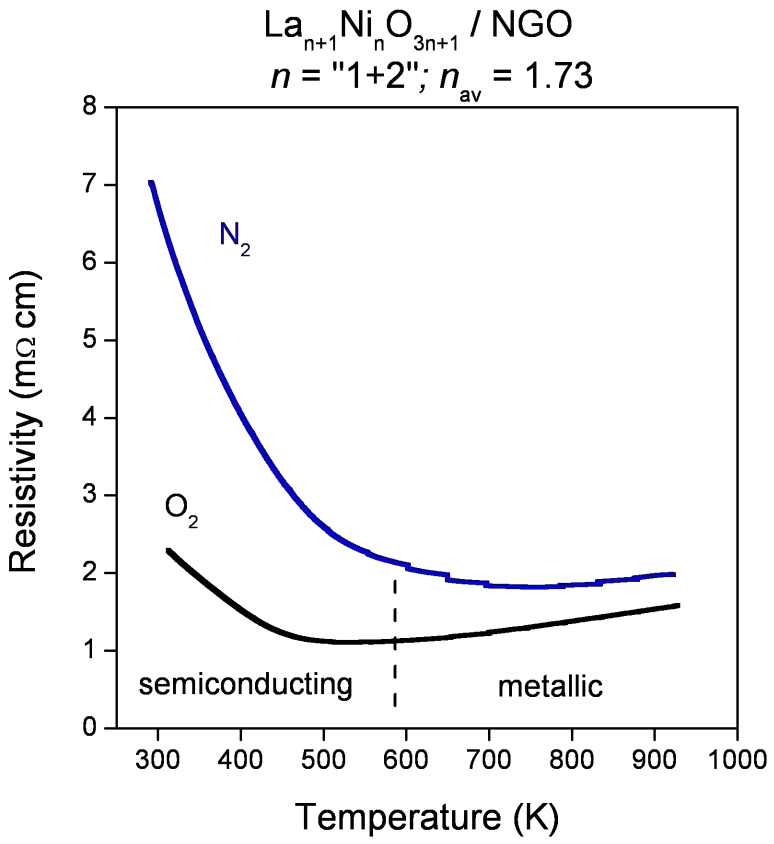

Figure 6.11: High temperature planar resistivity of the epitaxial film with La/Ni composition = 1.7 deposited on NGO substrate under oxygen and nitrogen atmosphere.

In Figure 6.12 a very similar dependence can be observed for the film with an average La/Ni = 1.5 composition, which consisted mainly of intermixed $n = 1$, 2, and 3 domains. The film shows a resistivity of 1.30 mΩ·cm at 300 K in O_2 atmosphere,

and it also changes from a semiconducting to a metallic dependence above 500 K. The resisitivty values in nitrogen are approximately double than in oxygen for the whole measured temperature range and the semiconducting-metallic change is shifted up to approximately 670 K. For these two films (La/Ni = 1.7 and La/Ni = 1.5) the linear temperature dependence of the resistivity above 500 K is a clear signature of the metallic state, so we have to rule out the possibility of a progressive loss of charge carriers, as it was the case for the semiconducting $La_2NiO_{4+\delta}$ phase.

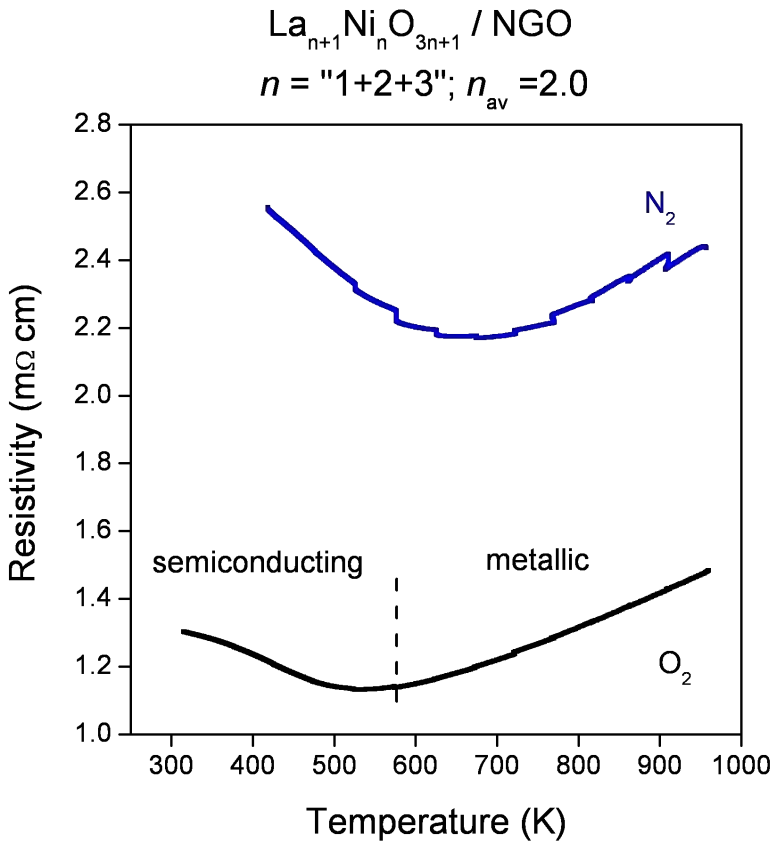

Figure 6.12: High temperature planar resistivity of the epitaxial film with La/Ni composition = 1.5 deposited on NGO substrate under oxygen and nitrogen atmosphere.

A similar type of transition from a semiconducting to a metallic state, associated

to a phase transition at high temperature has already been reported as an intrinsic behavior for $La_3Ni_2O_7$ ($n = 2$) samples [62, 70]. Both Zhang et al. for low temperatures (up to 300 K) [73] and Kobayashi et al. for high temperatures (up to 800 K) [70] have measured different electrical behavior for $La_3Ni_2O_{7-\delta}$ samples with different δ value. Kobayashi et al. [70] measured a room-temperature resistivity which increased dramatically with decreasing oxygen content in $La_3Ni_2O_{7-\delta}$, demonstrating the influence of oxygen content on the electronic transport properties. The nearly stoichiometric and fully oxidized sample of $La_3Ni_2O_{7-\delta}$ exhibited metallic behavior while both oxygen-deficient samples ($La_3Ni_2O_{6.92}$ and $La_3Ni_2O_{6.35}$) were semiconducting at low temperatures.

In our case, we would expect for these two films (La/Ni = 1.7 and La/Ni = 1.5) a different oxygen equilibrium in oxygen than in nitrogen, with a lower oxygen content in this second gas atmosphere. Thus, the higher values of resistivity and shift of the resistivity minimum towards higher temperatures in Figures 6.11 and 6.12 could be related to lower oxygen contents in the $La_3Ni_2O_{7-\delta}$ films in the lower oxygen partial pressure atmosphere (nitrogen). The evolution of the resistivity at constant temperature (during the plateaux), which can be observed in Figures 6.11 and 6.12 can be associated to the incorporation/loss of oxygen to reach the new equilibrium at each temperature. In view of the intermixed microstructure ($n = 1$, 2 and 3 phases), proven by the HREM observations, we cannot distinguish whether these phenomena are directly associated to the intrinsic properties of the $n = 2$ phase, or to the combination of electrical properties of the different intermixed structures in such a close proximity.

Films with an average La/Ni = 1.34 composition, which consisted mainly of intermixed $n = 2$, 3 and 4 domains, and average n value of 3.4, showed a metallic behavior in the whole temperature range analyzed with a resistivity of 340 $\mu\Omega$·cm in oxygen and 400 $\mu\Omega$·cm in nitrogen at 300 K, plotted in Figure 6.13. The resistivity curves corresponding to the different gas atmospheres are approximately parallel in the whole measured temperature range. The resistivity shows an anomaly around 500 K with a 15% decrease in the resistivity upon heating. A similar anomaly was also reported in the literature for ceramic samples of pure $La_4Ni_3O_{10}$ ($n = 3$) ceramic samples [62, 70]. Again, even though in our films we observe a similar

behavior, we cannot rule out that it might be induced by the combination of the transport properties of intermixed regions.

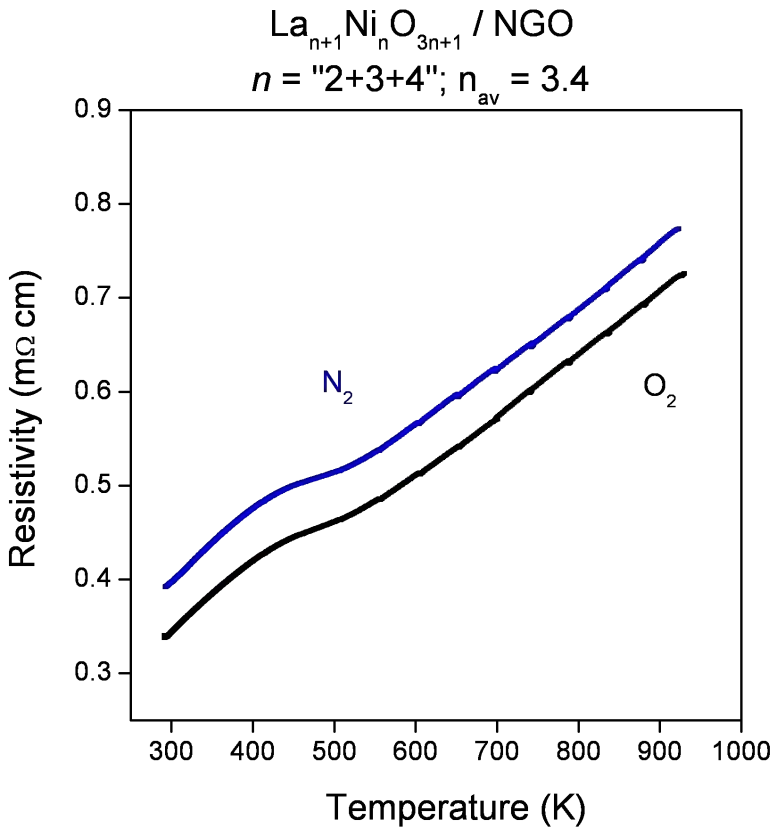

Figure 6.13: High temperature planar resistivity of the epitaxial film with La/Ni composition = 1.34 deposited on NGO substrate under oxygen and nitrogen atmosphere.

In Figure 6.14 it is observed that the films with La/Ni = 1.0 composition, which consisted mainly of $LaNiO_3$ ($n = \infty$) perovskite phase, show normal metallic behavior with the resistivity increasing linearly with the temperature from 194 $\mu\Omega$·cm in oxygen (212 $\mu\Omega$·cm in nitrogen) at 300 K with a slope $d\rho/dT = 0.66$ $\mu\Omega$·cm·K^{-1}. The evolution of the resistivity with temperature in nitrogen is quite similar. The values are comparable to those reported for high quality $LaNiO_3$ thin films [81–83].

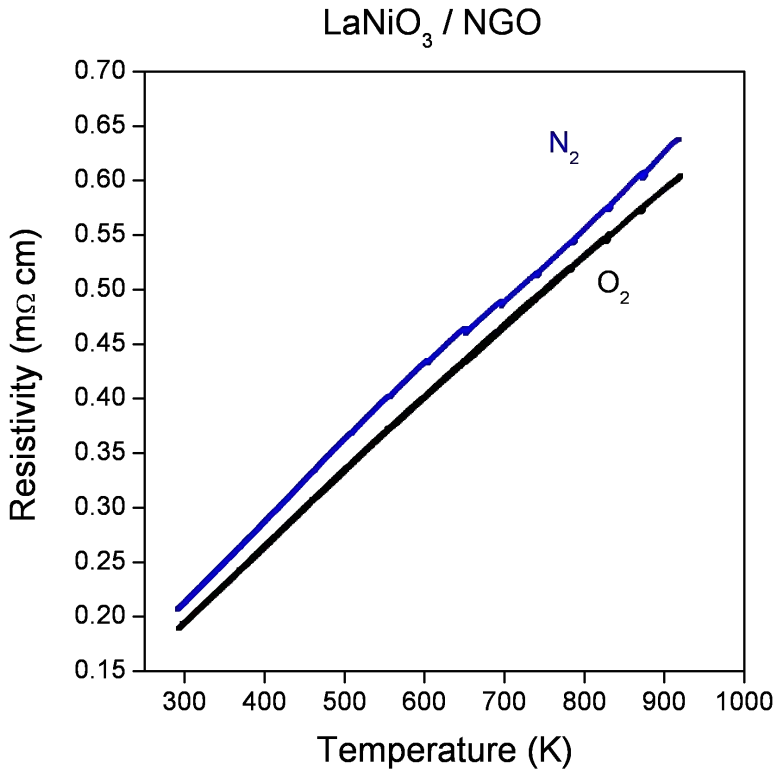

Figure 6.14: High temperature planar resistivity of the epitaxial film with La/Ni composition = 1.0 deposited on NGO substrate under oxygen and nitrogen atmosphere.

In Figure 6.15 we have plotted together the planar resistivity of all the *c*-oriented $La_{n+1}Ni_nO_{3n+1}$ films with different La/Ni composition deposited on NGO substrates, in a pure O_2 atmosphere as a function of temperature. The errors in the value of the conductivity for the different films have been estimated to be of approximately the 25% of the conductivity value, and are mainly due to the errors associated to the measurement of the thickness of the film. As a general trend the resistivity of the films decreases progressively upon decreasing the average composition in the films from La/Ni = 2 to 1. The temperature dependence reveals a change from semiconducting to metallic behavior, in the same way as expected from the results of bulk materials in the literature where the resistivity of $La_{n+1}Ni_nO_{3n+1}$ decreases with n, that is, the number of perovskite layers in the structure, from semiconducting $La_2NiO_{4+\delta}$ ($n = 1$) to a normal metal $LaNiO_3$ ($n = \infty$) which is generally associated to a progressive change from Ni^{2+} for $La_2NiO_{4+\delta}$ to Ni^{3+} for $LaNiO_3$ [62, 68–70].

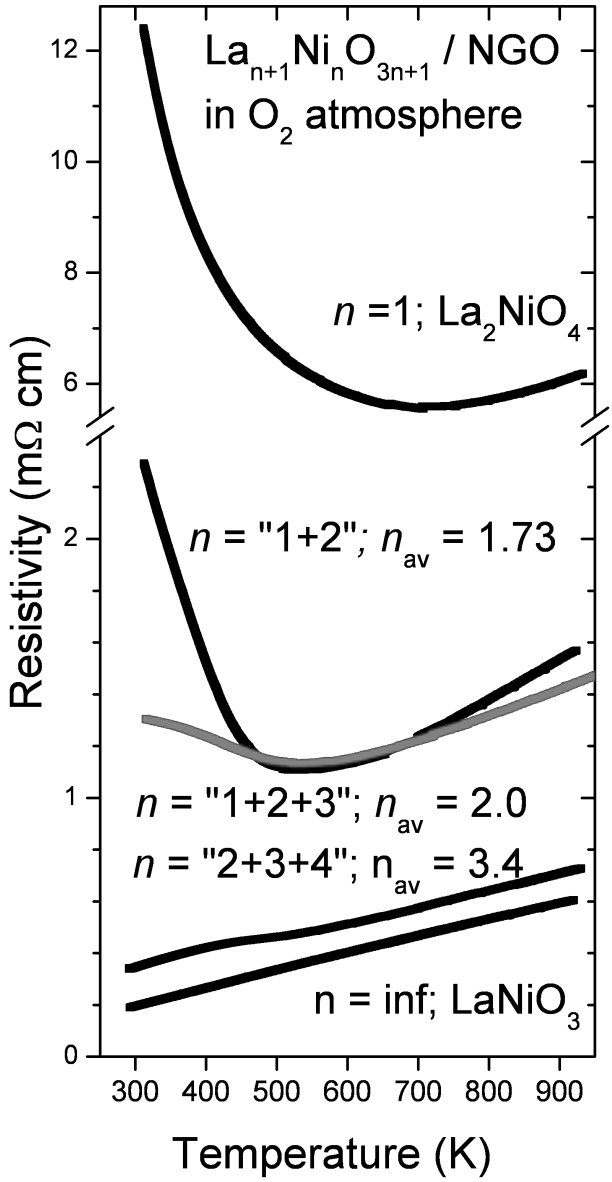

Figure 6.15: High temperature planar resistivity under oxygen atmosphere of the epitaxial films with different La/Ni composition deposited on NGO substrates. For each curve it is indicated the corresponding film microstructure and average n value.

6.5 Conclusions

In summary we have grown high quality epitaxial lanthanum nickel oxide films in a wide range of La/Ni compositions by simply varying the La/Ni composition in the precursor solution of our PI-MOCVD setup. We have obtained films which consisted of pure $La_2NiO_{4+\delta}$ ($n = 1$) and $LaNiO_3$ ($n = \infty$) phases for the extreme La/Ni ratios, above or close to 2 and below or close to 1, respectively, and films with intermixed $La_{n+1}Ni_nO_{3n+1}$ phases for intermediate La/Ni values between 2 and 1. The intermixed phases arise from planar defects in the stacking sequence along the c-axis during film growth. Despite the film microstructure of the mixed phases consists of an intricate intergrowth of domains with different n value, the observed average n value is in agreement with the La/Ni composition ratio. Even more remarkable is the fact that the high temperature electronic transport properties of the films show a progressive change from a semiconducting to a metallic character, along with the described particular anomalies, which for every average n value are consistent with the reported values in literature for ceramic samples of pure phases with the corresponding n values. Thus we can conclude that the transport properties of the intricate intermixed nanodomains follow the behavior of the global (average) film composition induced by the nanoscale. The control over the microstructure of intermixed $La_{n+1}Ni_nO_{3n+1}$ domains opens the possibility to increase, to a certain extent, the electronic conductivity of the films. It is a subject of a further study whether for the obtained microstructures there is still an efficient path for the ionic conductivity. This would lead to mixed ionic-electronic materials with enhanced performances for their application in electrochemical devices.

Chapter 7

Conclusions

The research work presented herein involves a complete structural and microstructural study of epitaxial $La_2NiO_{4+\delta}$ thin films grown by PI-MOCVD, in addition to their mixed ionic-electronic properties characterization by several different techniques. We have studied as well the structural, microstructural and total transport properties of other members of the Ruddlesden-Popper $La_{n+1}Ni_nO_{3n+1}$ family, which have also been grown epitaxially on single crystal substrates.

The main conclusions of the present research work can be summarized as follows:

- With an accurate selection of the deposition conditions we have been able to prepare high quality epitaxial *c*-oriented $La_2NiO_{4+\delta}$ layers by Pulsed Injection-MOCVD. Moreover, by growing films with different thickness and on different substrates, we have been able to vary their properties.

- Due to substrate-lattice mismatch, thin films grown on STO substrate are submitted to a tensile strain, while on NGO they grow subjected to a compresive strain. Both tensile and compressive strain relax as the film thickness increases, i.e, the in- and out-of plane cell parameters vary with film thickness towards a common value.

- From the evolution of the *c*-parameter as a function of temperature, we have been able to appreciate the oxygen loss at high temperatures in air atmosphere and a slower oxygen exchange kinetics in nitrogen, compared to air atmosphere. This kinetic limitation in nitrogen atmosphere is emphasized in the case of

thin, more stressed films grown on both substrates and is in agreement with observations in the conductivity and ECR measurements.

- We were able to determine the total conductivity of the $La_2NiO_{4+\delta}$ thin films along the *a-b* plane as a function of temperature and oxygen partial pressure. As expected, the conductivity has shown a semi-conducting thermally activated behavior for temperatures up to 425 °C and the activation energy has been found to increase with thickness.

- It seems that either directly due to the strain, or indirectly, due to differences in oxygen content or in microstructure, the electronic conductivity increases, while the ionic conductivity decreases with film thickness reduction. All the $La_2NiO_{4+\delta}$ films have shown total conductivity larger than that found in bulk $La_2NiO_{4+\delta}$ and the 50 nm films and thinner ones have shown a total conductivity which is also larger than that found in single crystal along the *a-b* plane. A maximum conductivity of 475 S/cm around 425 °C has been measured in 33 nm thick films, corresponding to the highest value reported to date for this compound.

- Although we have not found a complementary evidence yet, the IEDP measurements fitting model for the thicker films evidences to the existence of two regions in the film with different ionic conductivity along the *c*-axis: a higher one close to the film surface and a lower and variable one close to the substrate.

- We succesfully measured anisotropy in the oxygen diffusion of the films. As expected, the tracer diffusion and surface exchange coefficients are thermally activated and are approximately two orders of magnitude higher along the *a-b* plane than along the *c*-axis. Moreover, the low activation energies estimated for the diffusivity in both directions seem to correspond to a vacancy mechanism contribution to the ionic conduction at low temperatures.

- Chemical surface exchange coefficients have been measured by the electrical conductivity relaxation method, obtaining a surface exchange coefficient which is in agreement with the one measured by other authors for epitaxial $La_2NiO_{4+\delta}$ thin films.

- Comparing the ECR and the isotope c-axis surface exchange data we observed that, as expected, the chemical surface exchange coefficients are much larger (two orders of magnitude) than the isotopic surface exchange coefficients. The activation energy of the isotope exchange was very similar to the obtained values for the ECR measurement, which seems to confirm the validity of the data of both experiments.

- With regard to the oxygen isotope exchange measurements, it should be highlighted that we have developed and validated for the first time a methodology for the determination of anisotropic tracer diffusion and surface exchange coefficients in two perpendicular directions for thin films.

- Due to a higher thermal stability of the members with larger n of the Ruddlesden-Popper family, they appear as new candidates for IT-SOFC cathodes. For this reason, we have grown high quality epitaxial lanthanum nickel oxide films in a wide range of La/Ni compositions by simply varying the La/Ni composition in the precursor solution of our PI-MOCVD setup. In addition to the pure $La_2NiO_{4+\delta}$ ($n = 1$) films, we have obtained films which consisted pure $LaNiO_3$ ($n = \infty$) phases and films with intermixed $La_{n+1}Ni_nO_{3n+1}$ phases for intermediate La/Ni values between 2 and 1. The intermixed phases arise from planar defects in the stacking sequence along the c-axis during film growth. Despite the film microstructure of the mixed phases consists of an intricate intergrowth of domains with different n value, the observed average n value is in agreement with the La/Ni composition ratio.

- Even more remarkable is the fact that the high temperature electronic transport properties of the films show a progressive change from a semiconducting to a metallic character, along with some particular anomalies, which for every average n value are consistent with the reported values in literature for ceramic and single crystal samples of pure phases with the corresponding n values. Thus we can conclude that the transport properties of the intricate intermixed nanodomains follow the behavior of the global (average) film composition induced by the nanoscale.

It is a subject of a further study whether $La_{n+1}Ni_nO_{3n+1}$ thin films with the

obtained microstructures still have an efficient path for the ionic conductivity. This would lead to mixed ionic-electronic nanocomposite materials with enhanced performances for their application in electrochemical devices.

In summary, the total conductivity of the $La_2NiO_{4+\delta}$ thin films is larger than that of the $La_2NiO_{4+\delta}$ single crystal and bulk samples, while the diffusivity and surface exchange coefficient values are quite similar. Therefore, the $La_2NiO_{4+\delta}$ prepared by MOCVD can be considered as a possible candidate for its use as cathode for SOFC. Stability, compatibility with the other parts of the fuel cell and performance measurements should be studied to verify its functional application.

Although epitaxial $La_2NiO_{4+\delta}$ have shown good conducting properties, it is clear that for its application in conventional SOFC, the films have to be deposited onto rough polycrystalline electrolyte films. For this purpose we have already prepared polycrystalline $La_2NiO_{4+\delta}$ films deposited on half cells anode/electrolyte, and complete fuel tests will be performed by Dr. Serra from the Instituto de Tecnología Química (CSIC-UPV). The results are subject of a further study and go beyond the scope of the present work.

Bibliography

[1] Turner, J. A. *Science* **305**(5686), 972 (2004).

[2] Hirschenhofer, J. H., Stauffer, D. B., Engleman, R. R., and Klett, M. G. *Fuel Cell Handbook. Fourth Edition.* Pearsons Corporation, for U.S. Department of Energy, Office of Fossil Energy, Federal Energy Technology Center, (1999).

[3] Twigg, M. V. *Catalyst Handbook.* Wolfe Publishing Ltd, 2 ed edition, (1989).

[4] http://science.nasa.gov/headlines/. National Aeronautics and Space Administration (NASA), (visited on the 13th November 2006).

[5] Minh, N. Q. *J. Am. Ceram. Soc.* **76**, 563–588 (1993).

[6] Kawada, T. and Yokokawa, H. *Key Eng. Mat. Vols.* **125-126**, 187–248 (1997).

[7] Steele, B. C. H. In *Proc. 1st European SOFC Forum, Oberrohrdorf, vol. 1,* Bossel, U., editor, 375, (1994).

[8] Kroger, F. *The Chemistry of Imperfect Crystals.* pp. 213-257. North-Holland, Amsterdam, (1964).

[9] Bouwmeester, H. J. M. and Gurgraaf, A. J. *in A. J. Bugraaf and L. Cot (Eds.) Fundamentals of Inorganic Membrane Science and Technology*, 375. Elsevier, Amsterdam (1996).

[10] Steele, B. C. H. and Heinzel, A. *Nature* **414**, 345 (2001).

[11] Skinner, S. and Kilner, J. *Mater. Today* **6**(3), 30–37 (2003).

[12] Adler, S. *Solid State Ionics* **111**, 125 (1998).

[13] van Doorn, R. and Burggraaf, A. *Solid State Ionics* **128**, 65 (2000).

[14] Brugnoni, C., Ducatia, U., and Scagliotti, M. *Solid State Ionics* **76**, 177 (1995).

[15] Jiang, Y., Wang, S., Zhang, Y., Yan, J., and Li, W. *Solid State Ionics* **110**, 111 (1998).

[16] Van Herle, J., McEvoy, A. J., and Ravindranathan Thampi, K. *Electrochim. Acta* **41**(9), 1447 (1996).

[17] Teraoka, Y., Nobunaga, T., Okamoto, K., Miura, N., and Yamazoe, N. *Solid State Ionics* **48**(3-4), 207 (1991).

[18] Yaremchenko, A. A., Kharton, V. V., Naumovich, E. N., and Tonoyan, A. A. *Mater. Res. Bull.* **35**, 515 (2000).

[19] Souza, R. D. and Kilner, J. *Solid State Ionics* **106**, 175 (1998).

[20] Souza, R. A. D., Kilner, J. A., and Walker, J. F. *Mater. Lett.* **43**(1-2), 43–52 (2000).

[21] Steele, B. C. H. *J. Power Sources* **49**, 1 (1994).

[22] Tai, L. W., Nasrallah, M. M., Anderson, H. U., Sparlin, D. M., and Sehlin, S. R. *Solid State Ionics* **76**(3-4), 259–271 (1995).

[23] Tai, L. W., Nasrallah, M. M., Anderson, H. U., Sparlin, D. M., and Sehlin, S. R. *Solid State Ionics* **76**(3-4), 273–283 (1995).

[24] Bassat, J., Odier, P., Villesuzanne, A., Marin, C., and Pouchard, M. *Solid State Ionics* **167**, 341 (2004).

[25] Skinner, S. J. and Kilner, J. A. *Solid State Ionics* **131**, 709 (2000).

[26] Vashook, V. V., Tolochko, S. P., Yushkevich, I. I., Makhnach, L. V., Kononyuk, I. F., Altenburg, H., Hauck, J., and Ullmann, H. *Solid State Ionics* **110**, 245 (1998).

[27] Kharton, V. V., Viskup, A. P., Naumovich, E. N., and Marques, F. M. B. *J. Mater. Chem.* **9**, 2623 (1999).

[28] Kharton, V. V., Viskup, A. P., Kovalevsky, A., Naumovich, E. N., and Marques, F. M. B. *Solid State Ionics* **143**, 337 (2001).

[29] Skinner, S. J. and Kilner, J. A. *Ionics* **5**, 171 (1999).

[30] Kilner, J. A. and Shaw, C. K. M. *Solid State Ionics* **154-155**, 523 (20002).

[31] Vashook, V. V., Yushkevich, I. I., Kokhanovsky, L. V., Makhnach, L. V., Kononyuk, I. F., Ullmann, H., and Altenburg, H. *Solid State Ionics* **119**, 23 (1999).

[32] Boehm, E., Bassat, J. M., Dordor, P., Mauvy, F., Grenier, J. C., and Stevens, P. *Solid State Ionics* **176**(37-38), 2717 (2005).

[33] Beille, J., Cabanel, R., Chaillout, G., Chevalier, B., Demazeau, G., Deslandes, F., Etourneau, J., Lejay, P., Michel, C., Provost, J., Raveau, B., Sulpice, A., Tholence, J. L., and Tounier, R. *C.R. Acad. Sci., Ser. II* **304**, 1097 (1987).

[34] Jorgensen, J. D., Dabrowski, B., Pei, S., Hinks, D. G., Soderholm, L., Morosin, B., Schirber, J. E., Venturini, E. L., and Ginley, D. S. *Phys. Rev. B* **38**, 11337 (1988).

[35] Kakol, Z., Spalek, J., and Honig, J. M. *Solid State Commun.* **71**, 283 (1989).

[36] Kakol, Z., Spalek, J., and Honig, J. M. *Solid State Commun.* **71**, 511 (1989).

[37] Kakol, Z., Spalek, J., and Honig, J. M. *Solid State Commun.* **79**, 288 (1989).

[38] Hoffman, S. A., Venkatraman, C., Ehrlich, S. N., Durbin, S. M., and Liedl, G. L. *Phys. Rev. B* **43**, 7852 (1991).

[39] Rice, D. and Buttrey, D. *J. Solid State Chem.* **105**, 197 (1993).

[40] Rodriguez-Carvajal, J., Fernandez-Diaz, M. T., and Martinez, J. L. *J. Phys.-Condens. Mat.* **3**, 3215 (1991).

[41] Medarde, M. and Rodríguez-Carvajal, J. *Z. Phys. B* **102**, 307 (1997).

[42] Buttrey, D., Harrison, H., Honig, J., and Schartman, R. *J. Solid State Chem.* **54**, 407 (1984).

[43] Tamura, H., Hayashi, A., and Ueda, Y. *Physica C* **216**, 83 (1993).

[44] Tranquada, J., Kong, Y., Lorenzo, J., Buttrey, D., Rice, D., and Sachan, V. *Phys. Rev. B* **50**, 6340 (1994).

[45] Tamura, H., Hayashi, A., and Ueda, Y. *Physica C* **258**, 61.

[46] Poirot, N., Odier, P., and Simon, P. *J. Alloy. Compd.* **262 - 263**, 147 (1997).

[47] Poirot, N., Simon, P., Odier, P., and Bassat, J. *Eur. Phys. J.* **2**, 469 (1998).

[48] Demourgues, A., Wattiaux, A., Grenier, J., Pouchard, M., Soubeyroux, J., Dance, J., and Hagenmuller, P. *J. Solid State Chem.* **105**, 458 (1993).

[49] Jorgensen, J., Dabrowski, B., Pei, S., Richards, D., and Hinks, D. *Phys. Rev. B* **40**(4) (1989).

[50] Minervini, L., Grimes, R. W., Kilner, J. A., and Sickafus, K. E. *J. Mater. Chem.* **10**, 2349 (2000).

[51] Frayret, C., Villesuzanne, A., and Pouchard, M. *Chem. of Mater.* **17**(26), 6538 (2005).

[52] Demourges, A., Weill, F., Darriet, B., Wattiaux, A., Grenier, J. C., Graverau, P., and Pouchard, M. *J. Solid State Chem.* **106**(2), 317.

[53] Demourges, A., Weill, F., Darriet, B., Wattiaux, A., Grenier, J. C., Graverau, P., and Pouchard, M. *J. Solid State Chem.* **106**(2), 330 (1993).

[54] Hiroi, Z., Obata, T., Takano, M., Bando, Y., Takeda, Y., and Yamamoto, O. *Phys. Rev. B* **41**(16), 11665 (1990).

[55] Hücker, M., Chung, K., Chand, M., Vogt, T., Tranquada, J., and Buttrey, D. *Phys. Rev. B* **70**, 064105 (2004).

[56] Wochner, P., Tranquada, J. M., J., D., and V, B. *Phys. Rev. B* **57**(2) (1998).

[57] Sayer, M. and Odier, P. *J. Solid State Chem.* **67**, 26 (1987).

[58] Bassat, J. M., Loup, J. P., and Odier, P. *J. Phys.- Condens. Mat.* **6**, 8285 (1994).

[59] Rao, C. N. R., Buttrey, D. J., Otsuka, N., Ganmguly, P., Harrison, H. R., Sandberg, C., and Honig, J. M. *J. Solid State Chem.* **51**, 266 (1984).

[60] Bassat, J. M., Gervais, F., Odier, P., and Loup, J. P. *Mat. Sci. Eng.* **B3**, 507 (1989).

[61] Ishikawa, K., Shibata, W., Watanabe, K., Isonaga, T., Hashimoto, M., and Suzuki, Y. *J. Solid State Chem.* **131**, 275 (1997).

[62] Amow, G. and Skinner, S. J. *J. Solid State Electr.* **10**, 538 (2006).

[63] Aguadero, A., Alonso, J. A., Martínez-Lope, M. J., Fernández-Díaz, M. T., Escuderoa, M. J., and Daza, L. *J. Mater. Chem.* **16**, 3402 (2006).

[64] Dembinski, K., Bassat, J., Coutures, J. P., and Odier, P. *J. Mater. Sci. Lett.* **6**, 1365 (1987).

[65] Honig, J. M. and Buttrey, D. J. *Localization and Metal-Insulator Transitions. Edited by Fritzche H, Adler D, Ovshinsky SR.*, 409–416. Plenum, New York (1985).

[66] Ruddlesden, S. N. and Popper, P. *Acta Crytallogr.* **11**, 54 (1956).

[67] Greenblatt, M. *Curr. Opin. in Solid St. M.* **2**, 174 (1997).

[68] Ram, R. A. M., Ganaphathi, L., Ganguly, P., and Rao, C. N. R. *J. Solid State Chem* **63**, 139 (1986).

[69] Sreedhar, K., McElfresh, M., Perry, D., Kim, D., Metcalf, P., and Honig, J. *J. Solid State Chem.* **110**, 208 (1994).

[70] Kobayashi, Y., Taniguchi, S., Kasai, M., Sato, M., Nishioka, T., and Kontani, M. *J. Phys. Soc. Jpn.* **65**, 3978 (1996).

[71] Greenblatt, M., Zhang, Z., and Whangbo, M. H. *Synthetic Met.* **85**, 1451 (1997).

[72] Ling, C. D., Argyriou, D. N., Wu, G. Q., and Neumeier, J. J. *J. Solid State Chem.* **152**, 517 (2000).

[73] Zhang, Z., Greenblatt, M., , and Goodenough, J. B. *J. Solid State Chem.* **108**, 402 (1994).

[74] Savchenko, V. F., lvashkevich, L. S., and Lyubkina, I. *Russ. J. lnorg. Chem.* **33**, 17 (1988).

[75] Zhang, Z. and Greenblatt, M. *J. Solid State Chem.* **117**, 236 (1995).

[76] Wold, A., Post, B., and Banks, E. *J. Am. Chem. Soc.* **79**, 4911 (1957).

[77] Demazeau, G., Marbeuf, A., Pouchard, M., and Hagenmuller, P. *J. Solid State Chem.* **3**, 582 (1971).

[78] Nakamura, T., Petzov, G., and Gauckler, L. *Mater. Res. Bull.* **14**, 649 (1979).

[79] Crespin, M., Levitz, P., and Gatineau, L. *J. Chem. Faraday Trans.* **79**, 1181 (1983).

[80] Drennan, J., Tavares, C. P., and Steele, B. C. H. *Mater. Res. Bull.* **7**, 621 (1982).

[81] Satyalakshmi, K. M., Mallya, R. M., Ramanathan, K. V., Wu, X. D., Brainard, B., Gautier, D. C., Vasanthacharya, N. Y., and Hegde, M. S. *Appl. Phys. Lett.* **62**, 1233 (1993).

[82] Chen, P., Xu, S. Y., Zhou, W. Z., and Ong, C. K. *J. Appl. Phys.* **85**(5) (1999).

[83] Dobin, A. Y., Nikolaev, K. R., Krivorotov, N., Wentzcovitch, R. M., Dahlberg, E. D., and Goldman, A. M. *Phys. Rev. B* **68**, 113408 (2003).

[84] Aiyer, H. N., Raju, A. R., Subbanna, G. N., and Rao, C. N. R. *Chem. Mater.* **9**, 755 (1997).

[85] Raju, A. R., Aiyer, H. N., and Rao, C. N. R. *Chem. Mater.* **7**, 225 (1995).

[86] Smith, J. B. and Norby, T. *J. Electrochem. Soc.* **153**(2), A233 (2006).

[87] Abrutis, A., .Teiserskis, A., Garcia, G., Kubilius, V., Saltyte, Z., Salciunas, Z., Faucheux, V., Figueras, A., and Rushworth, S. *J. Membrane Sci.* **240**, 113 (2004).

[88] Li, C., Hu, T., Zhang, H., Chen, Y., Jin, J., and Yang, N. *J. Membrane Sci.* **226**, 1 (2003).

[89] Fontaine, M. L., Laberty-Robert, C., Ansart, F., and Tailhades, P. *J. Solid State Chem.* **177**, 1471 (2004).

[90] Faucheux, V., Pignard, S., and Audier, M. *J. Solid State Chem.* **177**, 4616 (2004).

[91] Faucheux, V., Pignard, S., and Audier, M. *J. Cryst. Growth* **275**, e947 (2005).

[92] Faucheux, V. and nd S. Pignard, M. A. *Appl. Surf. Sci.* **252**, 5504 (2006).

[93] Kim, G., Wang, S., Jacobson, A. J., and Chen, C. L. *Solid State Ionics* **177**, 1461 (2006).

[94] Shinomori, S., Kawasaki, M., and Tokura, Y. *Appl. Phys. Lett.* **80**(4), 574 (2002).

[95] Morosanu, C. *Thin Films by Chemical Vapor Deposition.* Thin Films Science and Technology 7. Elsevier, Amsterdam, (1990).

[96] Choy, K. *Prog. Mater. Sci.* **48**, 57 (2003)).

[97] Senateur, J., Madar, R., Thomas, O., Weiss, F., and Abrutis, A. Technical report, 1999.

[98] Lindner, J. PhD thesis, ENSPG-INPG, Grenoble, France, (1999).

[99] Dubordieu, C., Pantou, R., Weiss, F., Sénateur, J., Dooryhee, E., Hodeau, J., Nemoz, M., Kobernik, G., and Haesller, W. *Ferroelectrics* **268**, 557 (2002).

[100] Burriel, M., Garcia, G., Santiso, J., Hansson, A., Linderoth, S., and Figueras, A. *Thin Solid Films* **473**, 98 (2005).

[101] Burriel, M., Garcia, G., Santiso, J., Abrutis, A., Saltyte, Z., and Figueras, A. *Chem. Vapor Depos.* **11**(2), 106 (2005).

[102] Bedoya, C., Condorelli, G., Finocchiaro, S., Mauro, A. D., Atanasio, D., Fragalà, I., Cattaneo, L., and Carella, S. *Chem. Vapor Depos.* **12**, 46 (2006).

[103] Lane, P., Wright, P., Crosbie, M., Pitt, A., Reeves, C., Cockayne, B., Jones, A., and Leedham, T. *J. Cryst. Growth* **192**, 423 (1998).

[104] Binnig, G., Quate, C. F., and Gerber, C. *Phys. Rev. Lett.* **56**, 930–933 (1986).

[105] Crank, J. *The Mathematics of Diffusion.* Oxford University Press, Oxford, (1975).

[106] Killoran, D. *J. Electrochem. Soc.* **190**, 170 (1963).

[107] Mehta, A. and Heaney, P. J. *Phys. Rev. B* **49**, 563 (1994).

[108] Lane, P., Crosbie, M., Wright, P., Donohue, P., Hirst, P., Reeves, C., Anthony, C., Jones, J., Todd, M., and Williams, D. *Chem. Vapor Depos.* **9**(2), 87 (2003).

[109] Fontaine, M., Laberty-Robert, C., Barnabe, A., Ansart, F., and P.Tailhades. *Ceram. Int.* **30**, 2087 (2004).

[110] Skinner, S. *Solid State Sci.* **5**, 419 (2003).

[111] Kharton, V., Yaremchenko, A., Shaula, A., Patrakeev, M., Naumovich, E., Logvinovich, D., Frade, J., and Marques, F. *J. Solid State Chem.* **177**, 26 (2004).

[112] Odier, P., Nigara, Y., and Coutures, J. *J. Solid State Chem.* **56**, 32 (1985).

[113] Chen, X. J., Soltan, S., Zhang, H., and Habermeier, H.-U. *Phys. Rev. B* **65**, 174402 (2002).

[114] Mogni, L., Fouletier, J., Prado, F., and Caneiro, A. *J. Solid State Chem.* **178**, 2715 (2005).

[115] Maier, J. *Solid State Ionics* **112**, 197 (1998).

[116] Maier, J. *Solid State Ionics* **135**, 575 (2000).

[117] Maier, J. *Physical Chemistry of Ionic Materials. Ions and Electrons in Solids.* John Wiley and Sons, Ltd, England, (2004).

[118] Ziegler, J. F. *SRIM (The Stopping and Range of Ions in Matter) Software, from http://www.srim.org/*, (Retrieved January 18, 2006).

[119] Read, M., Islam, M., Watson, G., and Hancock, F. *J. Mater. Chem.* **11**, 2597 (2001).

[120] Munnings, C., Skinner, S., Amow, G., Whitfield, P., and Davidson, I. *Solid State Ionics* **176**, 1895 (2005).

[121] Wang, A., Verma, Y. L., Yang, and A. J. Jacobson, a. B. A. *Solid State Ionics* **140**, 125 (2001).

[122] Manning, P., Sirman, J., and Kilner, J. *Solid State Ionics* **93**, 125 (1997).

[123] Ishihara, T., Kilner, J. A., Honda, M., Sakai, N., Yokokawa, H., and Takita, Y. *Solid State Ionics* **113-115**, 1998 (1998).

[124] Yasuda, I. and Hikita, T. *J. Electrochem. Soc.* **141**(5), 1268 (1994).

[125] ten Elshof, J. E., Lankhorst, M. H. R., and Bouwmeester, H. J. M. *Solid State Ionics* **99**, 15 (1997).

[126] Lane, J. A. and Kilner, J. A. *Solid State Ionics* **136-137**, 997 (2000).

[127] den Otter, M. W., Bouwmeester, H. J. M., Boukamp, B. A., and Verweij, H. *J. Electrochem. Soc.* **148**(2), J1 (2001).

[128] Soegaard, M. *Transport properties and oxygen stoichiometry of mixed ionic electronic conducting perovskite-type oxides.* PhD thesis, Risoe National Laboratory, July (2006).

[129] Kim, G., Wang, S., Jacobson, A. J., Yuan, Z., Donner, W., Chen, C. L., Reimus, L., and P. Brodersen, a. C. A. M. *Appl. Phys. Lett.* **88**, 024103 (2006).

[130] Garcia-Munoz, J. L., Rodriguez-Carvajal, J., Lacorre, P., and Torrance, J. B. *Phys. Rev. B* **46**(8), 4414 (1992).